

Copyright

by

Fan Zhang

2011

The Dissertation Committee for Fan Zhang
certifies that this is the approved version of the following dissertation:

Electronic Correlations in Few Layer Graphene

Committee:

Allan H. MacDonald, Supervisor

James R. Chelikowsky

Alex Demkov

Zhen Yao

Gregory A. Fiete

Electronic Correlations in Few Layer Graphene

by

Fan Zhang, B.S.

Dissertation

Presented to the Faculty of the Graduate School of

The University of Texas at Austin

in Partial Fulfillment

of the Requirements

for the Degree of

Doctor of Philosophy

The University of Texas at Austin

December 2011

Dedicated to My Parents and WW.

Acknowledgments

First and foremost, I would like to express my heartfelt gratitude to my advisor Allan MacDonald, who has been an excellent teacher, mentor and friend. I was fortunate to have learned how to approach physics from one of the very best. He always led me to exciting physics and opened many doors of opportunity for me. I am also indebted to his extraordinary degree of kindness, patience and encouragement.

I have had the pleasure of working and collaborating with many others along the way. I would like to specially thank Qian Niu, Greg Fiete and Milos Milosavljevic, whose enthusiasm and support helped ease my introduction to various fields of condensed matter theory. I must also acknowledge Chunning Lau, Wenzhong Bao, Jairo Velasco Jr. and Lei Jing at University of California at Riverside, whose collaboration gave me a wonderful opportunity to think about and also learn from their excellent experiments. A special thanks to Dagim Tilahun, Hongki Min, Jung Jeil and Bhagawan Sahu and Marco Polini for giving me generous assistance and tireless support while we were working on projects together.

I am thankful to Professors Jim Chelikowsky, Alex Demkov, Zhen Yao and Greg Fiete for taking their time to be on my dissertation committee.

Thanks to Becky Drake for all of her patience and help. She is so reliable in tackling our administrative tasks. I still owe her a panda, and I will carry out

promise in the near future. A special thanks to Hongki Min, Ion Garate, Dmytro Pesin and Joseph Wang, my all-time officemates. My gratitude also goes to my other group members who I have not mentioned above: Yafis Barlas, Rafi Bistritzer, Rohit Hegde, Guru Khalsa, Wei-Cheng Lee, Maria Moura, Tami Pereg-Barnea, Inti Sodemann, Jung-Jung Su and John Tolsma. I have realized that our friendship has inspired me in my ways.

I wish to convey special gratitude to Yunmeng Du, Tiantian Zhang, Yong Huang, Lei Li, Qiang Luo and Wande Zhang, and I will miss the wonderful times we spent together. I would also like to thank Changhai Xu, Youzhong Guo, Jun Wen, Xuhui Luo, Shengyuan Yang, Fang Tang, Junwei Wei, Liming Luo, Peng Dong, Jing Zan, Ligang Long, and Chen Su. We have enjoyed great times playing badminton every week. The friendship built with you all during my stay in Austin shall forever be etched in my heart, as I hope that it does in yours as well.

Finally, I wish to thank my parents and Ting Wang for their unconditional love and unwavering support in my life. I sincerely appreciate their understanding for that I have been million miles away from them for so many years. Mere words cannot convey my immense gratitude and love. With them standing by my side I feel joy and deep inner peace. They are the reason why I enjoy physics and life.

FAN ZHANG

The University of Texas at Austin

December 2011

Electronic Correlations in Few Layer Graphene

Publication No. _____

Fan Zhang, Ph.D.

The University of Texas at Austin, 2011

Supervisor: Allan H. MacDonald

In this thesis we investigate the electronic band structures and the correlations in chirally (ABC) stacked N -layer graphene with $N \geq 2$. We use *ab initio* density-functional theory and $\mathbf{k} \cdot \mathbf{p}$ theory to fit the parameters of a π -band tight-binding model. External potential differences between top and bottom layers are strongly screened by charge transfer but still open an energy gap at overall neutrality. Perpendicular magnetic field drives the system into the quantum Hall region with $4N$ -fold zero energy Landau levels. We predict that Coulomb interactions spontaneously break the $SU(4N)$ symmetry and drive quantum Hall effects at all integer fillings ν from $-2N$ to $2N$ with exotic spin and pseudospin polarizations.

Based on mean-field theory and perturbative renormalization group analysis, we predict that the ground state of bilayer graphene spontaneously breaks inversion symmetry for arbitrarily weak electron-electron interactions and conclude that this instability is not suppressed by quantum fluctuations but that, because of trigonal warping, it may occur only in high quality suspended bilayers. Remarkably flat conduction and valence bands that touch at charge neutrality point and Bloch states with large pseudospin chirality combine to make the bilayer graphene gapless band state strongly susceptible to a family of broken symmetry states in which each spin-valley flavor spontaneously transfers charge between layers. We explain how these states are distinguished by their charge, spin, and valley Hall conductivities, by their orbital magnetizations, and by their edge state properties. We further analyze how these competing states are influenced by Zeeman fields that couple to spin and by interlayer electric fields that couple to layer pseudospin, and comment on the possibility of using response and edge state signatures to identify the character of the bilayer ground state experimentally. We demonstrate that similar insulating broken symmetry states and spontaneous topological orders also occur in bilayer's thicker cousins, chirally stacked multilayer graphene systems.

Contents

Acknowledgments	v
Abstract	vii
List of Tables	xiii
List of Figures	xiv
Chapter 1 Introduction	1
1.1 Few-layer graphene	1
1.2 Outline of the thesis	5
Chapter 2 Band Structure of ABC-Stacked Graphene Few-Layers	8
2.1 Introduction	9
2.2 Effective model	12
2.2.1 Low-energy effective model	12
2.2.2 Diagrammatic derivation of the effective model	16
2.2.3 <i>Ab initio</i> density-functional theory calculations	19
2.2.4 Extracting hopping parameters from DFT	20
2.2.5 Electron(hole) pockets and Lifshitz transitions	22

2.3	Induced band gaps in trilayers	26
2.3.1	Energy bands with electric fields	26
2.3.2	Self-consistent Hartree calculation	28
2.4	Discussion	33
Chapter 3 Electron-Electron Interactions in Bilayer Graphene		37
3.1	Introduction	38
3.2	Similarities and differences between 1DES and bilayer graphene . .	40
3.3	Perturbative renormalization group analysis in bilayer graphene . .	43
3.3.1	Green's functions and frequency sums	43
3.3.2	PRG analysis for a single spin-valley	45
3.3.3	Spins pseudospins and distinct interaction parameters	50
3.3.4	RG flow equations for distinct interaction parameters	53
3.3.5	Influence of trigonal warping and external potential	56
3.4	Spontaneous layer inversion symmetry breaking	59
3.4.1	Susceptibilities and which symmetry is broken	59
3.4.2	Mean-field pseudospin orientation	62
3.5	Bilayer graphene Dirac-point gaps and symmetry-breaking states . .	64
3.5.1	Introduction	64
3.5.2	Full $k \cdot p$ Hamiltonian of bilayer graphene	65
3.5.3	Trigonal warping does not yield a gapped state	67
3.5.4	Nematic order does not yield a gapped state	68
3.5.5	Relative layer displacement does not yield a gapped state . .	71
3.5.6	Broken inversion symmetry yield gap and Berry curvature . .	73
Chapter 4 Spontaneous Quantum Hall States		76
4.1	Spontaneous quantum Hall states	77

4.1.1	Introduction	77
4.1.2	Classification of broken symmetry states	78
4.1.3	Hall conductivities and orbital magnetizations	80
4.1.4	Edge states	84
4.1.5	Discussion	85
4.2	Deformation of edge states	88
4.2.1	Landau levels	88
4.2.2	Electric field effects	90
4.2.3	Edge states along domain walls	92
4.2.4	Discussion	94
4.3	Distinguish spontaneous quantum Hall states in bilayer graphene	96
4.3.1	Introduction	96
4.3.2	Continuum model mean-field theory	98
4.3.3	Influence of Zeeman field	100
4.3.4	Influence of electric field	103
4.3.5	Discussion	104
Chapter 5 Broken $SU(12)$ Symmetry Quantum Hall Ferromagnets		107
5.1	Introduction	108
5.2	Quantum Hall ferromagnetism in ABC trilayer graphene	110
5.3	Quantum Hall ferromagnetism in ABA trilayer graphene	114
Chapter 6 Conclusion		119
6.1	Experimental observations	119
6.2	Future directions	123
Bibliography		127

Vita

136

List of Tables

2.1	SWM hopping parameters	23
3.1	Contrasting contributions from three one-loop diagrams	49
3.2	Influence of trigonal warping and external potential	59
4.1	Summary of spontaneous quantum Hall states	81
4.2	Attributes of distinct $\nu = 0$ states	97

List of Figures

2.1	Schematic of ABC-stacked trilayer graphene	13
2.2	Schematic of hoppings from A_1 to B_3	18
2.3	Band structure of gapless ABC trilayer graphene	19
2.4	Band structure fit for ABC trilayer graphene	22
2.5	Contour plots of the ABC trilayer conduction band	24
2.6	Trigonometric relationship for ABC trilayer graphene	25
2.7	Conduction band contour plots of graphite valued ABC trilayers	26
2.8	Band structure of gapped ABC trilayer graphene	27
2.9	Potential screening and energy gap evolution	28
2.10	Screening effect in different chiral- N systems	33
3.1	Lattice and band structures of bilayer graphene	40
3.2	One-loop Feynman diagrams	42
3.3	ZS and ZS' channels	45
3.4	Singlet propagation in BCS channel	47
3.5	Triplet propagation in BCS channel	47
3.6	Interaction channels for a system with one $1/2$ -pseudospin	51
3.7	Interaction channels for a system with two $1/2$ -pseudospins	52
3.8	RG flows of distinct interaction parameters	55

3.9	Pseudospin susceptibility diagram	61
3.10	Mean-field pseudospin orientation	63
3.11	Spectrum with trigonal warping	68
3.12	Gapless spectra with nematic orders	70
3.13	Spectrum of bilayer graphene with layer displacement	71
3.14	Gapped bilayer graphene without trigonal warping	73
3.15	Gapped bilayer graphene with trigonal warping	74
4.1	Schematic Hall conductivity contributions	79
4.2	Berry curvature of spontaneous quantum Hall states	82
4.3	Orbital moments for chiral graphene with spontaneous gaps	83
4.4	Spontaneous quantum Hall edge states	86
4.5	Landau levels of spontaneous quantum Hall states	89
4.6	Electric field induced phase transition	91
4.7	Edges states along domain walls	93
4.8	Non-collinear LAF order	100
4.9	Canted LAF state quasiparticle bands	102
4.10	Influence of electric field on SQH states	104
5.1	Sketches of graphene trilayers	109
5.2	Spectrum of QHF in ABC trilayer graphene	113
5.3	Spectrum of QHF in ABA trilayer graphene	116
6.1	Raman spectroscopy of trilayer graphene	119
6.2	Spontaneous gap in suspended bilayer graphene	120
6.3	Evolution of bilayer spontaneous gap with external fields	121
6.4	Spontaneous gap in suspended ABC trilayer graphene	122

Chapter 1

Introduction

1.1 Few-layer graphene

Recent progress[1–3] in the isolation of nearly perfect monolayer and multilayer graphene sheets has opened up a new topic in two-dimensional electron systems (2DES) physics. Graphene 2DES's are remarkable for several different reasons. The fact that they are truly two-dimensional (2D) on an atomic length scale elevates 2DES physics from the low-temperature world to the room-temperature world. Furthermore, they are accurately described by very simple models over very wide energy ranges and yet have electronic properties that can be qualitatively altered simply by stacking them in different arrangements[4–7]. In other words, each graphene few-layer is a unique 2DES with fascinating electronic properties depending on its layer number and stacking order.

The basic building block of all graphene 2DES's is the isolated monolayer, which is described by a massless Dirac $\vec{k} \cdot \vec{p}$ Hamiltonian over a very wide energy range ~ 3 eV. The massless Dirac model has chiral quasiparticles and perfect linear

dispersions down to Dirac points. In the graphene case the chirality refers to the relationship between the $\vec{k} \cdot \vec{p}$ momentum and the direction of a pseudospin associated with the sublattice degree-of-freedom of graphene's honeycomb lattice, that is closely related to the π Berry's phase gained by a quasiparticle circling around a Dirac point[8, 9]. Most of the exotic graphene properties directly involve the low-energy physics close to the Dirac points where the conduction and valence bands kiss each other and where the Fermi level lies for the charge neutral case. When these honeycomb layers are stacked together, their low-energy electronic properties are strongly modified in a way that is controlled by the stacking order and the number of layers. Among all the possibilities, we find that only the ABC (chiral) arrangement maintains the following fascinating features[6]: (i) there are two low-energy sublattice sites, implying that a two band model provides a useful tool to describe its physics; (ii) the low energy sublattice sites are localized in the outermost layers, at A_1 and B_N , and can be separated energetically by an electric field perpendicular to the film which breaks the inversion symmetry and opens an energy gap at Dirac points; (iii) hopping between low energy sites via high energy states is an N -step process which leads to p^N dispersion in conduction and valence bands, sublattice pseudospin chirality N and Berry's phase $N\pi$; (iv) the low energy Hamiltonian of a multilayer with any type of stacking can always be chiral-decomposed to a direct sum of ABC-stacked layers; (v) The low-energy bands are increasingly flat for larger N , at least when weak remote hopping processes are neglected, and the opportunity for interesting interaction and disorder physics is therefore stronger. Consequently, in the simplified chiral model, the density-of-states $D(E) \sim E^{(2-N)/N}$ diverges as E approaches zero for $N > 2$ whereas it remains finite for $N = 2$ and vanishes for $N = 1$, which means interactions are more and more relevant as the number of layer increases. ABC-stacked multilayers are the chiral generalizations

of monolayer and bilayer graphene, and we believe that they are likely to prove to be fertile ground for new many-body physics[10], as we will show in this thesis.

For a chiral graphene with $N > 1$, external potential differences between the top and bottom layers, *e.g.* interlayer electric fields, are strongly screened by charge transfer within the layers, but still open an energy gap at overall neutrality[6]. The created gap increases monotonically with the external interlayer potential difference and saturates around the strongest interlayer hopping energy scale ~ 0.4 eV. On the other hand, when a perpendicular magnetic field is applied, these chiral 2DES's are driven into quantum Hall region with $4N$ -fold zero energy Landau levels. We predict[11] that Coulomb interactions spontaneously break the $SU(4N)$ symmetry and drive quantum Hall effects at all the integer fillings ν from $-2N$ to $2N$ with exotic spin and pseudospin polarizations. Unlike a conventional 2DES, both the magnetic field at which the chiral bands are quantized into Landau levels and the critical field where the broken symmetry physics occurs are typically smaller than 1 T for high quality suspended bilayer graphene and its thicker chiral cousins[12, 13]. These unusual phenomena in the presence of external fields, either electrically or magnetically, are directly related to the following weak repulsive interaction instabilities[10, 14] at zero fields.

Remarkably flat conduction and valence bands that touch at charge neutrality point and Bloch states with large pseudospin chirality combine to make the bilayer graphene gapless band state strongly susceptible to a family of broken symmetry states in which each spin-valley flavor spontaneously transfers charge between layers[9]. The underlying many-body physics can be explained elegantly by perturbative renormalization group (PRG) analysis[10], analogous to the well known non-Fermi-liquid states, interacting one-dimensional (1D) electron systems, where the Fermi-surface consists of points, and divergences associated with low-

energy particle-hole excitations abound. Actually, electron-electron interactions in 2D bilayer graphene behave in many ways as if they were 1D, because they have Fermi points instead of Fermi lines and because their particle-hole energies have a quadratic dispersion which compensates for the difference between 1D and 2D phase space. However, the detail PRG calculations prove that the interactions in bilayer graphene are marginally relevant at one-loop level. Because of the large layer pseudospin chirality, the broken symmetry occurs in the perpendicular \hat{z} channel rather than the in-plane $\hat{\phi}$ channel[14, 15], which indicates in each spin-valley, layer inversion symmetry is spontaneously broken[10] while in-plane rotational symmetry is not that reduced. Similar instabilities and broken symmetry physics also occur in bilayer's thicker cousins, chirally stacked multilayer graphene systems.

Because of spontaneously breaking inversion symmetries, in a single spin-valley of chiral N -layer graphene with $N \geq 2$, the Dirac point is gapped with layer polarization and the momentum-space Berry curvature becomes nontrivial[9]. The broken symmetry states are thus able to be classified by their spin-valley flavor dependent layer polarization, by their orbital magnetizations and by their other topological properties, such as various Hall conductivities and edge states[9]. More interestingly, these topologically nontrivial states exhibit non-collinear spin flop influenced by Zeeman fields that couple to spin and undergo a first order transition induced by interlayer electric fields that couple to layer pseudospin[16]. And indeed, these competing spontaneous quantum Hall states are able to be identified and distinguished using response and edge state signatures.

The required access to the low-energy and many-body physics in high quality graphene few-layer samples has been enabled by removing the underlying substrates and further annealing the devices. Not only the electric field induced energy gap and the quantum Hall physics have been extensively explored in experiments,

but also, more excitingly, the spontaneous gaps and insulating broken symmetry states have been recently observed in suspended bilayer[13, 17–19] and trilayer[19] graphene which have started to exhibit spontaneous quantum Hall effects[9, 20]. We expect that even richer novel physics occurs near the charge neutrality point of few-layer graphene, due to the interplay between electron-electron interactions, disorders, and external fields.

1.2 Outline of the thesis

This thesis basically is a collection of my Ph.D papers [6, 9–11, 13, 14, 16, 19, 21–25] from the spring of 2010 to the summer of 2011. Here we give a preview of the materials contained in this thesis work and its organization:

In chapter 2 [6] we introduce the chirally (ABC) stacked few-layer graphene 2DES's and specifically we investigate the band structures of chiral trilayer graphene. We derive the low-energy continuum model, and extract the parameters of a π -band tight-binding model by fitting our *ab initio* density-functional theory results to the effective model. We also study the interlayer electric field related screening effects and induced energy gaps, comparing the chiral 2DES's with different number of layers.

In chapter 3 [10, 14] we use perturbative renormalization group to study the weak repulsive interaction instability in bilayer graphene and to access the robustness of this instability, comparing with the closely related case of interacting 1D electron gas. We predict that the spontaneous gap opening and layer inversion symmetry breaking is enhanced by quantum fluctuations and spin-valley flavors but that, because of trigonal warping, it may occur only in high quality suspended bilayers. Furthermore, we calculate the layer pseudospin susceptibilities, compare

the divergences in different possible broken symmetry channels, and further confirm the inversion symmetry breaking physics that occurs in bilayer graphene and its thicker cousins, chirally stacked multilayer graphene 2DES's.

In chapter 4 [9, 16, 21, 22] we explore the momentum-space Berry curvature of various insulating broken symmetry states to which chiral few-layer graphene is strongly susceptible, and find that these non-Fermi-liquids exhibit spontaneous quantized anomalous Hall effects with spin-valley flavor transfers between layers. We explain how these states are distinguished by their charge, spin, and valley Hall conductivities, by their orbital magnetizations, and by their edge state properties. We investigate how the spontaneous quantum Hall edge states deform in the presence of electric fields and magnetic fields. We further analyze how these competing states are influenced by Zeeman fields that couple to spin and by interlayer electric fields that couple to layer pseudospin, and comment on the possibility of using response and edge state signatures to identify the character of the bilayer ground state experimentally.

In chapter 5 [11] we study the stacking-dependent interaction-driven quantum Hall effects in ABC and ABA trilayer graphene. Particularly, we investigate the zeroth Landau level that is 12-fold degenerate in the absence of interactions and external fields. We predict that Coulomb interactions spontaneously break the $SU(12)$ symmetry and drive quantum Hall effects at all the integer fillings ν from -6 to 6 with exotic spin and pseudospin polarizations. We also discuss the interlayer electric field driven phase transition between the spin- and layer(valley)-polarized $\nu = 0$ states in ABC trilayers, and address the pronounced influence of the next-nearest layer tunnelings in ABA trilayers.

In chapter 6 [13, 19, 25] we conclude this thesis work by discussing the recent experimental observations of insulating broken symmetry states and sponta-

neous quantum Hall effects in high quality suspended bilayer and trilayer graphene.
We also discuss some potential future works.

Chapter 2

Band Structure of ABC-Stacked Graphene Few-Layers

The ABC-stacked N -layer-graphene family of two-dimensional electron systems is described at low energies by two remarkably flat bands with Bloch states that have strongly momentum-dependent phase differences between carbon π -orbital amplitudes on different layers, and large associated momentum space Berry phases. These properties are most easily understood using a simplified model with only nearest-neighbor inter-layer hopping which leads to gapless semiconductor electronic structure and p^N dispersion in both conduction and valence bands. In this chapter, we report on a study of the electronic band structures of trilayers which uses *ab initio* density functional theory and $\mathbf{k} \cdot \mathbf{p}$ theory to fit the parameters of a π -band tight-binding model. We find that when remote interlayer hopping is retained, the triple Dirac point of the simplified model is split into three single Dirac points located along the three KM directions. External potential differences between top and bottom layers are strongly screened by charge transfer within the trilayer, but

still open an energy gap at overall neutrality.

2.1 Introduction

Success[1] in isolating nearly perfect monolayer and few layer sheets from bulk graphite, along with progress in the epitaxial growth of few-layer graphene samples, has led to an explosion of experimental and theoretical[2, 3, 26, 27] interest in this interesting class of quasi-two-dimensional electron systems (2DES's). Unique aspects of the electronic structure of graphene based 2DES's have raised a number of new fundamental physics issues and raised hope for applications.

Monolayer graphene has a honeycomb lattice structure and is a gapless semiconductor. Hopping between its equivalent A and B sublattices gives rise to a massless Dirac fermion band structure with $J = 1$ chirality when the sublattice degree of freedom is treated as a pseudospin. In this chapter we will find it useful to view the quantum two-level degree of freedom associated with two sublattice sites as a pseudospin in the multi-layer case as well. In AB-stacked graphene bilayers, for example, electrons on the A_2 and B_1 sublattices are repelled from the Fermi level by a direct interlayer tunneling process with energy γ_1 , leaving[4] only states that are concentrated on the A_1 and B_2 sites in the low-energy band-structure projection. When direct hopping between A_1 and B_2 sites is neglected, the two-step hopping process via high energy sites leads to p^2 conduction and valence band dispersions and to a pseudospin chirality that is doubled, *i.e.* to a phase difference between sublattice projections which is proportional to $2\phi_p$ where ϕ_p is the two-dimensional momentum orientation. Pseudospin chirality has a substantial influence on interaction physics[28] in both single-layer and bilayer graphene, and through the associated momentum space Berry phases also on Landau quantization and the integer

quantum Hall effect[4, 5, 29–31]. Because the two low-energy sublattices in bilayer graphene are located on opposite layers it is possible to introduce[32–36] a gap[37–44] in the electronic structure simply by using gates to induce a difference in electric potential between layers. According to some theories a small gap could even emerge spontaneously[10, 15, 45–48] in neutral graphene bilayers with weak disorder because of layer inversion symmetry-breaking.

Graphene bilayer 2DES's are quite distinct from single layer 2DES's because of their flatter band dispersion and the possibility of using external potentials to create gaps. Among all stacking possibilities, only the ABC arrangement (see below) maintains the following features that make Bernal bilayer electronic structure interesting in thicker N -layer films: (i) there are two low-energy sublattice sites, implying that a two band model provides a useful tool to describe its physics; (ii) the low energy sublattice sites are localized in the outermost layers, at A_1 and B_N , and can be separated energetically by an electric field perpendicular to the film; (iii) hopping between low energy sites via high energy states is an N -step process which leads to p^N dispersion in conduction and valence bands, sublattice pseudospin chirality N and Berry phase $N\pi$. The low-energy bands are increasingly flat for larger N , at least when weak remote hopping processes are neglected, and the opportunity for interesting interaction and disorder physics is therefore stronger. Consequently, in the simplified chiral model, the density-of-states $D(E) \sim E^{(2-N)/N}$ diverges as E approaches zero for $N > 2$ whereas it remains finite for $N = 2$ and vanishes for $N = 1$. These properties also have some relevance to more general stacking arrangements since the low energy Hamiltonian of a multilayer with any type of stacking can always be chiral-decomposed to a direct sum of ABC-stacked layers[5].

ABC-stacked multilayers are the chiral generalizations of monolayer and Bernal bilayer graphene, and we refer them collectively as the chiral 2D electron

system (C2DES) family. We believe that they are likely to prove to be fertile ground for new physics. As a first step in the exploration of these materials we report in this chapter on an effort to characterize the way in which the chirality N bands of an N -layer C2DES are altered by remote hopping processes neglected in the simplified model, focusing on the $N = 3$ trilayer case. We use *ab initio* density functional theory (DFT) calculations, combined with a $\mathbf{k} \cdot \mathbf{p}$ expansion of the low-energy bands near the Dirac point, to fit the parameters of a phenomenological tight-binding method (PTBM) for the π -bands of multilayer graphene.[5, 7, 49–51] We find that details of the low-energy band dispersion can be used to fix rather definite values for the model’s remote inter-layer hopping parameters.

This chapter is organized as follows. In section II we first sketch the derivation of the low energy effective band Hamiltonian of a trilayer, reserving details to an Appendix and explain how the interlayer hopping parameters influence the shape of constant energy surfaces. The values for these parameters obtained by fitting to our DFT calculations are surprisingly different from the values for the analogous hopping parameters in Bernal stacked layers, and are not yet available from experiment. In Section II we also discuss the evolution of constant energy surface pockets with energy, concentrating on the Lifshitz transitions at which pockets combine, in terms of Berry phase considerations and a competition between chiral dispersion and trigonal warping. In section III we use DFT to estimate the dependence of the trilayer energy gap on the external potential difference between top and bottom layers and compare with predictions based on the simplified two-band model. The simplified model picture is readily extended to higher N and we use it to discuss trends in thicker ABC multilayers. Finally, we conclude in Section IV with a discussion of how Berry phases modify the integer quantum Hall effect and weak localization in C2DES’s and with some speculations on the role of electron-electron

interactions in these two-dimensional materials.

2.2 Effective model

2.2.1 Low-energy effective model

In ABC-stacked graphene layers, each layer has inequivalent triangular A and B sublattices. As illustrated in Fig. 2.1(a), each adjacent layer pair forms a AB-stacked bilayer with the upper B sublattice directly on top of the lower A sublattice, and the upper A above the center of a hexagonal plaquette of the layer below. Our microscopic analysis uses the categorization of interlayer hopping processes illustrated in Fig. 2.1(b), which is analogous to the Slonczewski-Weiss-McClure (SWM) parametrization of the tight binding model of bulk graphite with the Bernal stacking order[52]. Following convention γ_0 and γ_1 describe nearest neighbor intralayer and interlayer hopping respectively, γ_3 represents hopping between the low energy sites of a AB-stacked bilayer (*i.e.* $A_i \leftrightarrow B_{i+1}$ ($i = 1, 2$)), γ_4 couples low and high energy sites located on different layers (*i.e.* $A_i \leftrightarrow A_{i+1}$ and $B_i \leftrightarrow B_{i+1}$ ($i = 1, 2$)). We use γ_2 to denote direct hopping between the trilayer low energy sites, and δ as the on-site energy difference of A_1 and B_3 with respect to the high energy sites. γ_5 and γ_6 correspond to the presumably weaker couplings $B_1 \leftrightarrow A_3$ and $S_1 \leftrightarrow S_3$ ($S = A, B$), respectively and u_i is used to denote the average potential of the i th layer.

The massless Dirac-Weyl quasiparticles of monolayer graphene are described by a $\vec{k} \cdot \vec{p}$ Hamiltonian,

$$\hat{H} = v_0 \begin{pmatrix} 0 & \pi^\dagger \\ \pi & 0 \end{pmatrix}, \quad (2.1)$$

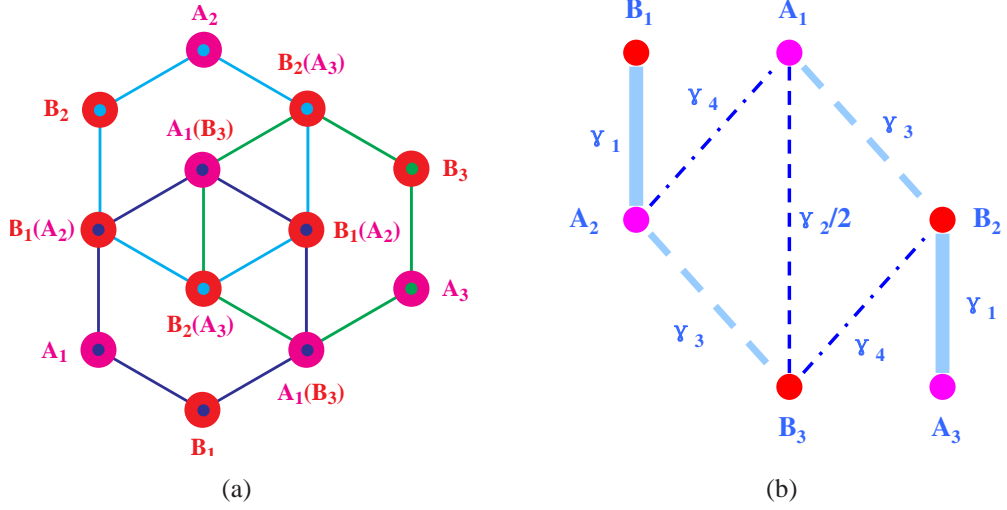


Figure 2.1: (a) Lattice structure of ABC-stacked graphene trilayer; blue/cyan/green indicate links on the top/middle/bottom layers while purple/red distinguish the A/B sublattices. (b) Schematic of the unit cell of ABC-stacked graphene trilayer and the most important interlayer hopping processes.

where $\pi = \xi p_x + i p_y$ and $\xi = +(-)$ for valley $K(K')$. (In this chapter we focus on bands near Brillouin zone corner K ; the general result can be obtained by setting p_x to ξp_x .) The trilayer π -bands are the direct produce of three sets of monolayer bands, modified by the various interlayer coupling processes identified above. In a representation of sublattice sites in the order $A_1, B_3, B_1, A_2, B_2, A_3$, the trilayer Hamiltonian near valley K can then be expressed in the form:

$$\hat{\mathcal{H}}_{\text{trilayer}}^{\text{ABC}} = \begin{pmatrix} u_1 + \delta & \frac{1}{2}\gamma_2 & v_0\pi^\dagger & v_4\pi^\dagger & v_3\pi & v_6\pi \\ \frac{1}{2}\gamma_2 & u_3 + \delta & v_6\pi^\dagger & v_3\pi^\dagger & v_4\pi & v_0\pi \\ v_0\pi & v_6\pi & u_1 & \gamma_1 & v_4\pi^\dagger & v_5\pi^\dagger \\ v_4\pi & v_3\pi & \gamma_1 & u_2 & v_0\pi^\dagger & v_4\pi^\dagger \\ v_3\pi^\dagger & v_4\pi^\dagger & v_4\pi & v_0\pi & u_2 & \gamma_1 \\ v_6\pi^\dagger & v_0\pi^\dagger & v_5\pi & v_4\pi & \gamma_1 & u_3 \end{pmatrix}, \quad (2.2)$$

where $v_i = \sqrt{3}a\gamma_i/2\hbar$ and $a = 0.246\text{nm}$.

The identification of A_1 and B_3 as the low-energy sublattice sites is made by neglecting the weaker remote interlayer hopping processes and setting $\pi \rightarrow 0$. We treat coupling between the low and high-energy subspaces perturbatively by writing the trilayer Greens function as

$$\mathcal{G} = (\hat{\mathcal{H}}_{\text{trilayer}}^{\text{ABC}} - \varepsilon)^{-1} = \begin{pmatrix} H_{11} - \varepsilon & H_{12} \\ H_{21} & H_{22} - \varepsilon \end{pmatrix}^{-1} \quad (2.3)$$

where the indices 1 and 2 denote the 2×2 low-energy block and the 4×4 high-energy block respectively. We then solve the Schrödinger equation, $(\mathcal{G})_{11}^{-1}\psi_{\text{low}} = 0$, by using the block matrix inversion rule $(A^{-1})_{11} = (A_{11} - A_{12}(A_{22})^{-1}A_{21})^{-1}$ to obtain

$$((H_{11} - \varepsilon) - H_{12}(H_{22} - \varepsilon)^{-1}H_{21})\psi_{\text{low}(A_1, B_3)} = 0. \quad (2.4)$$

Since we are interested in the low-energy part of the spectrum we can view ε as small compared to H_{22} . Expanding Eq. (2.4) to first order in ε , we find that $(H_{\text{eff}} - \varepsilon)\psi_{\text{low}} = 0$, where

$$H_{\text{eff}} = (1 + H_{12}(H_{22})^{-2}H_{21})^{-1}(H_{11} - H_{12}(H_{22})^{-1}H_{21}). \quad (2.5)$$

The terms in the second parenthesis capture the leading hopping processes between low energy sites, including virtual hopping via high-energy states, while the first parenthesis captures an energy scale renormalization by a factor of order $1 - (v_0\rho/\gamma_1)^2$ due to higher-order processes which we drop except in the terms which arise from an external potential.

Using Eq. (2.5) we find that for ABC trilayer graphene

$$\begin{aligned}
\hat{H}_{\text{eff}} &= \hat{H}_{\text{ch}} + \hat{H}_{\text{s}} + \hat{H}_{\text{tr}} + \hat{H}_{\text{gap}} + \hat{H}'_{\text{s}}, \\
\hat{H}_{\text{ch}} &= \frac{v_0^3}{\gamma_1^2} \begin{pmatrix} 0 & (\pi^\dagger)^3 \\ \pi^3 & 0 \end{pmatrix} \\
&= \frac{(v_0 p)^3}{\gamma_1^2} (\cos(3\varphi_{\mathbf{p}}) \sigma_x + \sin(3\varphi_{\mathbf{p}}) \sigma_y), \\
\hat{H}_{\text{s}} &= \left(\delta - \frac{2v_0 v_4 p^2}{\gamma_1} \right) \sigma_0, \\
\hat{H}_{\text{tr}} &= \left(\frac{\gamma_2}{2} - \frac{2v_0 v_3 p^2}{\gamma_1} \right) \sigma_x, \\
\hat{H}_{\text{gap}} &= u_{\text{d}} \left(1 - \left(\frac{v_0 p}{\gamma_1} \right)^2 \right) \sigma_z, \\
\hat{H}'_{\text{s}} &= \frac{u_{\text{a}}}{3} \left(1 - 3 \left(\frac{v_0 p}{\gamma_1} \right)^2 \right) \sigma_0.
\end{aligned} \tag{2.6}$$

Here we have chosen $\tan \varphi_{\mathbf{p}} = p_y/p_x$, defined $u_{\text{d}} = (u_1 - u_3)/2$ and $u_{\text{a}} = (u_1 + u_3)/2 - u_2$, and neglected an overall energy scale associated with the external potentials. σ_0 is the identity matrix and the σ_i 's are Pauli matrices acting on the low-energy pseudospin. We have retained leading terms with cubic, quadratic, and constant dispersions, which are due respectively to three-step, two-step, and one-step hopping processes between low energy sites. For trilayer graphene, the linear term is absent because the one step hopping (γ_2) is normal to the 2D space and therefore independent of momentum. \hat{H}_{ch} is the only term which appears in the effective Hamiltonian in the simplified model with only nearest neighbor inter-layer tunneling. This term has pseudospin chirality $J = 3$ and dominates at larger values of p . It reflects coupling between low energy sites via a sequence of three nearest neighbor intralayer and interlayer hopping events. \hat{H}_{tr} is proportional to σ_x and,

because it is isotropic in 2D momentum space, is responsible for trigonal warping of constant energy surfaces when combined with the $J = 3$ chiral term. Notice that the direct hopping γ_2 process opens a small gap at the K points so that \hat{H}_{tr} vanishes at finite p if γ_2 is positive. \hat{H}_s arises from a weaker coupling between low energy and high energy states that is present in bilayers and for any $N > 1$ multilayer system. This term in the effective Hamiltonian preserves layer inversion symmetry. \hat{H}_{gap} captures the external potential processes which break layer inversion symmetry and introduce a gap between electron and hole bands. The possibility of opening a gap with an external potential is unique to ABC stacked multilayers, increasing the possibility that they could be useful materials for future semiconductor devices. The strength of the gap term decreases with increasing momentum (since $v_0 p \ll \gamma_1$) so that the gap around K has a Mexican hat shape, as we will discuss later. \hat{H}'_s is non-zero when the potential of the middle layer deviates from the average of the potentials on the outermost layers. Unlike \hat{H}_{gap} , this term preserves the layer inversion symmetry and is not responsible for an energy gap. A non-zero \hat{H}'_s is relevant when the electric fields in the two inter-layer regions are different. Further discussion on the derivation of this effective Hamiltonian and on the physical meaning of the various terms can be found in the Appendix. Note that for strict consistency the constant terms δ and $\gamma_2/2$ should be accompanied by the factor $1 - (v_0 p)^2/\gamma_1^2$ based on Eq. (2.5) which does appear in \hat{H}_{gap} . However we ignore this factor because δ and $\gamma_2/2$ are already small.

2.2.2 Diagrammatic derivation of the effective model

As a result of tight-binding model, each term of the effective Hamiltonian Eq. (2.6) has a unique physical picture. Hereafter, we view the strongly stacked pair $B_i A_{i+1}$

as a single dimer site and assume zero external potentials for simplicity. The general formula of effective low energy models Eq. (2.5) can be understood as following. The terms in the second parenthesis represent the leading hopping processes, while the terms in the first parenthesis are approximately $1 - (v_0 p / \gamma_1)^2$ and give a small correction. H_{11} is the unperturbed Hamiltonian of low energy sites and thus includes the direct hopping and on-site energy. H_{21} and H_{12} are hoppings from and to low energy sites, respectively, describing the coupling to high energy ones. H_{22} contains the hoppings between high energy sites and is an intermediate process. Therefore $H_{12}(H_{22})^{-1}H_{21}$ together gives the general “three”-step hoppings which start from and end at low energy sites by way of high energy ones. Note that the intermediate process within high energy sites is zero for single layers, a constant for bilayers, one-step for trilayers, and multi-step for $N \geq 3$ layers. In bilayers for example, the linear trigonal warping term arises from H_{11} , while the chiral term attributes to $H_{12}(H_{22})^{-1}H_{21}$. Because H_{22} gives no hopping and is simply γ_1 , $H_{12}(H_{22})^{-1}H_{21}$ is reduced to two-step and hence the chiral term is quadratic. In the trilayer case, for the matrix element B_3A_1 , H_{11} provides the first term of \hat{H}_{tr} shown in Fig. 2.2(a) while $H_{12}(H_{22})^{-1}H_{21}$ contributes \hat{H}_{ch} and the second term of \hat{H}_{tr} as depicted in Fig. 2.2(b)-2.2(d), respectively. $H_{12}(H_{22})^{-1}H_{21}$ also gives rise to the second term of \hat{H}_{s} for the matrix element A_1A_1 as presented in Fig. 2.2(e) and 2.2(f).

Generally, in order to derive the low energy effective model for a general ABC-stacked N -layer graphene, we first need to write a $2N \times 2N$ Hamiltonian matrix as Eq. (2.2), then we specify all the leading hopping processes in the diagrammatic language like Fig. 2.2, instead of inverting the large Hamiltonian matrix. The hopping diagrams are convenient for systematic calculations in a way similar to the way Feynman diagrams help in perturbation theories. The exact coefficient

of one hopping process can be easily calculated using Eq. (2.5) by picking up the

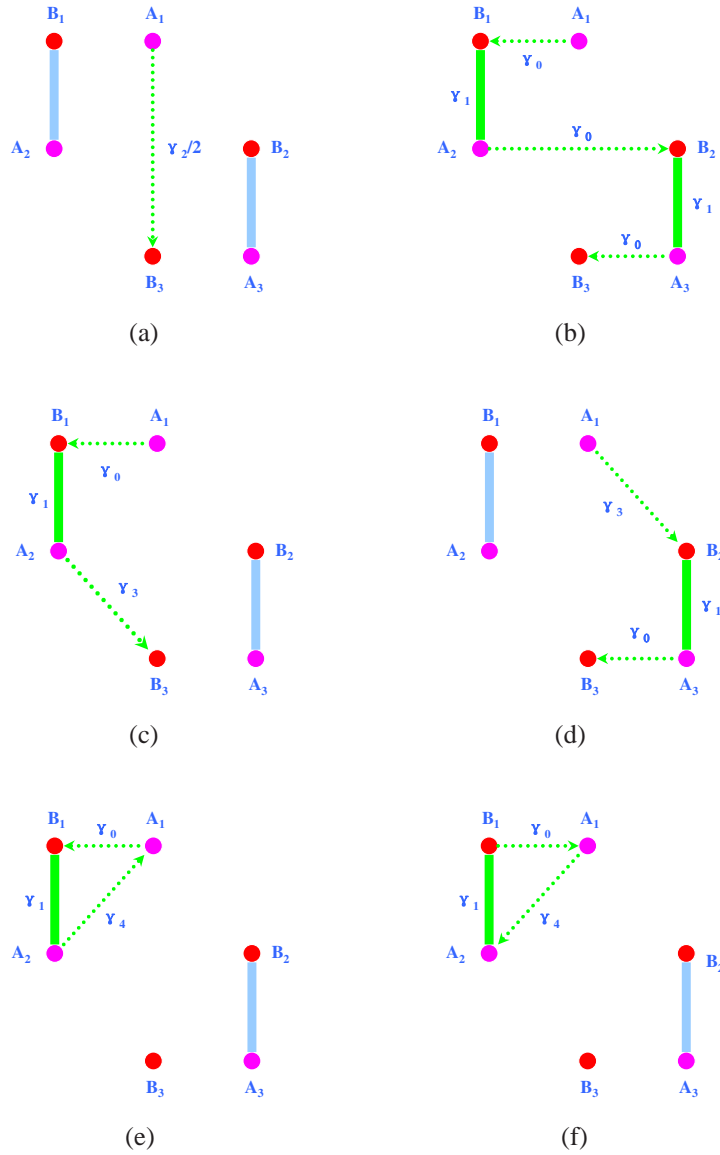


Figure 2.2: Schematic of hoppings from A_1 to B_3 ; (a) one-step $A_1 \rightarrow B_3$ and (b) three-step $A_1 \rightarrow B_1A_2 \rightarrow B_2A_3 \rightarrow B_3$ and (c) (d) two-step $A_1 \rightarrow B_1A_2 \rightarrow B_3$ and $A_1 \rightarrow B_2A_3 \rightarrow B_3$. Schematic of hoppings from A_1 to A_1 ; (e) two-step $A_1 \rightarrow B_1A_2 \rightarrow A_1$ and (f) two-step $A_1 \rightarrow A_2B_1 \rightarrow A_1$.

starting and ending sites, setting matrix elements of unrelated sites as zero and turning off the unrelated hopping parameters. Frequently, one hopping process can be neglected because its requirement of more than one sub-hopping with comparably small amplitudes.

2.2.3 *Ab initio* density-functional theory calculations

We have performed *ab initio* DFT calculations[53] for an isolated graphene trilayer in the absence of a transverse external electric field which induces an electric potential difference between the layers. (DFT calculations in the presence of electric fields will be discussed in the next section.) Our electronic structure calculation-

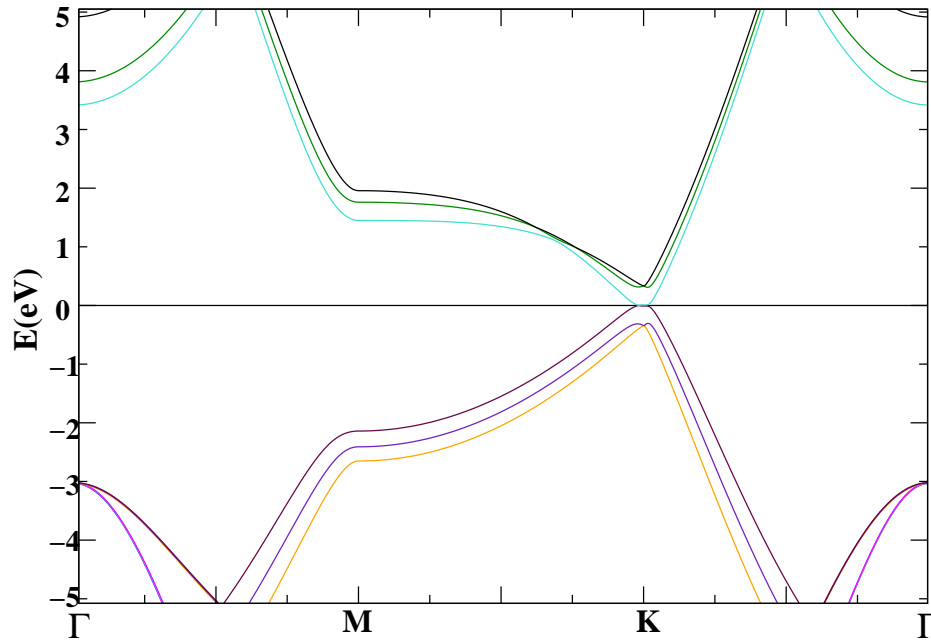


Figure 2.3: Band structure of ABC-stacked graphene trilayers in the absence of an external electric field. The zero of energy in this plot is at the Fermi energy of a neutral trilayer. Notice the single low-energy band with extremely flat dispersion near the K point.

s were performed with plane wave basis sets and ultrasoft pseudopotentials [54]. The local density approximation (LDA) was used for the exchange and correlation potential. We have used the layer separation at the experimental value 0.335 nm, instead of allowing relaxation, because the layer separation is known to depend on Van der Waals interactions that are not captured by the LDA. We note that the main role of the Van der Waals interactions is to anchor the layers at a fixed distance through its influence on the overall energy[55, 56]. Although DFT with local or semi-local approximations does not reliably predict interlayer separations, the electronic structure at a given layer separation is not strongly influenced by Van der Waals forces[55, 56]. We placed bulk trilayer graphene in a supercell with a 40 nm vacuum region, large enough to avoid intercell interactions. A $21 \times 21 \times 1$ \mathbf{k} -point mesh in the full supercell Brillouin zone (FBZ) was used with a 408 eV kinetic energy cut-off. The calculations were tested for large \mathbf{k} -point meshes in the FBZ and large energy cut-offs for convergence studies. Fig. 2.3 shows the DFT energy band structure of ABC stacked trilayer graphene in the absence of an external electric field. The low energy band dispersion is nearly cubic at the two inequivalent corners K and K' of the hexagonal Brillouin zone, as predicted by the π -orbital tight-binding and continuum model phenomenologies. The conduction and valence bands meet at the Fermi level. Close enough to Fermi level the band is nearly flat, which indicates the important role interactions might play in this material.

2.2.4 Extracting hopping parameters from DFT

Previously, bulk graphite (with the Bernal stacking order) SWM hopping parameters have been extensively studied using DFT and measured in experiments. However, the values of the SWM parameters appropriate for ABC-stacked trilayer graphene

were previously unknown. We extract their values by fitting the effective model with the DFT data in the zero electric field limit. The eigenenergies of the Hamiltonian in Eq. (2.6) in the absence of external potentials are

$$E^{(\pm)} = h_s \pm \sqrt{h_{\text{ch}}^2 + h_{\text{tr}}^2 + 2 \cos(3\varphi_{\mathbf{p}}) h_{\text{ch}} h_{\text{tr}}}, \quad (2.7)$$

where $h_{\text{ch}} = (v_0 p)^3 / \gamma_1^2$, $h_{\text{tr}} = \gamma_2 / 2 - 2v_0 v_3 p^2 / \gamma_1$ and $h_s = \delta - 2v_0 v_4 p^2 / \gamma_1$. To extract the remote hopping parameters we first set the nearest neighbor in-plane hopping parameter γ_0 to 3.16 eV to set the overall energy scale. The values of δ and, up to a sign, γ_2 can then be obtained by comparing the band energies at $p = 0$ calculated by the two different methods. Then comparing $E^{(+)} + E^{(-)}$ from the DFT data with Eq. (2.7), we obtain a value for $\gamma_4 \gamma_0 / \gamma_1$. Finally we notice that Eq. (2.7) implies that the gap between conduction (+) and valence (−) bands vanishes at $\cos(3\varphi_{\mathbf{p}}) = 1$ if h_{tr} is negative and at $\cos(3\varphi_{\mathbf{p}}) = -1$ if h_{tr} is positive. Because of this property the Fermi level of a neutral balanced ABC trilayer is at the energy of three distinct Dirac points which are removed from the Dirac point separated in direction by $2\pi/3$. The triple Dirac point of the trilayer's simplified model is split into three separate single Dirac points. The DFT theory result that the conduction valence gap vanishes along the $K'M$ directions for which $\cos(3\varphi_{\mathbf{p}}) = 1$ implies that h_{tr} is negative and helps to fix the sign of γ_2 . Values for $\gamma_3 \gamma_0 / \gamma_1$ and γ_0^3 / γ_1^2 are provided by the value of p at the Dirac points and the size of the splitting between conduction and valence bands ($2\sqrt{h_{\text{ch}}^2 + h_{\text{tr}}^2}$) along the $\cos(3\varphi_{\mathbf{p}}) = 0$ directions. The best overall fit we obtained to the bands around the K point and the deformed Dirac cones is summarized in Table 2.1, where we compare with the corresponding fitting parameters for bulk graphite[3, 52]. Our fit is extremely good in the low energy region in which we are interested, as shown in Fig. 2.4, though there are still discrepancies

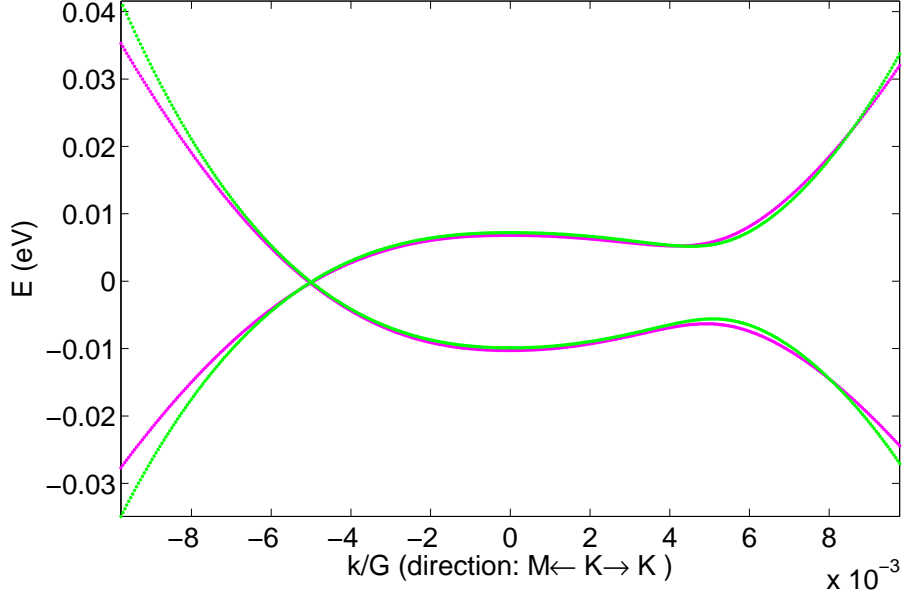


Figure 2.4: The magenta curve is the DFT data while the Green one represents the effective model using the extracted parameters shown in Table 2.1. $G = 4\pi/(\sqrt{3}a)$ is the length of the reciprocal vectors and $k = 0$ is the K point.

as higher energies are approached. These discrepancies are expected because of the perturbative nature of the effective model and can be partly corrected by restoring the $1 - (v_0 p)^2/\gamma_1^2$ correction factor in Eq. (2.5).

2.2.5 Electron(hole) pockets and Lifshitz transitions

With the effective model hopping parameters extracted from DFT we study the shape of the Fermi surface of a graphene trilayer. Fig. 2.5 shows the constant energy contour plot of the electron band around zero energy. Clearly, under remote hopping the $J=3$ Dirac points evolve into three separate $J = 1$ Dirac points symmetrically shifted away a little bit in the KM directions (\hat{k}_x); each shifted Dirac point resembles a linear cone like the ones in monolayer graphene. The property that total

Table 2.1: Summary of SWM hopping parameters obtained by fitting DFT bands in ABC-stacked trilayer graphene to a low-energy effective model. We compare with bulk graphite values from References[3, 52].

Parameters	graphite(eV)	ABC trilayer (eV)
δ	0.008	-0.0014
γ_1	0.39	0.502
γ_3	0.315	-0.377
γ_4	-0.044	-0.099
γ_2	-0.020	-0.0171

chirality is conserved can be established by evaluating Berry phases along circular paths far from the Dirac points where the remote hopping processes do not play an essential role. The Dirac point distortion occurs because the direct hopping γ_2 process does not involve 2D translations and therefore gives a momentum independent contribution to the Hamiltonian which does not vanish at the Brillouin-zone corners. A similar distortion of the simplified-model ideal chirality Dirac point occurs in any $3m$ -layer system of ABC stacked (m is a positive integer) graphene sheets. Around each deformed Dirac cone there is a electron (hole)-like pocket in the conduction(valence) band at low carrier densities and two Lifshitz transitions as a function of carrier density. Take the conduction band for example. As shown in Fig. 2.5, immediately above zero energy, the constant energy surface consists of three separate Dirac pockets. At the first critical energy 6.7 meV, the three electron pockets combine and a central triangle-like hole pocket appears. (Energies are measured from the Fermi energy of a neutral trilayer.) At this energy three band-structure saddle points occur midway between the shifted Dirac points, and thus

the density-of-states diverges. Fermi levels close to these 2D logarithmic van Hove singularities could lead to broken symmetry states. At the second critical energy 7.2 meV, the central pocket and the three remote pockets merge into a single pocket with a smoothed triangle shape. Fig. 2.5 is in excellent agreement with constant energy surfaces constructed directly from our DFT calculations (Figure not shown). The two similar Lifshitz transition energies in the valence band occur at -7.9 meV and -9.9 meV. The constant energy surface at the second Lifshitz transition solves

$$E^{(\pm)}(\mathbf{p} \neq \mathbf{0}) = E^{(\pm)}(\mathbf{p} = \mathbf{0}), \quad (2.8)$$

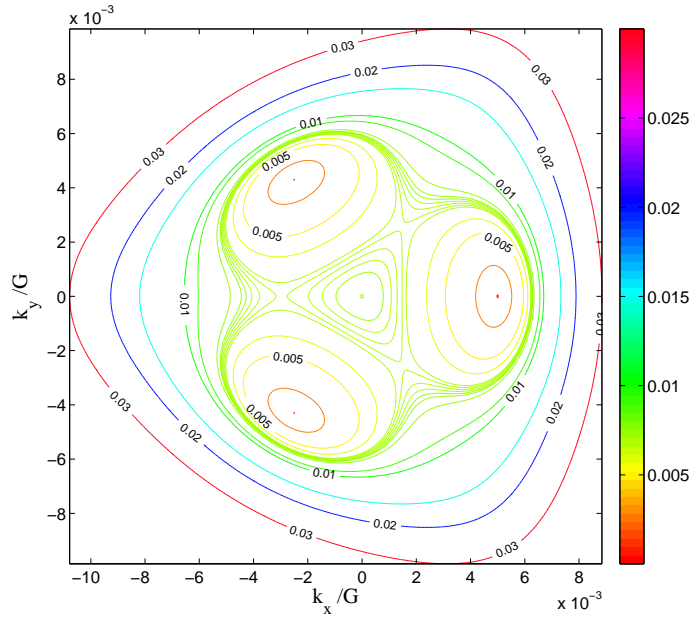


Figure 2.5: Constant energy (in units of eV) contour plots of the conduction band near zero energy for ABC-valued Fermi surfaces of a ABC trilayer. $G = 4\pi/(\sqrt{3}a)$ is the length of the reciprocal vector and $k = 0$ is a K point. The energies of the initial three electron pockets from inner to outer are 0.0, 2.5, 5.0, 6.0, and 6.7 meV; The energies of the central triangles from outer to inner are 6.8, 6.9, 7.0, 7.1 and 7.2 meV; The energies of the bigger triangles from inner to outer are 6.8, 6.9, 7.0, 7.1, 7.2, 7.5, 9.0, 10.0, 15.0, 20.0, and 30.0 meV.

where $+(-)$ refers to conduction and valence band cases. This critical condition can be specified using the law of cosines as shown in Fig. 2.6, where for trilayers $\phi_{\text{Berry}} = 3\pi$ and $h_0 = |\gamma_2/2| \pm 2v_0v_4p^2/\gamma_1$. This momentum-dependent trigonometric condition can be easily generalized to the case of any other graphene multilayer and to the case with an external potential difference. Above the second Lifshitz

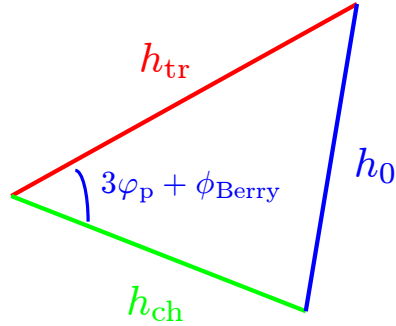


Figure 2.6: A momentum-dependent trigonometric relationship which describes how the shape of the constant energy surfaces near the Lifshitz transitions is collectively governed by chiral dispersion, trigonal warping, and Berry phases.

transition, the constant energy surface is triangular in shape, with a trigonal distortion that differs in orientation compared to the one obtained by plugging the bulk graphite values for the hopping parameters into the same effective model Eq. (2.6) as illustrated in Fig. 2.7. The ABC-stacked trilayer trigonal distortion has a different orientation and is weaker. The difference mainly reflects a difference in the sign of γ_3 , which favors anti-bonding orbitals at low energies. The warping of the constant energy surface becomes hexagonal at $8 \sim 9$ meV, which provides nearly parallel flat pieces on the edges of the hexagon leading to strong nesting. This might support some competing ground states and a density-wave ordered phase might then exist at a small but finite interaction strength. The electronic properties of low-carrier density systems in graphene trilayers will be sensitive to these detailed band fea-

tures. Future ARPES experiments should be able to determine whether or not these features are predicted correctly by our DFT calculations.

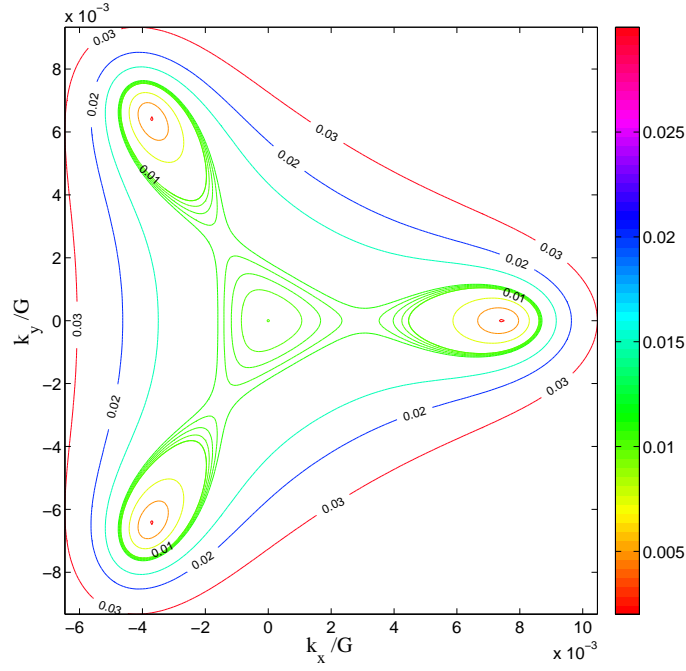


Figure 2.7: Constant energy (in units of eV) contour plots of the conduction band near zero energy for bulk graphite valued Fermi surfaces of a ABC trilayer. $G = 4\pi/(\sqrt{3}a)$ is the length of the reciprocal vector and $k = 0$ is a K point. The energies of the initial three electron pockets from inner to outer are 1.0, 5.0, 7.5, 10.0, 10.2, 10.4 and 10.6 meV; The energies of the central triangles from inner to outer are 10.0, 10.2, 10.4 and 10.6 meV; The energies of the bigger triangles from inner to outer are 10.8, 15.0, 20.0, and 30.0 meV.

2.3 Induced band gaps in trilayers

2.3.1 Energy bands with electric fields

Fig. 2.8 shows the energy band structure of a ABC-stacked graphene trilayer for several external electric potential differences between the outermost layers. In the

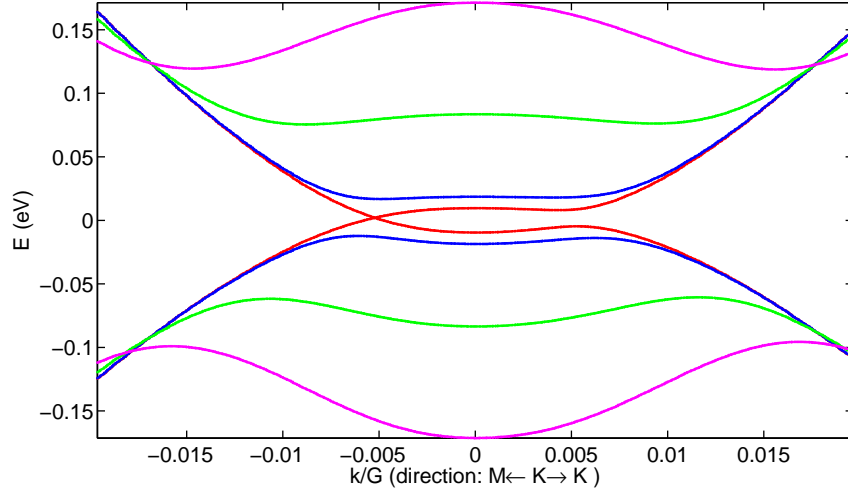
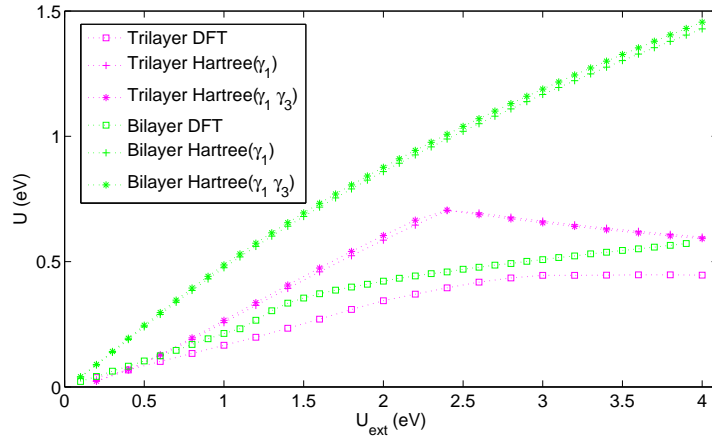


Figure 2.8: The band structures of a ABC graphene trilayer with external electric potential differences between the outermost layers. The external potential difference U_{ext} values are 0.0(red), 0.2(blue), 1.0(green) and 2.0(magenta) eV, respectively. $G = 4\pi/(\sqrt{3}a)$ is the length of the reciprocal vectors and $k = 0$ is a K point.

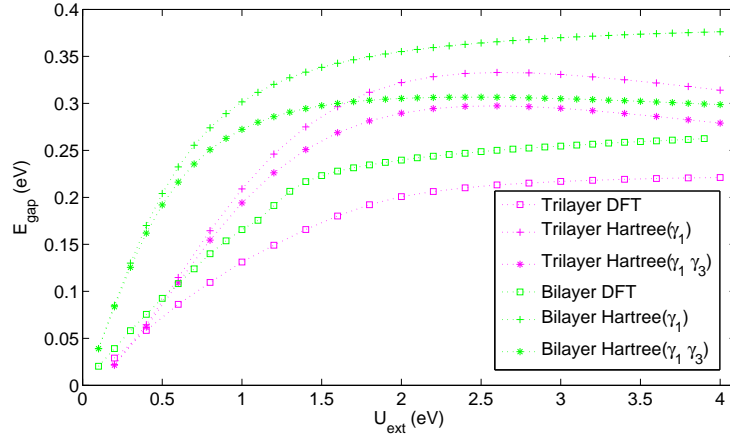
presence of an external field, as in the graphene bilayer case, the energy gap is direct but, because the low-energy spectrum develops a *Mexican hat* structure as the electric potential difference increases, occurs away from the K or K' point. Charge transfer from the high-potential layer to the low-potential layer partially screens the external potential in both bilayer and multilayer cases. Fig. 2.9(a) plots the screened potential U and Fig. 2.9(b) the energy gap, as a function of the external potential U_{ext} for bilayers and trilayers calculated using both DFT and the full band self-consistent Hartree approximation. The simple model Hartree calculations agree quite well with the DFT results generally. We find that the screening is stronger in a trilayer system, and that the maximum energy gap is slightly smaller. In both bilayer and trilayer, remote hopping suppresses the size of the energy gap but make little difference to the screening.

2.3.2 Self-consistent Hartree calculation

As in the bilayer case, it is interesting to develop a theory of gap formation and external potential screening for ABC trilayers by combining the low-energy effec-



(a) Potential Screening



(b) Energy gap evolution

Figure 2.9: Evolution of (a) the screened electric potential difference and (b) the energy gap, with respect to the increase of the external electric potential difference between the outermost layers. \square represents the DFT calculations while \dagger ($*$) denotes the full band self-consistent Hartree calculations without (with) remote hopping γ_3 .

tive model with a Poisson equation which takes Hartree interactions into account. This simplified approach provides a basis for discussing the dependence on layer number for general N . We therefore consider an isolated graphene N -layer with an interlayer separation $d = 0.335\text{nm}$ under an external electric field E_{ext} perpendicular to the layers, neglecting the finite thickness and crystalline inhomogeneity of the graphene layers. In an isolated system charge can only be transferred between layers so that $n = n_t + n_b = 0$. Defining $\delta n = n_b = -n_t$ and using a Poisson equation, we find that the screened electric potential difference U between the outermost layers is

$$U = U_{\text{ext}} + 4\pi e^2(N-1)d\delta n. \quad (2.9)$$

In the two-band effective model, δn is accumulated through the layer pseudospin polarization of the valence band states and is thus given by the following integral over momentum space:

$$\delta n = \sum_{i \in \text{v}} 2 \int_{\text{BZ}} \frac{d^2k}{(2\pi)^2} \langle \psi_i(\mathbf{k}) | \frac{\sigma_z}{2} | \psi_i(\mathbf{k}) \rangle, \quad (2.10)$$

where the factor 2 accounts for spin degeneracy, $|\psi_i(\mathbf{k})\rangle$ is a band eigenstate in the presence of E_{ext} , band index i runs over all the filled valence band states, and $\sigma_z/2$ denotes the layer-pseudospin. Any Hamiltonian of a two-band model can be generally written as $H = h_0(\mathbf{p}) + \mathbf{h}(\mathbf{p}) \cdot \boldsymbol{\sigma}$. Defining $\tan \theta_{\mathbf{p}} = \sqrt{h_1^2 + h_2^2}/h_3$ and $\tan \phi_{\mathbf{p}} = h_2/h_1$ the conduction and valence band states in the sublattice representation are

$$|+, \mathbf{p}\rangle = \begin{pmatrix} \cos \frac{\theta_{\mathbf{p}}}{2} \\ \sin \frac{\theta_{\mathbf{p}}}{2} e^{i\phi_{\mathbf{p}}} \end{pmatrix}, \quad |-, \mathbf{p}\rangle = \begin{pmatrix} -\sin \frac{\theta_{\mathbf{p}}}{2} \\ \cos \frac{\theta_{\mathbf{p}}}{2} e^{i\phi_{\mathbf{p}}} \end{pmatrix}. \quad (2.11)$$

It follows that

$$\begin{aligned}
\delta n &= 4 \int_{|p| < p_c} \frac{d^2 p}{(2\pi\hbar)^2} \langle -, \mathbf{p} | \frac{\sigma_z}{2} | -, \mathbf{p} \rangle \\
&= -\frac{1}{2\pi^2\hbar^2} \int_0^{2\pi} \int_0^{p_c} \cos \theta_{\mathbf{p}} p dp d\varphi_{\mathbf{p}}, \tag{2.12}
\end{aligned}$$

where $p_c = \gamma_1/v_0$ is the high momentum cutoff of the effective model and $\varphi_{\mathbf{p}}$ is the angle of \mathbf{p} .

Let's first discuss the simplified two-band model which has only the chiral term. For general N

$$\begin{aligned}
\hat{H}_{\text{ch}}^{(N)} &= \frac{v_0^N}{(-\gamma_1)^{N-1}} \begin{pmatrix} 0 & (\pi^\dagger)^N \\ \pi^N & 0 \end{pmatrix} \\
&= \frac{(v_0 p)^N}{(-\gamma_1)^{N-1}} (\cos(N\varphi_{\mathbf{p}}) \sigma_x + \sin(N\varphi_{\mathbf{p}}) \sigma_y). \tag{2.13}
\end{aligned}$$

The electric potential in the two-band model is $\pm \frac{U_{\text{ext}}}{2} \sigma_z$. Inserting Eq. (2.13) in Eq. (2.9) and Eq. (2.12), we obtain an algebraic formula for the self-consistent Hartree potential valid for general N :

$$\begin{aligned}
\frac{U_{\text{ext}}}{\gamma_1} &= \frac{U}{\gamma_1} + \frac{4(N-1)d}{a_0} \frac{m_2}{m_e} F(N, U), \tag{2.14} \\
F(N, U) &= \frac{1}{t_c} \int_0^{t_c} \frac{dt}{\sqrt{t^N + 1}} \\
&= {}_2F_1\left(\frac{1}{N}, \frac{1}{2}, \frac{1+N}{N}, -\left(\frac{2\gamma_1}{U}\right)^2\right),
\end{aligned}$$

where $a_0 = 0.053\text{nm}$ is the Bohr radius, m_2 is the effective mass of a graphene bilayer, $t_c = (2\gamma_1/U)^{2/N}$ and ${}_2F_1$ is Gauss' hypergeometric function. In the limit of

large N , $F(N, U) \rightarrow 1$ and thus the Hartree equation reduces to

$$U \simeq U_{\text{ext}} - \frac{4(N-1)d}{a_0} \frac{m_2}{m_e} \gamma_1 \quad (2.15)$$

except at very small U . For small U and $N = 2$, the Hartree equation reads

$$\frac{U_{\text{ext}}}{U} \simeq \frac{2d}{a_0} \frac{m_2}{m_e} \ln \frac{4\gamma_1}{U}, \quad (2.16)$$

which is consistent with previous Hartree calculations in graphene bilayers[33]. In the limit of small U for $N > 2$, the Hartree equation has the asymptotic form

$$\frac{U}{2\gamma_1} \simeq \left(\frac{U_{\text{ext}}}{2\gamma_1} \right)^{\frac{N}{2}} C, \quad (2.17)$$

where the factor $C = \left[\frac{2(N-1)d}{a_0} \frac{m_2}{m_e} \left(1 - \frac{2}{2-N} + \frac{1}{2-3N} \right) \right]^{-N/2}$. The larger the value of N , the flatter the chiral bands, and the stronger the screening. For $N = 2$ the screening response is linear up to a logarithmic factor, while for larger N , superlinear screening leads to a screened potential difference which initially grows slowly with external potential following $U \propto U_{\text{ext}}^{N/2}$. The strongest possible screening reduction of the external potential corresponds to the Hartree-potential due to transfer of all the states in the energy regime $\leq 2\gamma_1$ over which the low energy model applies to one layer.

For the trilayer case we can perform a similar calculation using the full low-

energy Hamiltonian derived in Eq. (2.6). In this case we find that

$$\begin{aligned}\frac{U_{\text{ext}}}{\gamma_1} &= \frac{U}{\gamma_1} + \frac{8d}{a_0} \frac{m_2}{m_e} G(U), \\ G(U) &= \frac{2}{\pi} \int_0^1 dt \frac{h_{\text{gap}} K\left(\frac{4\sqrt{2}h_{\text{ch}}h_{\text{tr}}}{(h_{\text{ch}}+\sqrt{2}h_{\text{tr}})^2+h_{\text{gap}}^2}\right)}{\sqrt{(h_{\text{ch}}+\sqrt{2}h_{\text{tr}})^2+h_{\text{gap}}^2}},\end{aligned}\tag{2.18}$$

where $h_{\text{ch}} = t^{\frac{3}{2}}$, $h_{\text{tr}} = |\frac{\gamma_2}{2\gamma_1} - \frac{2v_3}{v_0}t|$, $h_{\text{gap}} = \frac{U}{2\gamma_1}(1-t)$, $t = (\frac{v_0 p}{\gamma_1})^2$, and $K(x)$ is the complete elliptic integral of the first kind. Fig. 2.10 compares the screening properties of the full low-energy effective model for trilayers to the chiral model results for $N = 2, 3, 4, 5$. For $U_{\text{ext}} < \gamma_1/2$, the energy regime over which the low-energy effective model applies, we see that screening increases systematically with N because of smaller gaps between conduction and valence band orbitals which make the occupied valence band orbitals more polarizable. The comparison between the simplified chiral model and the low-energy effective model for $N = 3$ demonstrates that remote hopping processes suppress screening because they tend to increase the gap between conduction and valence bands at momenta near the Brillouin-zone corner.

In concluding this section we caution that occupied σ orbitals, neglected in the low-energy effective model and π -band tight-binding models, will contribute slightly to polarization by an external electric field and therefore to screening. Furthermore exchange potentials will also be altered by an external electric field and influence the screening. Since exchange interactions are attractive, they always work against screening and will make a negative contribution to the screening ratio we have discussed in multilayers. Because the low energy eigenstates in multilayers are coherent superpositions of states localized in different layers, our DFT calculations

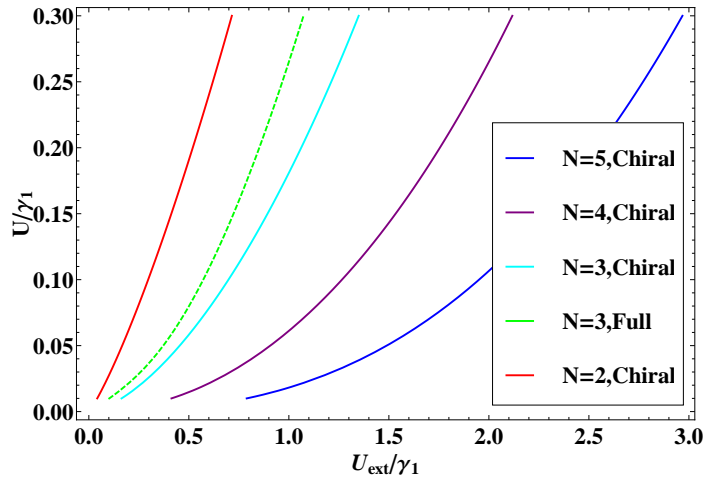


Figure 2.10: U v.s. U_{ext} plot describes the screening effect in different chiral- N systems. The Chiral model results refer to the Hamiltonian in Eq. (2.13) while the full model results refer to the Hamiltonian in Eq. (2.6).

which employ a local exchange approximation, might also yield inaccurate results for the screening ratio. In fact simple measurements of the screening properties might provide a valuable window on many-body physics in ABC-stacked graphene multilayers which lies outside the scope of commonly employed approximations.

2.4 Discussion

We have derived an effective model for the low-energy conduction and valence bands of an ABC-stacked graphene multilayer. The low-energy model can be viewed as a momentum-dependent pseudospin Hamiltonian, with the pseudospin constructed from the low energy sites on the top and bottom layers. The simplified version of this model starts from a π -band tight-binding model with only nearest neighbor hopping and yields a pseudospin magnetic field whose magnitude varies as momentum p^N in an N -layer stack and whose direction is $N\phi_{\mathbf{p}}$ where $\phi_{\mathbf{p}}$ is the

momentum orientation. The likely importance of electron-electron interactions in multilayers can be judged by comparing the characteristic band and interaction energies in a system with carrier density n and Fermi wavevector $p_F \propto \sqrt{n}$. The characteristic Coulomb interaction energy per-particle in all cases goes like $e^2 n^{1/2}$, while the band energy goes like $n^{N/2}$. For low-carrier densities the band energy scale is always smaller. In the case of trilayer ABC graphene, the interaction energy scale is larger than the band energy scale for carrier density $n < 10^{12} \text{cm}^{-2}$.

Although interactions are clearly important and can potentially introduce new physics, the chiral band model is not valid at low-densities because of the influence of remote hopping processes which we have estimated in this article by carefully fitting a low-energy effective model to DFT bands. The Hamiltonian in Eq. (2.6) combined with the parameters in Table I should be used to describe graphene trilayers with low carrier densities. In a realistic system the Fermi surface of a ABC trilayer with a low carrier density consists of three electron pockets centered away from the K point. As the carrier density grows these pockets convert via a sequence of two closely spaced Lifshitz transitions into a single K-centered pocket. The carrier density at the Lifshitz transition is $\sim 10^{11} \text{cm}^{-2}$, which translates to a Coulomb interaction scale of $\sim 45 \text{meV}$, compared to a Fermi energy of $\sim 7 \text{meV}$.

The Berry phase associated with the momentum-dependence of the pseudospin orientation field, π for a full rotation in single-layers and 2π in the bilayer chiral model for example, is known[57–63] to have an important influence on quantum corrections to transport. Because of their very different Berry phases time-reversed paths are expected to interfere destructively for N -odd systems while constructively for N -even system, leading to weak anti-localization for odd N and weak localization for even N . This general tendency will however be altered by trigonal and other corrections to the low-energy effective Hamiltonian, like those

we have derived for trilayers. The influence of these band features on quantum corrections to transport can be evaluated starting from the results obtained here.

Another important consequence of Berry phases in the chiral model is the unconventional Landau level structure it yields[4, 5, 29–31]. In the chiral model for ABC trilayers there is a three-fold degeneracy at the Dirac point, in addition to the usual spin and valley degeneracies. This grouping of Landau level leads to the expectation that quantum Hall studies in trilayers will reveal plateaus that jump from one at $-6e^2/h$ to one at $6e^2/h$. Electron-electron interactions acting alone are expected to lift these degeneracies and give rise to quantum Hall ferromagnetism[12, 64, 65]. These interaction effects will act in concert with small corrections to the Landau level structures due to the remote hopping terms that have been quantified in this chapter.

Although we have discussed the case of ABC stacked trilayers, we expect qualitatively similar results for ABC stacking sequences of general thickness N . At low energies the band structure will consist of a conduction and a valence band with p^N dispersion and a gap in the presence of an external electric field across the film. In the presence of a magnetic field N Landau levels are pinned to the neutral system Fermi level for each spin and valley. At the lowest energies, within around 10meV of the neutral system Fermi level, constant energy surfaces will be strongly influenced by remote hopping processes which will also split the Dirac point Landau levels. The remote hopping terms give rise to saddle-points in the band structure at which the density-of-states will diverge. Broken symmetry electronic states are mostly likely to occur when the Fermi level is coincident with these saddle points. The energy range over which the low-energy effective model applies will, however, decrease with film thickness. We expect both disorder and interaction effects to be strong within this family of low-dimensional electron systems, which should be ac-

cessible to experimental study in samples for which disorder is weak on the energy scale over which the low-energy effective model applies.

In summary, we have derived an effective model for trilayers, extracted the hopping parameters for ABC-stacked multilayers, from DFT and studied the trilayer Fermi surfaces. Furthermore, we have explored the screening effect in trilayers and then explained and compared with other C2DES cases by a tight-binding model self-consistent Hartree method. Lastly, we have argued the importance of Berry phases and interactions in C2DES.

Chapter 3

Electron-Electron Interactions in Bilayer Graphene

In a mean-field-theory treatment the ground state of a graphene bilayer spontaneously breaks inversion symmetry for arbitrarily weak electron-electron interactions when trigonal warping terms in the band structure are ignored. This chapter first details a perturbative renormalization group calculation which assesses the robustness of this instability, comparing with the closely related case of the charge-density-wave instability incorrectly predicted by mean-field theory in a one-dimensional electron gas. Two dimensional bilayer graphene systems behave in many ways as if they were one dimensional, although the interactions become marginally relevant in the one loop level, unlike the case of Luttinger liquids. It turns out that the mean-field instability is not suppressed by quantum fluctuations but that, because of trigonal warping, it may occur only in high quality suspended bilayers. We then explain the influences of spin and pseudospin degrees of freedom, trigonal warping and external interlayer potential difference on the RG flows of the

interaction parameters. Based on a layer pseudospin susceptibility calculation, we further conclude that the ground states of bilayer graphene and its thicker chiral cousins spontaneously break their layer inversion symmetry with a spontaneous gap opening at Dirac points via the weak repulsive interaction instability. Lastly, we details various broken symmetry states in bilayer graphene and compare them with the state observed in recent experiments. This analysis leads to the conclusion that the gaps[10, 15, 46] observed[13, 17, 18] in the quasiparticle spectrum of bilayer graphene likely reflect the formation of spontaneous quantum Hall states[9] in which inversion symmetry is broken[10] in opposite senses for different spins or valleys.

3.1 Introduction

Electrons most often organize into Fermi-liquid states in which interactions play an inessential role. A well known exception is the case of one-dimensional (1D) electron systems (1DES). In 1D, the electron Fermi-surface consists of points, and divergences associated with low-energy particle-hole excitations abound when electron-electron interactions are described perturbatively. In higher space dimensions, the corresponding divergences occur only when Fermi lines or surfaces satisfy idealized nesting conditions. In this article we discuss electron-electron interactions in 2D graphene bilayer systems which behave in many ways as if they were one-dimensional, because they have Fermi points instead of Fermi lines and because their particle-hole energies have a quadratic dispersion which compensates for the difference between 1D and 2D phase space.

Recent progress in isolation of nearly perfect single and multilayer graphene sheets[2, 3, 26, 27] has opened up a new topic in two-dimensional electron sys-

tems (2DES) physics. There is to date little unambiguous experimental evidence that electron-electron interactions play an essential role in the graphene family of 2DES's. However, as pointed out by Min *et al.*[15] graphene bilayers near neutrality should be particularly susceptible to interaction effects because of their peculiar massive-chiral[4] band Hamiltonian, which has an energy-splitting between valence and conduction bands that vanishes at $\mathbf{q} = 0$ and grows quadratically with $q = |\mathbf{q}|$:

$$\mathcal{H}_B = - \sum_{\mathbf{q}\sigma'\sigma} \frac{\hbar^2 q^2}{2m^*} c_{\mathbf{q}\sigma'}^\dagger [\cos(J\phi_{\mathbf{q}})\tau_{\sigma'\sigma}^x + \sin(J\phi_{\mathbf{q}})\tau_{\sigma'\sigma}^y] c_{\mathbf{q}\sigma}. \quad (3.1)$$

In Eq. (3.1) the τ^i 's are Pauli matrices and the Greek labels refer to the two bilayer graphene sublattice sites, one in each layer, which do not have a neighbor in the opposite graphene layer. (See Fig. 3.1.) The other two sublattice site energies are repelled from the Fermi level by interlayer hopping and irrelevant at low energies. It is frequently useful to view quantum two-level layer degree of freedom as a pseudospin. The $J = 2$ pseudospin chirality of bilayer graphene contrasts with the $J = 1$ chirality[26, 28] of single-layer graphene and is a consequence of the two-step process in which electrons hop between low-energy sites via the high-energy sites. The massive-chiral band-structure model applies at energies smaller than the interlayer hopping scale[3] $\gamma_1 \sim 0.3$ eV but larger than the trigonal-warping scale[3] $\gamma_3(\gamma_1/\gamma_0)^2 \sim 0.003$ eV below which direct hopping between low-energy sites plays an essential role. The body of this section concerns the role of interactions in the massive-chiral model; we return at the end to explain the important role played by trigonal warping.

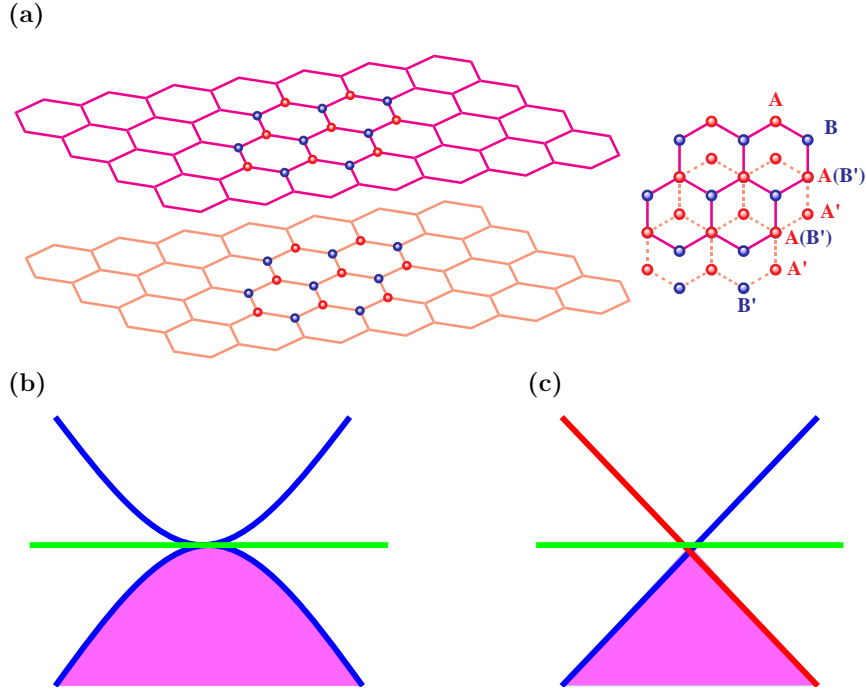


Figure 3.1: **a**, The massive chiral fermion model describes the low-energy sites in a AB-stacked graphene bilayer, those atom sites (top layer B sites and bottom layer A' sites) which do not have a neighbor in the opposite layer. **b**, The conduction and valence bands of a graphene bilayer touch at the Brillouin-zone corner wavevectors, taken as zero-momentum in continuum model theories, and separate quadratically with increasing wavevector. **c**, In a 1DES left and right going electrons cross the Fermi energy at a single point; The momentum of right-going (left-going) electrons is plotted relative to q_F ($-q_F$) where q_F is the Fermi wavevector.

3.2 Similarities and differences between 1DES and bilayer graphene

Similarities and differences between graphene bilayers and 1DES are most easily explained by temporarily neglecting the spin, and in the case of graphene also the additional valley degree of freedom. As illustrated in Fig. 3.1 in both cases the Fermi sea is point-like and there is a gap between occupied and empty free-particle

states which grows with wavevector, linearly in the 1DES case. These circumstances are known to support a mean-field broken symmetry state in which phase coherence is established between conduction and valence band states for arbitrarily weak repulsive interactions. In the case of a 1DES, the broken symmetry state corresponds physically to a charge density-wave (CDW) state, while in the case of bilayer graphene[15] it corresponds to state in which charge is spontaneously transferred between layers. This mean-field theory prediction is famously incorrect in the 1DES case, and the origin of the failure can be elegantly identified[66, 67] using a perturbative renormalization group (PRG) approach. We show below that when applied to bilayer graphene, the same considerations lead to a different conclusion.

The reliability of the mean-field theory prediction[15] of a weak-interaction instability in bilayer graphene can be systematically assessed using PRG[67]. We outline the main steps in the application of PRG to bilayer graphene, pointing out essential differences compared to the 1DES case. We assume short-range interactions¹ between electrons in the same (S) and different (D) layers.

The PRG analysis centers on the four point scattering function defined in terms of Feynman diagrams in Fig. 3.2. Since the Pauli exclusion principle implies that (in the spinless valleyless case) no pair of electrons can share the same 2D position unless they are in opposite layers, intralayer interactions cannot influence the particles; there is therefore only one type of interaction generated by the RG flow, interactions between electrons in opposite layers with the renormalized coupling parameter Γ_D . The direct and exchange first order processes in Fig. 3.2 have the values V_D (bare coupling parameter) and 0 respectively.

The PRG analysis determines how V_D is renormalized in a RG procedure

¹We replace the bare Coulomb interactions by short-range momentum-independent interactions[67] by evaluating them at typical momentum transfers at the model's high-energy limit. We believe that this approximation is not serious because of screening.

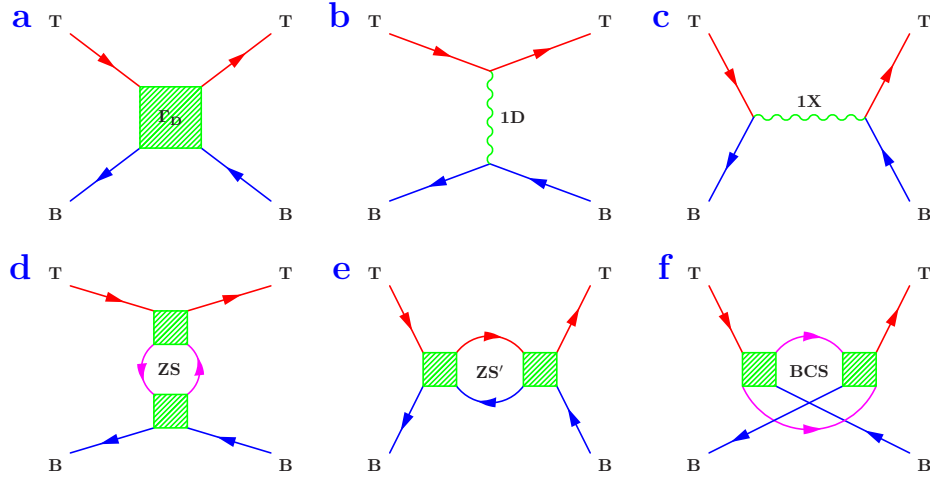


Figure 3.2: **a**, The renormalized interaction Γ_D . **b**, **c**, The direct and exchange bare interactions. **d**, **e**, **f**, They are the one-loop diagrams labelled ZS, ZS' and BCS, respectively. The external and internal Green's function labels refer to layer in the case of graphene and to chirality in 1DES' case.

in which high energy degrees of freedom are integrated out and the fermion fields of the low energy degrees of freedom are rescaled to leave the free-particle action invariant. The effective interaction Γ_D is altered by coupling between low and high energy degrees of freedom. At one loop level this interaction is described[67] by the three higher order diagrams labeled ZS, ZS', and BCS in Fig. 3.2. The internal loops in these diagrams are summed over the high-energy labels. In the case of 1DES the ZS loop vanishes and the ZS' and BCS diagrams cancel, implying that the interaction strengths do not flow to large values and that neither the CDW repulsive interaction nor the BCS attractive interaction instabilities predicted by mean-field theory survive the quantum fluctuations they neglect. The key message of this section is summarized by two observations about the properties of these one-loop diagrams in the bilayer graphene case: (i) the particle-particle (BCS) and particle-hole (ZS, ZS') loops have the same logarithmic divergences as in the 1DES

case in spite of the larger space dimension and (ii) the ZS loop, which vanishes in the 1DES case, is finite in the bilayer graphene case and the BCS loop vanishes instead. Both of these changes are due to a layer pseudospin triplet contribution to the single-particle Green's function as we explain in the next subsections. The net result is that interactions flow to strong coupling even more strongly than in the mean-field approximation. The following paragraphs outline key steps in the calculations which support these conclusions.

3.3 Perturbative renormalization group analysis in bilayer graphene

3.3.1 Green's functions and frequency sums

Starting from the low-energy massive chiral band Hamiltonian 3.1, an elementary calculation shows that the single-particle Matsubara Green's function corresponding to the Hamiltonian in Eq. (3.1) is

$$\mathcal{G}(\mathbf{q}, i\omega_n) = \begin{pmatrix} \mathcal{G}_s(\mathbf{q}, i\omega_n) & -\mathcal{G}_t(\mathbf{q}, i\omega_n)e^{-iJ\phi_q} \\ -\mathcal{G}_t(\mathbf{q}, i\omega_n)e^{iJ\phi_q} & \mathcal{G}_s(\mathbf{q}, i\omega_n) \end{pmatrix} \quad (3.2)$$

where $\hbar\omega_q = \xi_q = \hbar q^2/2m^*$ and

$$\mathcal{G}_{s,t}(\mathbf{q}, i\omega_n) \equiv \frac{1}{2} \left(\frac{1}{i\omega_n - \omega_q} \pm \frac{1}{i\omega_n + \omega_q} \right). \quad (3.3)$$

The pseudospin-singlet component of the Green's function \mathcal{G}_s , which is diagonal in layer index, changes sign under frequency inversion whereas the triplet component \mathcal{G}_t , which is off-diagonal, is invariant.

The loop diagrams are evaluated by summing the product of two Green's functions (corresponding to the two arms of the Feynman diagram loops) over momentum and frequency. The frequency sums are standard and yield ($\beta = (k_B T)^{-1}$)

$$\begin{aligned} \frac{1}{\beta \hbar^2} \sum_{\omega_n} \mathcal{G}_{s,t}^2(i\omega_n) &= \mp \frac{\tanh(\beta \xi_q/2)}{4\xi_q} \xrightarrow{T \rightarrow 0} \mp \frac{1}{4\xi_q} \\ \frac{1}{\beta \hbar^2} \sum_{\omega_n} \mathcal{G}_s(i\omega_n) \mathcal{G}_t(i\omega_n) &\xrightarrow{T \rightarrow 0} 0 \end{aligned} \quad (3.4)$$

where \mathbf{q} is the momentum label shared by the Green's functions. Note that the singlet-triplet product sum vanishes in the low-temperature limit in which we are interested. Each loop diagram is multiplied by appropriate interaction constants (discussed below) and then integrated over high energy momentum labels up to the massive chiral fermion model's ultraviolet cutoff Λ :

$$\int_{\Lambda/s < q < \Lambda} \frac{d^2 \mathbf{q}}{(2\pi)^2} \frac{\tanh(\beta \xi_q/2)}{4\xi_q} \xrightarrow{T \rightarrow 0} \frac{1}{2} v_0 \ln(s) \quad (3.5)$$

where $v_0 = m^*/2\pi\hbar^2$ is the graphene bilayer density-of-states. Because $\omega_q \propto q^2$, this integral grows logarithmically when the high-energy cut-off is scaled down by a factor of s in the RG transformation, exactly like the familiar 1DES case. This rather surprising property of bilayer graphene is directly related to its unusual band structure with Fermi points rather than Fermi lines and quadratic rather than linear dispersion.

The key differences between bilayer graphene and the 1DES appear upon identifying the coupling factors which are attached to the loop diagrams. The external legs in the scattering function Feynman diagrams (Fig. 3.2) are labeled by layer index ($T =$ top layer and $B =$ bottom layer) in bilayer graphene. The corresponding labels for the 1DES are chirality ($R =$ right-going and $L =$ left going); we call these

interaction labels when we refer to the two cases generically. Since only opposite layer interactions are relevant, all scattering functions have two incoming particles with opposite layer labels and two outgoing particles with opposite layer labels.

3.3.2 PRG analysis for a single spin-valley

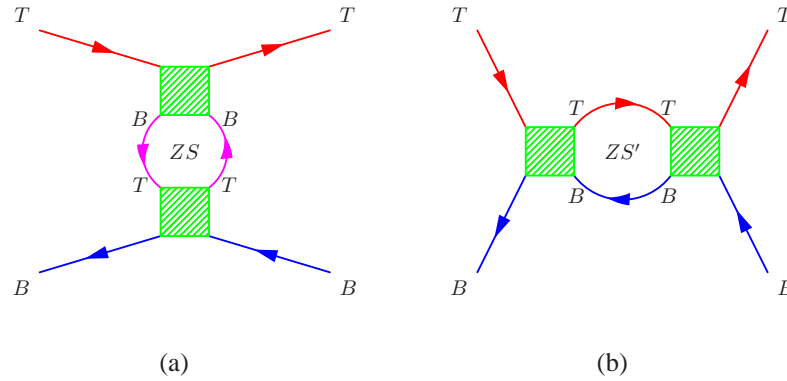


Figure 3.3: **(a)** ZS, **(b)** ZS' loop corrections in the one-loop PRG calculation.

The character of the marginally relevant interactions in bilayer graphene is most easily explained by PRG analysis for a single spin-valley, as we will see in this subsection. As shown in Fig. 3.3(a), at the upper vertex of ZS diagram the incoming and the outgoing T particles induce a B particle-hole pair in the loop while the incoming and outgoing B particles at the lower vertex induce a T particle-hole pair. The corresponding labels in the 1DES case are L, R for left and right chirality. The ZS contribution is absent in the 1DES case[66, 67] because propagation is always diagonal in interaction labels. However, this correction survives for GBS because the single-particle Green's function has a triplet contribution [see Eq. (3.4)] which

is off-diagonal in layer index. Here we find

$$\begin{aligned}\Gamma_{\text{D}}^{\text{ZS}} &= \frac{\Gamma_{\text{D}}^2}{\beta\hbar^2} \int \frac{d^2\mathbf{q}}{(2\pi)^2} \sum_{\omega_n} \mathcal{G}_t^2(\mathbf{q}, i\omega_n) \\ &= \Gamma_{\text{D}}^2 \int \frac{d^2\mathbf{q}}{(2\pi)^2} \frac{\tanh(\beta\xi_{\mathbf{q}}/2)}{4\xi_{\mathbf{q}}} = \frac{1}{2} \Gamma_{\text{D}}^2 v_0 \ln(s),\end{aligned}\quad (3.6)$$

where $v_0 = m^*/2\pi\hbar^2$ is the graphene bilayer density-of-states (per spin and valley) and the integral is carried out in the momentum shell $\Lambda/s < q < \Lambda$.

The ZS' loop shown in Fig. 3.3(b) corresponds to repeated interaction between a T particle and a B hole. This is the channel responsible for the 1DES mean-field CDW instability [67] in which coherence is established between R and L particles[66]. In both 1DES and GBS cases it has the effect of enhancing repulsive interactions. Its evaluations for the two cases correspond quite closely, because this loop diagram involves only particle-propagation that is diagonal in interaction labels, namely, singlet contribution. We find

$$\begin{aligned}\Gamma_{\text{D}}^{\text{ZS}'} &= -\frac{\Gamma_{\text{D}}^2}{\beta\hbar^2} \int \frac{d^2\mathbf{q}}{(2\pi)^2} \sum_{\omega_n} \mathcal{G}_s^2(\mathbf{q}, i\omega_n) \\ &= \Gamma_{\text{D}}^2 \int \frac{d^2\mathbf{q}}{(2\pi)^2} \frac{\tanh(\beta\xi_{\mathbf{q}}/2)}{4\xi_{\mathbf{q}}} = \frac{1}{2} \Gamma_{\text{D}}^2 v_0 \ln(s).\end{aligned}\quad (3.7)$$

The BCS channel corresponds to repeated interaction between the two incoming particles. In the 1DES case the contribution from this loop (see Fig. 3.4) cancels the ZS' contribution[67], leading to marginal interactions and Luttinger liq-

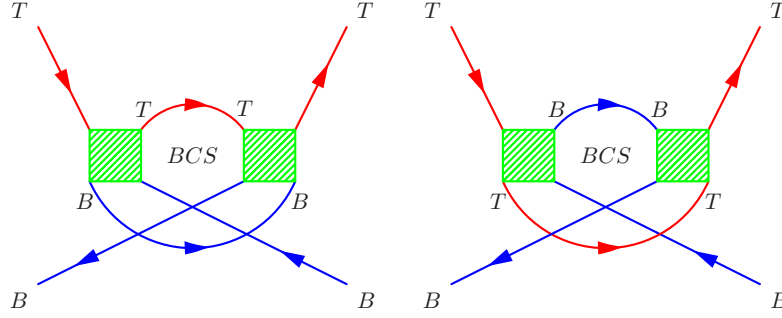


Figure 3.4: BCS(particle-particle) loop correction for singlet propagation in the one-loop PRG calculation.

uid behavior. This same kind of BCS correction for graphene bilayer reads

$$\begin{aligned}
 \Gamma_D^{\text{BCS}_1} &= - \frac{1}{2} \frac{\Gamma_D^2}{\beta \hbar^2} \int \frac{d^2 \mathbf{q}}{(2\pi)^2} \sum_{\omega_n} \mathcal{G}_s(\mathbf{q}, i\omega_n) \mathcal{G}_s(-\mathbf{q}, -i\omega_n) \\
 &\quad - \frac{1}{2} \frac{(-\Gamma_D)^2}{\beta \hbar^2} \int \frac{d^2 \mathbf{q}}{(2\pi)^2} \sum_{\omega_n} \mathcal{G}_s(\mathbf{q}, i\omega_n) \mathcal{G}_s(-\mathbf{q}, -i\omega_n) \\
 &= - \frac{1}{2} \Gamma_D^2 v_0 \ln(s). \tag{3.8}
 \end{aligned}$$

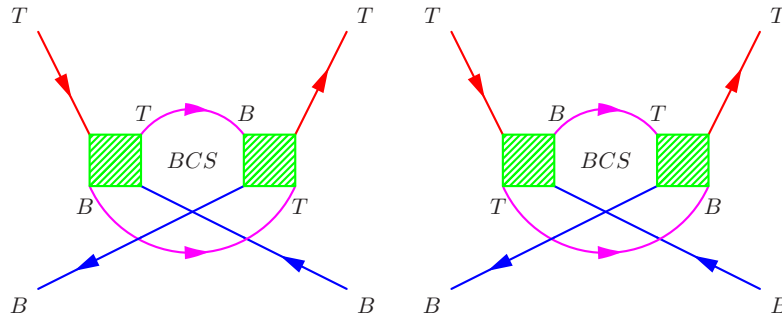


Figure 3.5: BCS(particle-particle) loop correction for triplet propagation in the one-loop PRG calculation.

In the graphene bilayer case, however, there is an additional contribution (see Fig. 3.5) to the BCS loop contribution in which the incoming T and B particles both change layer labels before the second interaction. This contribution is possible because of the triplet layer pseudospin propagation and, in light of Eq. (3.4), gives a BCS contribution of opposite sign to the normal contribution:

$$\begin{aligned}
\Gamma_D^{\text{BCS}_2} &= -\frac{1}{2} \frac{\Gamma_D(-\Gamma_D)}{\beta\hbar^2} \int \frac{d^2\mathbf{q}}{(2\pi)^2} \sum_{\omega_n} \mathcal{G}_t(\mathbf{q}, i\omega_n) \mathcal{G}_t(-\mathbf{q}, -i\omega_n) \\
&\quad -\frac{1}{2} \frac{(-\Gamma_D)\Gamma_D}{\beta\hbar^2} \int \frac{d^2\mathbf{q}}{(2\pi)^2} \sum_{\omega_n} \mathcal{G}_t(\mathbf{q}, i\omega_n) \mathcal{G}_t(-\mathbf{q}, -i\omega_n) \\
&= \frac{1}{2} \Gamma_D^2 v_0 \ln(s). \tag{3.9}
\end{aligned}$$

It follows that the BCS loop contribution is absent in the graphene bilayer case because

$$\Gamma_D^{\text{BCS}} = \Gamma_D^{\text{BCS}_1} + \Gamma_D^{\text{BCS}_2} = 0. \tag{3.10}$$

Therefore, at one-loop level, the renormalization of interlayer interaction is

$$\Gamma_D^{\text{one-loop}} = \Gamma_D^{\text{ZS}} + \Gamma_D^{\text{ZS}'} + \Gamma_D^{\text{BCS}} = \Gamma_D^2 v_0 \ln(s). \tag{3.11}$$

These results and comparison with 1DES are summarized in Table 3.1 and imply the following RG flow equation for GBS:

$$\frac{d\Gamma_D}{v_0 d\ln(s)} = \Gamma_D^2. \tag{3.12}$$

Combined with the bare interlayer interaction V_D and integrating the flow equation

we obtain that

$$\Gamma_D = \frac{V_D}{1 - V_D v_0 \ln(s)} \quad (3.13)$$

which diverges if $V_D v_0 \geq 1/\ln(s)$. This equation serves as an instability criterion similar with Stoner criterion in ferromagnetism.

Table 3.1: Summary of contrasting the contributions (in units of the related density-of-states) of the three one-loop diagrams in 1DEG and graphene bilayer cases

diagrams	1DEG	Graphene Bilayer
<i>ZS</i>	0	$\frac{1}{2} \Gamma_D^2 \ln(s)$
<i>ZS'</i>	$u^2 \ln(s)$	$\frac{1}{2} \Gamma_D^2 \ln(s)$
<i>BCS</i>	$-u^2 \ln(s)$	0
Mean Field	$u^2 \ln(s)$	$\frac{1}{2} \Gamma_D^2 \ln(s)$
Quantum Fluctuations	$-u^2 \ln(s)$	$\frac{1}{2} \Gamma_D^2 \ln(s)$
Full One-Loop	0	$\Gamma_D^2 \ln(s)$

For the Feynman diagrams drawing conventions we have chosen, the interaction correction to the layer pseudospin response function χ_{zz} , which diverges at the pseudospin ferromagnet phase boundary, is obtained by closing the scattering function with a τ_z vertex at top and bottom. The τ_z operator measures the charge difference between *T* and *B* layers. Because it is an effective single-particle theory, fermion mean-field theory[15] corresponds to response function diagrams with at most a single particle-hole pair. It follows that mean-field theory is equivalent to a single-loop PRG calculation in which the BCS and *ZS'* channels, namely, the quantum fluctuations are neglected and only the *ZS* channel is retained. In mean-field theory[15] the ideal graphene bilayer has an instability to a state in which charge is

spontaneously transferred between the layers which is signalled by the divergence of χ_{zz} . The PRG analysis demonstrates that the mean-field theory instability is enhanced by reinforcing ZS' channel contribution.

Therefore, the net result is that interactions flow to strong coupling even more strongly than in the mean-field approximation. Taking guidance from the mean-field theory[15], the strong coupling state at each spin-valley is likely a pseudospin ferromagnet which has an energy gap and spontaneous charge transfer between layers, spontaneously breaking the inversion symmetry. The following subsections outline how spin and valley degrees of freedom influence the RG flows and which pseudospin channel has the most divergent susceptibility which support these conclusions.

3.3.3 Spins pseudospins and distinct interaction parameters

In the low-energy continuum model of bilayer graphene electrons carry spin, and both layer and valley pseudospin labels. In a scattering event, both the two incoming and two outgoing particles can therefore have one of eight labels and the general scattering function therefore has 8^4 possible low-energy long-wavelength values. The number of distinct coupling constants in the RG flow equations is much smaller, however, because many values are zero and others are related to each other by symmetry. One simplification is that interactions conserve spin, and both layer and valley pseudospin, at each vertex. Interactions are however dependent on whether the interacting particles are in the same (*S*) or in different (*D*) layers. The internal loops in the perturbative RG calculation contain two fermion propagator (Green's function) lines. These propagators conserve both spin and valley pseudospin, but as we have seen above, not the layer pseudospin. It is clear then that the incoming and

outgoing total spin must be preserved for real spin and for the valley pseudospin, but the layer pseudospin case requires a more elaborate consideration. From Eq. (3.2) we see that a phase factor $e^{\pm 2i\phi_q}$ is gained when the propagator transfers electrons between layer index with the $+$ for top to bottom evolution and the $-$ for bottom to top. Unless these transfers enter an equal number of times in each direction, the integrand in a Feynman diagram will contain a net phase factor related to chirality and vanish under momentum integration. The total layer pseudospin is therefore also conserved in collisions.

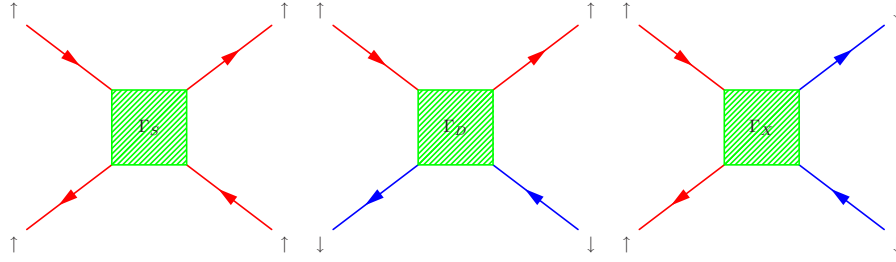


Figure 3.6: Electron-electron scattering processes for a system with one pseudospin-1/2 degree of freedom.

In identifying distinct coupling constants, we start with the simplest case in which the valley and spin labels are absent. There are then three possibilities, as illustrated in Fig. 3.6. When the two incoming pseudospins are parallel (Γ_S in Fig. 3.6), the outgoing pseudospins must also be parallel. Because of Fermi statistics interchanging the outgoing lines in Γ_S changes the diagrams's sign. Since the diagram is invariant under this operation, it must vanish. The second possibility is opposite incoming pseudospins, which requires opposite outgoing pseudospins in one of the two configurations labelled by Γ_D and Γ_X in Fig. 3.6. In this case Fermi statistics implies that $\Gamma_D = -\Gamma_X$. It follows that the only distinct interaction

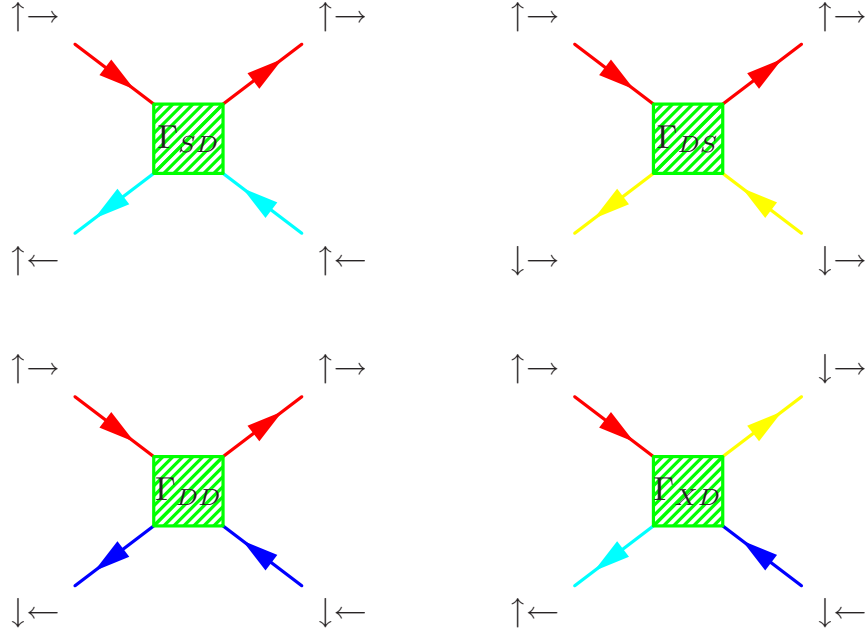


Figure 3.7: Distinct interaction channels for systems with two pseudospin-1/2 degrees of freedom. In this figure the first spin is denoted by $|\uparrow\rangle$ or $|\downarrow\rangle$ while the second by $|\rightarrow\rangle$ or $|\leftarrow\rangle$. The one-dimensional electron gas system can be viewed as being in this class if the chirality index is regarded as a pseudospin.

parameter is Γ_D .

If more than one pseudospin is present, we have to recognize more separate interacting processes. For example, for systems with two relevant pseudospins, the interaction parameters can be labeled in the same way as in Fig. 3.6 but by doublets which account for the different pseudospins separately. For instance, two pseudospin interactions might include Γ_{SD} , Γ_{DS} , Γ_{DD} and Γ_{XD} (see Fig. 3.7). Again Γ_{SS} is absent due to Pauli exclusion principle. If the labels represent layer and spin respectively, interpreting their physical meaning, $\Gamma_{S(D)D(S)}$ denotes the interaction between the particles within the same (different) layer(s) carrying different (same) spin flavor(s) respectively; Γ_{XD} corresponds to the layer-flipping interacting process between particles having different spin flavors. In models for which prop-

agators and interactions preserve all pseudospin labels, we would have $\Gamma_{XD} = 0$ since all pseudospin flavors are preserved along each fermion line. For graphene bilayers, however, we must keep $\Gamma_{XD} \neq 0$ because the layer pseudospin has triplet propagation. Following this line of argument, considering Pauli exclusion principle and the fermionic antisymmetry between outgoing particles, we conclude that in graphene bilayers, with its three different pseudospins, there are ten distinct non-zero interaction parameters: Γ_{SSD} , Γ_{SDS} , Γ_{SDD} , Γ_{DSS} , Γ_{DSD} , Γ_{DDS} , Γ_{DDD} , Γ_{XSD} , Γ_{XDS} and Γ_{XDD} , where the first label refers to layer pseudospin, and the following labels to real spin and valley.

3.3.4 RG flow equations for distinct interaction parameters

The one-loop flow equations are derived in the same way as in the spinless valleyless case, except for the necessity of keeping track of the many-possible configurations of the end labels on the loop propagators. We summarize the RG flow equations in Eq.(3.14).

$$\begin{aligned}
\frac{d\Gamma_{SSD}}{v_0 d\ln(s)} &= -\frac{1}{2}\Gamma_{SSD}^2 - \Gamma_{DSS}(\Gamma_{DSD} - \Gamma_{SSD}) \\
&\quad - (\Gamma_{DDS} - \Gamma_{SDS})(\Gamma_{DDD} - \Gamma_{SDD}) + \frac{1}{2}(\Gamma_{XSD} - \Gamma_{SSD})^2 \\
\frac{d\Gamma_{SDS}}{v_0 d\ln(s)} &= -\frac{1}{2}\Gamma_{SDS}^2 - \Gamma_{DSS}(\Gamma_{DDS} - \Gamma_{SDS}) \\
&\quad - (\Gamma_{DSD} - \Gamma_{SSD})(\Gamma_{DDD} - \Gamma_{SDD}) + \frac{1}{2}(\Gamma_{XDS} - \Gamma_{SDS})^2 \\
\frac{d\Gamma_{SDD}}{v_0 d\ln(s)} &= -\frac{1}{2}\Gamma_{SDD}^2 - \Gamma_{DSS}(\Gamma_{DDD} - \Gamma_{SDD}) \\
&\quad - (\Gamma_{DSD} - \Gamma_{SSD})(\Gamma_{DDS} - \Gamma_{SDS}) + \frac{1}{2}(\Gamma_{XDD} - \Gamma_{SDD})^2
\end{aligned}$$

$$\begin{aligned}
\frac{d\Gamma_{\text{DSS}}}{v_0 d\ln(s)} &= \Gamma_{\text{DSS}}^2 + \frac{1}{2}(\Gamma_{\text{DSD}} - \Gamma_{\text{SSD}})^2 + \frac{1}{2}(\Gamma_{\text{DDS}} - \Gamma_{\text{SDS}})^2 \\
&\quad + \frac{1}{2}(\Gamma_{\text{DDD}} - \Gamma_{\text{SDD}})^2 + \frac{1}{2}\Gamma_{\text{XSD}}^2 + \frac{1}{2}\Gamma_{\text{XDS}}^2 + \frac{1}{2}\Gamma_{\text{XDD}}^2 \\
\frac{d\Gamma_{\text{DSD}}}{v_0 d\ln(s)} &= \frac{1}{2}\Gamma_{\text{DSD}}^2 + \Gamma_{\text{DSS}}(\Gamma_{\text{DSD}} - \Gamma_{\text{SSD}}) \\
&\quad + (\Gamma_{\text{DDD}} - \Gamma_{\text{SDD}})(\Gamma_{\text{DDS}} - \Gamma_{\text{SDS}}) - \frac{1}{2}(\Gamma_{\text{DSD}} + \Gamma_{\text{XSD}})^2 \\
\frac{d\Gamma_{\text{DDS}}}{v_0 d\ln(s)} &= \frac{1}{2}\Gamma_{\text{DDS}}^2 + \Gamma_{\text{DSS}}(\Gamma_{\text{DDS}} - \Gamma_{\text{SDS}}) \\
&\quad + (\Gamma_{\text{DDD}} - \Gamma_{\text{SDD}})(\Gamma_{\text{DSD}} - \Gamma_{\text{SSD}}) - \frac{1}{2}(\Gamma_{\text{DDS}} + \Gamma_{\text{XDS}})^2 \\
\frac{d\Gamma_{\text{DDD}}}{v_0 d\ln(s)} &= \frac{1}{2}\Gamma_{\text{DDD}}^2 + \Gamma_{\text{DSS}}(\Gamma_{\text{DDD}} - \Gamma_{\text{SDD}}) \\
&\quad + (\Gamma_{\text{DDS}} - \Gamma_{\text{SDS}})(\Gamma_{\text{DSD}} - \Gamma_{\text{SSD}}) - \frac{1}{2}(\Gamma_{\text{DDD}} + \Gamma_{\text{XDD}})^2 \\
\frac{d\Gamma_{\text{XSD}}}{v_0 d\ln(s)} &= \Gamma_{\text{DSS}}\Gamma_{\text{XSD}} - \Gamma_{\text{XDS}}\Gamma_{\text{XDD}} \\
&\quad - \frac{1}{2}(\Gamma_{\text{XSD}} - \Gamma_{\text{SSD}})^2 - \frac{1}{2}(\Gamma_{\text{XSD}} + \Gamma_{\text{DSD}})^2 \\
\frac{d\Gamma_{\text{XDS}}}{v_0 d\ln(s)} &= \Gamma_{\text{DSS}}\Gamma_{\text{XDS}} - \Gamma_{\text{XSD}}\Gamma_{\text{XDD}} \\
&\quad - \frac{1}{2}(\Gamma_{\text{XDS}} - \Gamma_{\text{SDS}})^2 - \frac{1}{2}(\Gamma_{\text{XDS}} + \Gamma_{\text{DDS}})^2 \\
\frac{d\Gamma_{\text{XDD}}}{v_0 d\ln(s)} &= \Gamma_{\text{DSS}}\Gamma_{\text{XDD}} - \Gamma_{\text{XSD}}\Gamma_{\text{XDS}} \\
&\quad - \frac{1}{2}(\Gamma_{\text{XDD}} - \Gamma_{\text{SDD}})^2 - \frac{1}{2}(\Gamma_{\text{XDD}} + \Gamma_{\text{DDD}})^2. \tag{3.14}
\end{aligned}$$

The only fixed point that we have identified is the non-interacting one. These ten coupled flow equations can be integrated numerically starting from bare interactions. In order to represent the property that same layer interactions will be slightly stronger than different layer interactions we set the bare values of the scattering amplitudes to 1.1, 0.9 and 0 for $v_0 V_S$ (represents $V_{\text{SSD}}, V_{\text{SDS}}, V_{\text{SDD}}$), $v_0 V_D$ (represents $V_{\text{DSS}}, V_{\text{DSD}}, V_{\text{DDS}}, V_{\text{DDD}}$) and $v_0 V_X$ (represents $V_{\text{XSD}}, V_{\text{XDS}}, V_{\text{XDD}}$), respectively.

(The motivation for this choice is explained in the next section.) We find that the interaction parameters flow away from the non-interacting fixed point and diverge at a finite value of s as illustrated in Fig. 3.8. The instability criterion implied by this one-loop PRG calculation is $V_D v_0 \simeq 0.6/\ln(s)$. The instability tendency is therefore enhanced by the spin and valley degrees of freedom since the criterion was $V_D v_0 \simeq 1/\ln(s)$ for the spinless and valleyless case.

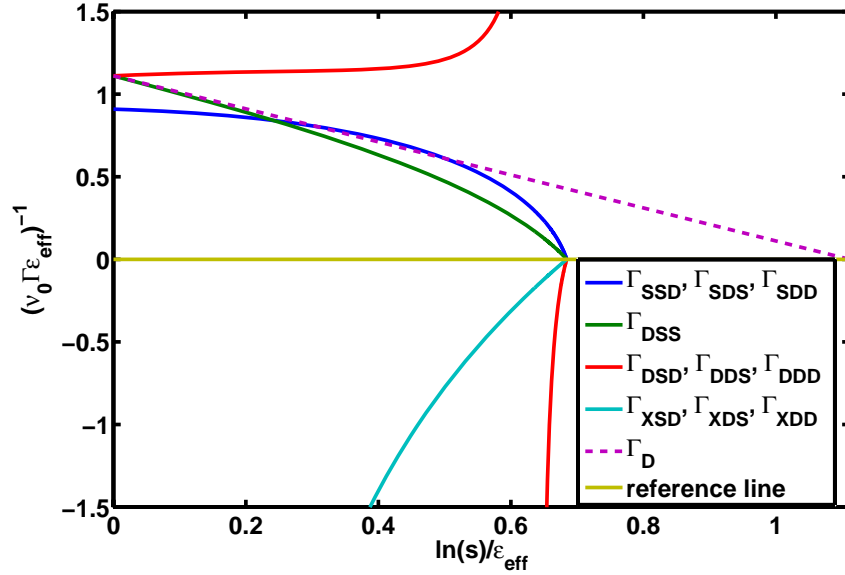


Figure 3.8: This illustration plots the inverse interaction strength $(v_0 \Gamma \epsilon_{\text{eff}})^{-1}$ versus the scaling parameter $\ln(s)/\epsilon_{\text{eff}}$. ϵ_{eff} is the effective dielectric constant of the graphene bilayer and $\Gamma = \Gamma_{\text{vacuum}}/\epsilon_{\text{eff}}$. Interlayer interaction parameters Γ_{DSS} (green) and $\Gamma_{\text{XSD}}, \Gamma_{\text{XDS}}, \Gamma_{\text{XDD}}$ (cyan) flow to large values most quickly. According to this estimate the normal state becomes unstable for $v_0 V_D \geq 0.6/\ln(s)$.

When spin and valley is included, the tendency of the instability is actually enhanced, based on the above analysis. However, we should be careful to express the final ground state. In this full mode, there are four species of electrons, one for each valley and each spin, and each of them undergoes the spontaneous inversion symmetry breaking. The most stable final state is that two species transfer to one

layer and the other two species transfer to the other layer, although it is possible to have other possible states, all the four species transfer to one layer, or three species and the fourth one transfer to different layers respectively. The formation of a layer pseudospin ferromagnetic phase has an electrostatic energy cost. This broken symmetry phase, like the formation of exciton condensates in normal bilayer systems, is driven by interlayer exchange energy. A consideration of the full exchange interaction shows that it can overcome the electrostatic contribution. Therefore, the broken symmetry phase is stable and favored.

3.3.5 Influence of trigonal warping and external potential

The conclusions which can be drawn from the PRG calculation presented here are sensitive to the upper and lower momentum and energy cutoffs, which limit the applicability of the massive chiral fermion model for bilayer graphene, and to the strength of bare electron-electron scattering amplitudes. Below we estimate the range of s over which the RG flows discussed above apply, and the strength of the bare interaction V_D . We caution that, given the nature of the PRG calculations, the estimates presented below should be regarded as qualitative.

In practice the upper cutoff is the interlayer hopping energy $E_H = \gamma_1 \sim 0.4$ eV; at higher energies it is essential to account for two sublattice sites in each layer. We have in addition ignored the trigonal-warping part in the full Hamiltonian, due to a direct hopping process between the low-energy sites which has energy scale [3, 26] $\gamma_3 \sim 0.3$ eV. Inserting the expression for the effective mass of the massive chiral Fermion model we find that the model we have studied is appropriate for

$$\hbar v_F q \frac{\gamma_3}{\gamma_0} \leq \frac{\hbar^2 q^2}{2m^*} = \frac{\hbar^2 q^2 v_F^2}{\gamma_1} \leq \gamma_1 \quad (3.15)$$

where $v_F \sim 10^8$ cm/s is the Fermi velocity near the Dirac point in the single-layer-graphene continuum model, and $\gamma_0 \sim 3$ eV is the intralayer near neighbor hopping energy. It follows that the high energy momentum cutoff $q_H = \gamma_1/\hbar v_F$ and that the low energy momentum cutoff $q_L = (\gamma_3\gamma_1/\gamma_0)/\hbar v_F$, which gives the maximum value of the scaling parameter $\ln(s)$. Using accepted values for the hopping parameters[3, 26], it follows that the scaling relations we derive should apply approximately over a wavevector range corresponding to $\ln(s)_{\max} = \ln(q_H/q_L) \simeq \ln(\gamma_0/\gamma_3) \simeq 2.3$.

If a small external potential difference $2U$, where $U = \eta \gamma_1$ and $\eta \ll 1$, is applied between the layers, it adds a single-particle term $U \tau^z$ [4, 6, 33] to the single-particle Hamiltonian, and hence breaks inversion symmetry. Then the low energy limit is

$$E_L = \max \left\{ \eta \gamma_1, \left(\frac{\gamma_3}{\gamma_0} \right)^2 \gamma_1 \right\}. \quad (3.16)$$

It's easily to find that $\eta_L = (\gamma_3/\gamma_0)^2 \sim 0.01$ is the critical value above which the low energy limit is determined by the external potential difference between the layers rather than the intrinsic trigonal warping.

We estimate the strength of the bare interactions by evaluating the 2D Coulomb scattering potential at the cutoff wavevector q_H :

$$v_0 V_S \simeq \frac{m^*}{2\pi\hbar^2} \frac{2\pi e^2}{q_H} = \frac{\alpha_{ee}}{2} \quad (3.17)$$

where $\alpha_{ee} = e^2/\hbar v_F \simeq 2.2$ is graphene's fine structure constant. Based on the instability criterion, larger interactions are more likely to break symmetry. Evaluating the interaction strength at high cutoff gives the minimal value. We argue that the instability occurs even at minimal interactions. The initial values used in the RG

flows is motivated by this estimate. The value used for V_D is reduced by a factor of $\exp(-q_H d)$ compared to V_S to account for the layer separation $d = 3.35 \text{ \AA}$. Taking into account both the direct and exchange contributions, we easily get the bare values of the scattering amplitudes we use in the last section.

If no external potential difference is applied between the layers, according to these estimates the bare value of $v_0 V_D$ exceeds the stability limit of $\sim 0.6/\ln(s)_{\max} \sim 0.25$ by approximately a factor of four. The above estimates are for the case of a graphene bilayer in vacuum. For graphene layers on the surface of a substrate with dielectric constant ϵ , interactions are expected to be reduced by a factor of $\sim (\epsilon + 1)/2$. In the case of SiO_2 substrates $\epsilon \sim 4$ and the interaction strength exceeds the stability limit by a much narrower margin.

Applying potential difference between the layers does give rise a small energy gap. There is another critical value of $\eta_H \sim 1/3$, namely, $\ln(s)_{\max} = -(\ln \eta_H)/2$ and it satisfy $v_0 V_D = 0.6/\ln(s)_{\max}$. Above this value, the momentum shell valid for the chiral model is too narrow to support the occur of spontaneous symmetry breaking. Therefore the small energy gap around the Dirac points are governed dominantly by this large potential difference. Both electron-electron interactions and the potential difference between the layers have the potential to open a energy gap around the Dirac points in suspended GB, however, the larger the potential difference, the less possibility of the occur of the spontaneous layer inversion symmetry breaking. We summarize in the Table 3.2 how interactions and potential differences play their roles in the model we use and determine whether breaking inversion symmetry occurs in suspended GBS.

The strength of the instabilities, at least for high quality suspended graphene bilayers and small external potential differences between the layers, are large enough to lead some consequences which can be observed in experiments, although

Table 3.2: Summary of whether the electron-electron interactions drive a suspended graphene bilayer, with different values of the potential difference between the layers, to a spontaneous layer inversion symmetry breaking state and hence open a gap

η	Chiral Model	E_L/γ_1	Instability	Dominant
$0 \leq \eta < \eta_L$	Valid	$(\gamma_3/\gamma_0)^2$	Yes	V_D
$\eta_L \leq \eta < \eta_H$	Valid	η	Yes	V_D
$\eta_H \leq \eta < 1$	Valid	η	No	$U \tau^z$
$\eta \geq 1$	Beyond Chiral	\	No	$U \tau^z$

trigonal warping effect does give rise some inhomogeneities and anisotropy, and the external potential difference breaks inversion symmetry and transfers charge between layers.

3.4 Spontaneous layer inversion symmetry breaking

3.4.1 Susceptibilities and which symmetry is broken

There must be a spontaneous broken symmetry in bilayer graphene since the interaction coupling constants blow up in the RG flows. To show which symmetry is broken, we need to investigate the pseudospin susceptibilities, namely, the pseudospin-pseudospin response functions defined as following

$$\chi_{TB}(\mathbf{q}, i\omega) = \int_0^\beta d\tau e^{i\omega\tau} \langle T_\tau S_T(\mathbf{q}, \tau) S_B(-\mathbf{q}, 0) \rangle, \quad (3.18)$$

$$S_\alpha(\mathbf{q}, \tau) = \sum_{\mathbf{k}} c_{\mathbf{k}+\mathbf{q}, i}^\dagger \sigma_{ij}^{(\alpha)} c_{\mathbf{k}j}, \quad (3.19)$$

where S_α is the spin-density operator for $\alpha = x, y, z$ component. The ordering tendencies are determined by the logarithmical divergencies in the normal state pseudospin susceptibilities. $\langle S_z(\mathbf{r}) \rangle$ is the order parameter of a gapped phase with inversion symmetry breaking and pseudospin ferromagnetism perpendicular to the graphene layers for a single spin-valley. We will show this phase has fine classifications and each class exhibits different nontrivial spontaneous Hall conductivity. $\langle S_x(\mathbf{r}) \rangle$ or $\langle S_y(\mathbf{r}) \rangle$ describe a gapless phase with in-plane rotational symmetry breaking. This nematic phase breaks the lattice point group symmetry by splitting the original vorticity $N = 2$ (Berry phase 2π) Dirac point (or say the valley cone including the center Berry phase π Dirac point and three Berry phase $-\pi$ Dirac points symmetrically surrounded the center one when trigonal warping effect is considered) into two vorticity $N = 1$ Dirac points along the easy axes. But we will demonstrate that this gapless nematic phase is not the physical case in bilayer graphene because the dominance of broken inversion symmetry. Therefore it is of utmost importance to compare the divergencies of χ_{zz} and χ_{xx} (or χ_{yy}). The calculations of these pseudospin-pseudospin response functions can be systematically done with the Feynman diagrams specified in Fig. 3.9. Fig. 3.9(a) denotes the non-interacting pseudospin susceptibility χ_{TB}^0 and Fig. 3.9(b) shows the interaction mediated pseudospin susceptibility $\chi_{\text{TB}}^{\text{I}}$. In the long wavelength and static limit, the susceptibilities explicitly read

$$\begin{aligned}
\chi_{\text{TB}}^0 &= -\int \frac{d^2 \mathbf{q}}{(2\pi)^2 (\beta \hbar^2)} \sum_{\omega} \sum_{\alpha_{\text{T}} \beta_{\text{T}}} \sum_{\alpha_{\text{B}} \beta_{\text{B}}} \mathcal{G}_{\alpha_{\text{B}} \alpha_{\text{T}}}(\mathbf{q}, i\omega) \sigma_{\alpha_{\text{T}} \beta_{\text{T}}}^{(\text{T})} \mathcal{G}_{\beta_{\text{T}} \beta_{\text{B}}}(\mathbf{q}, i\omega) \sigma_{\beta_{\text{B}} \alpha_{\text{B}}}^{(\text{B})}, \\
\chi_{\text{TB}}^{\text{I}} &= -\int \frac{d^2 \mathbf{q}_1 d^2 \mathbf{q}_2}{(2\pi)^4 (\beta \hbar^2)^2} \sum_{\omega_1 \omega_2} \sum_{\text{all } \alpha \beta} \mathcal{G}_{\alpha_1 \alpha_{\text{T}}}(\mathbf{q}_1, i\omega_1) \sigma_{\alpha_{\text{T}} \beta_{\text{T}}}^{(\text{T})} \mathcal{G}_{\beta_{\text{T}} \beta_1}(\mathbf{q}_1, i\omega_1) \\
&\quad \times \Gamma_{\alpha_2 \beta_2}^{\beta_1 \alpha_1} \mathcal{G}_{\beta_2 \beta_{\text{B}}}(\mathbf{q}_2, i\omega_2) \sigma_{\beta_{\text{B}} \alpha_{\text{B}}}^{(\text{B})} \mathcal{G}_{\alpha_{\text{B}} \alpha_2}(\mathbf{q}_2, i\omega_2). \tag{3.20}
\end{aligned}$$

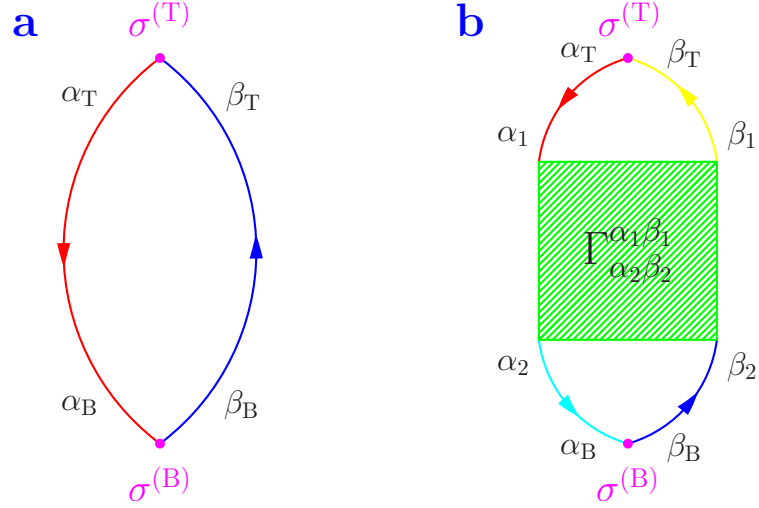


Figure 3.9: Feynman diagrams for the pseudospin susceptibilities. **(a)** χ_{TB}^0 the non-interacting susceptibility and **(b)** χ_{TB}^I the interacting correction to the susceptibility.

In bilayer graphene systems, near charge neutrality, the layer pseudospin susceptibilities are simplified as following

$$\begin{aligned}
 \chi_{zz}^{(0)} &= 2\chi_{xx}^{(0)} = 2\chi_{yy}^{(0)}, \\
 \chi_{zz}^{(I)} &= 4\chi_{xx}^{(I)} = 4\chi_{yy}^{(I)},
 \end{aligned}
 \tag{3.21}$$

which indicates that the divergence in χ_{zz} channel would be dominant. Note that the transverse channels, χ_{xx} and χ_{yy} , are relatively suppressed by the large pseudospin chirality. In result, the ground state of bilayer graphene is a gapped phase with spontaneously breaking layer inversion symmetry in each spin-valley. We will discuss in the next chapter that this insulating state is a topologically nontrivial state with spontaneous quantum Hall effects[9, 13, 17] at zero external fields.

3.4.2 Mean-field pseudospin orientation

When interactions are neglected, a neutral chiral graphene is a gapless semiconductor. The ground state has a full valence band of pseudospinors aligned at each \mathbf{q} to the pseudospin field direction $(\cos(N\phi_{\mathbf{q}}), \sin(N\phi_{\mathbf{q}}), 0)$, forming the momentum-space vortex. Note that the chirality of the vortices are opposite at valley K and K' and we focus on a single spin-valley. The vortex exacts a large interaction energy penalty because of its rapid pseudospin-orientation variation. We propose[9, 10, 15] that, like its real-space counterpart, the momentum-space vortex sidesteps this energy cost by forming a vortex core in which the pseudospin orientation is out of plane in either the \hat{z} or $-\hat{z}$ direction. Since we have known from the PRG and susceptibility analysis that the mean fields generated by interactions are proportional to σ_z , mean-field calculations would be sufficient to provide correct pictures. We summarize the results in Fig.3.10 using weak electron-electron interactions in chirally-stacked N -layer graphene with $N = 1, 2, 3$ and 4, respectively.

Clearly, a vortex core only forms in chiral graphene with layer number $N \geq 2$ where the weak repulsive interaction instability occurs at charge neutrality point. Furthermore, the instability is stronger for a larger N system, which results from the fact that the interactions are marginally relevant at one-loop level in bilayer and relevant even at tree-level in $N > 2$ layers. However, as the number of layers grows, the interlayer bare interactions start to be suppressed and screened, and the remote hopping processes become more and more important and thus the chiral description starts to break down. Therefore, we only expect the broken symmetry states in chiral few-layers with $N < 5$. Recently, the gapped broken symmetry ground states have been observed in high quality graphene bilayers[13, 17, 18] and trilayers[68].

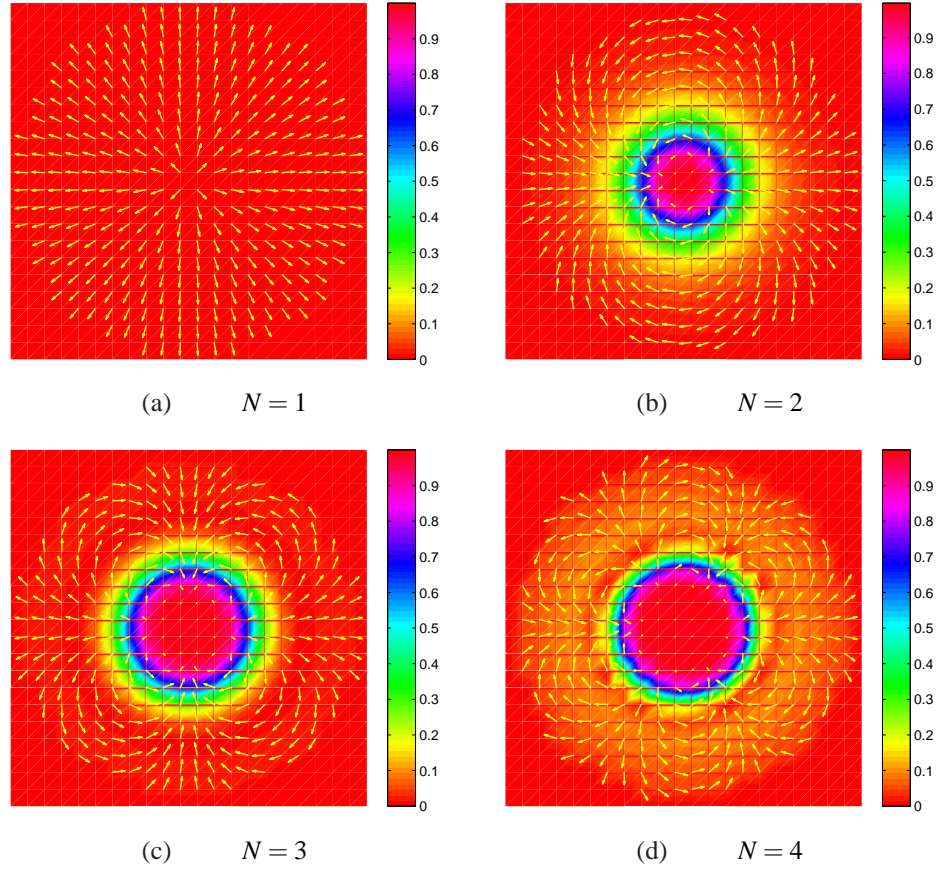


Figure 3.10: The pseudospin orientation of chirally stacked graphene few-layers with **(a)** $N = 1$, **(b)** $N = 2$, **(c)** $N = 3$ and **(d)** $N = 4$ in momentum space. The length of an arrow denotes the pseudospin in-plane amplitude and orientation while the background intensity represents the amplitude of out-of-plane pseudospin. The range we plot here is from the Dirac point (the origin) to $q = \gamma_1/(\hbar v_F)$. There is no broken symmetry for $N = 1$ while the inversion symmetry is spontaneously broken for $N \geq 2$ in the nonzero intensity region centered at the Dirac point. The instability is stronger for larger N . In the Hartree Fock mean-field calculations, we use long-range Coulomb interactions and choose a dielectric constant $\epsilon = 2.2$. The broken symmetries would be even stronger in the suspended case.

3.5 Bilayer graphene Dirac-point gaps and symmetry-breaking states

3.5.1 Introduction

This section details the analysis which leads to the conclusion that the gaps [10, 15, 46] observed in the quasiparticle spectrum of bilayer graphene likely reflect the formation of spontaneous quantum Hall states[9, 20, 21]. Because of the relatively small value of the observed gap, we conclude that it must be due to the physics of low-energy band states near the K and K' valley Dirac points. We therefore analyze the properties of these states using bilayer graphene's continuum $\mathbf{k}\cdot\mathbf{p}$ model. When a broken symmetry state is formed the Hamiltonian that describes quasiparticles can have additional terms due to interactions with the condensate. Because electron-electron interactions within a valley are much stronger than inter-valley interactions we restrict our attention to condensates that do not couple quasiparticles in different valleys. Since the gap forms near the Dirac point we neglect the momentum dependence of the interaction with the condensate which should not play an essential role. We allow the interaction with the condensate to be spin-dependent, but assume collinearity. Non-collinear states are indeed likely when Zeeman coupling is included[16], but allowing this possibility does not increase the gap size. Given these assumptions, we can analyze the gap properties associated with different types of order quite thoroughly, both in the absence and in the presence of a magnetic field. In the following discussion we follow common usage in referring to points in momentum space at which the gap between conduction and valence bands vanishes as Dirac points.

Experimentally the observed gap is an even function of an electric field be-

tween the layers[13, 17], implying that the broken symmetry state does not break overall inversion symmetry. Inversion symmetry that is broken[10] in opposite senses for different spins or valleys, is however consistent with experiment. Indeed we will argue that only this type of broken symmetry can produce the observed gaps.

3.5.2 Full $k \cdot p$ Hamiltonian of bilayer graphene

The starting point of our analysis is the massless Dirac-Weyl $k \cdot p$ Hamiltonian for monolayer graphene[3]:

$$\hat{H}_{N=1} = v_0 \begin{pmatrix} 0 & \pi^\dagger \\ \pi & 0 \end{pmatrix}, \quad (3.22)$$

where $\pi = \tau_z p_x + i p_y$ and $\tau_z = +(-)$ for valley $K(K')$. The matrix operator in this Hamiltonian acts on the single-layer sublattice degree-of-freedom. We focus on bands near Brillouin zone corner K ; results for valley K' can be obtained by setting p_x to $-p_x$. The bilayer π -bands are a direct product of two sets of monolayer bands, modified by the various interlayer coupling processes identified below. In the representation in which the bilayer sublattice sites are ordered $\{A_1, B_1, A_2, B_2\}$, the bilayer Hamiltonian near valley K can be written in the form:

$$\hat{H}_{N=2} = \begin{pmatrix} 0 & v_0 \pi^\dagger & v_4 \pi^\dagger & v_3 \pi \\ v_0 \pi & 0 & \gamma_1 & v_4 \pi^\dagger \\ v_4 \pi & \gamma_1 & 0 & v_0 \pi^\dagger \\ v_3 \pi^\dagger & v_4 \pi & v_0 \pi & 0 \end{pmatrix}, \quad (3.23)$$

where $v_i = \sqrt{3}a\gamma_i/2\hbar$ and $a = 0.246\text{nm}$. The band parameter values[52], $\gamma_0 = 3.16$ eV, $\gamma_1 = 0.40$ eV, $\gamma_3 = 0.315$ eV, $\gamma_4 = -0.044$ eV are generally accepted to be reasonably accurate. We treat finite- π coupling between the low- and high-energy subspaces of this Hamiltonian, which are separated by an interlayer tunneling energy scale, perturbatively. For this purpose it is convenient to change the sublattice order to one which lists the low-energy sites first: $\{(A_1, B_2)_1, (B_1, A_2)_2\}$. In this notation the low-energy effective band Hamiltonian at finite π is[6]

$$\mathcal{H}_{\text{eff}} = [1 + H_{12}(H_{22})^{-2}H_{21}]^{-1}[H_{11} - H_{12}(H_{22})^{-1}H_{21}]. \quad (3.24)$$

The second factor on the right-hand side of this equation captures the effects of direct hopping between the low-energy sites A_1 and B_2 and of virtual hopping via high-energy states, while the first captures an inessential energy scale renormalization by a factor of order $1 - (v_0p/\gamma_1)^2$ which is usually dropped[4, 6]. We find that the low-energy $\mathbf{k}\cdot\mathbf{p}$ Hamiltonian for bilayer graphene can be written in the form

$$\begin{aligned} \mathcal{H} = & -\frac{v_0^2 p^2}{\gamma_1} [\cos(2\phi_p) \sigma_x + \sin(2\phi_p) \sigma_y] \\ & + v_3 p [\cos(\phi_p) \sigma_x - \sin(\phi_p) \sigma_y] - \frac{2v_4 v_0 p^2}{\gamma_1} \sigma_0. \end{aligned} \quad (3.25)$$

The Pauli matrices in this Hamiltonian act on the low-energy sublattice degrees of freedom which forms a layer pseudospin. The first term on the right hand side of Eq.(3.25) dominates at large p and the second term at small p . When the two terms are of comparable size their interference leads to angular variation in the bands that is invariant under a 120° rotation (trigonal warping). The term proportional to γ_4 breaks particle-hole symmetry, but is usually ignored below because it does not materially alter the gap properties on which we focus.

The general form of the low energy bilayer quasiparticle Hamiltonian can be written in the following compact manner:

$$H(\mathbf{k}) = -\frac{1}{2m} \begin{pmatrix} 0 & \pi^{\dagger 2} \\ \pi^2 & 0 \end{pmatrix} + \lambda \begin{pmatrix} 0 & \pi \\ \pi^{\dagger} & 0 \end{pmatrix} + \Delta \cdot \boldsymbol{\sigma} \quad (3.26)$$

where the coefficient $\lambda = v_3$ is an indirect measure of the trigonal warping strength and $\Delta = (\Delta_x, \Delta_y, \Delta_z)$ parameterizes interactions with the condensate. (A $\Delta_0 \sigma_0$ term must be also present, but plays no role apart from a shift in the zero of energy.)

The low-energy band-structure of bilayer graphene in the absence of interactions and external fields is therefore gapless. The gapless property and the degeneracy at the Dirac point $\mathbf{p} = 0$ is protected by inversion symmetry with respect to a point midway between A_1 and B_2 . As we explain in the following sections, any perturbation of the bilayer graphene quasiparticle Hamiltonian that does not break this inversion symmetry can not open a gap at the Dirac point[9, 10, 15, 20, 21, 46].

3.5.3 Trigonal warping does not yield a gapped state

The trigonal warping effect dominates at energies below ~ 1 meV. Physics on this energy scale is likely to be smeared by unintended disorder or by electron-electron interactions even in the highest quality samples currently available, *i.e.* bilayers on h-BN substrates and suspended current-annealed bilayers. We nevertheless consider the ideal case of a perfectly clean sample with no interactions. When trigonal warping is neglected the chiral Hamiltonian has a single Dirac point at $\mathbf{p} = 0$, the spectrum is rotationally invariant, and the phase difference between sublattices changes by 4π when the quasiparticle-momentum circles the Dirac point, a property we refer to as $J = 2$ chirality. When trigonal warping is included the gap between

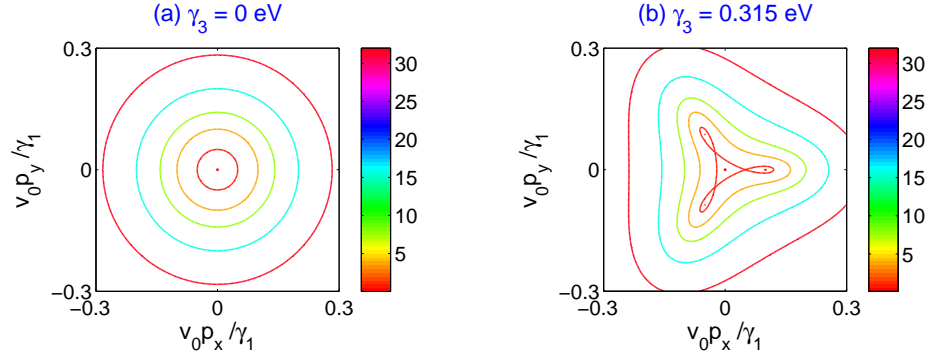


Figure 3.11: Constant energy contour plots of the conduction band of bilayer graphene near valley K . (a) The gap vanishes at one point in momentum space and the spectrum is rotationally invariant when $\gamma_3 = 0$; (b) The gap vanishes at four points in momentum space and the spectrum has \mathcal{C}_3 rotational symmetry when $\gamma_3 = 0.315$ eV. The contour energies are 32, 16, 8, 4, 1, and 0 meV from outer to inner. The total spectrum has particle-hole symmetry, since γ_4 has been set to zero.

conduction and valence bands vanishes at $\mathbf{p} = 0$ and also at three additional $\mathbf{p} \neq 0$ points where the coefficients of both σ_x and σ_y sublattice-pseudospin operators vanish. The central Dirac point at $\mathbf{p} = 0$ has $J=-1$ whereas the three surrounding points at $p = v_3 \gamma_1 / v_0^2$ and $\phi = 0, \pm 2\pi/3$ have $J = 1$. These features are illustrated in Figure 3.11. In general a gap in the quasiparticle spectrum can occur only if the coefficients of the σ_x , σ_y and σ_z pseudospin operators do not vanish simultaneously at any value of \mathbf{p} .

3.5.4 Nematic order does not yield a gapped state

The σ_z layer-pseudospin operator measures the density difference between top and bottom layers whereas σ_x and σ_y measure interlayer coherence. When its inessential momentum dependence is dropped, the interactions of quasiparticles of a particular valley and spin with the condensate can be expanded in terms of these Pauli

matrices, as mentioned earlier. Researchers have reached different conclusions concerning the character of the broken symmetry state. Some researchers[47, 69] have concluded that the interaction with the condensate leads to a pseudospin effective magnetic field in the $x - y$ plane which lowers the rotational symmetry of the bands. This ordered state is therefore referred to as a nematic and has the quasiparticle-condensate interaction

$$\mathcal{H}_{\text{Nematic}} = \Delta_x \sigma_x + \Delta_y \sigma_y. \quad (3.27)$$

The quasiparticle spectrum of $\mathcal{H} + \mathcal{H}_{\text{Nematic}}$ (dropping γ_4 is)

$$E^2 = \left[\frac{(v_0 p)^2}{\gamma_1} \cos(2\phi_p) - v_3 p \cos(\phi_p) - \Delta_x \right]^2 + \left[\frac{(v_0 p)^2}{\gamma_1} \sin(2\phi_p) + v_3 p \sin(\phi_p) - \Delta_y \right]^2. \quad (3.28)$$

This spectrum is gapless for any value of Δ_x and Δ_y , since we are always able to locate points in momentum space at which the total pseudospin effective field, and hence the gap, vanishes. To see this note that the gap vanishes when the following two equations are solved simultaneously:

$$\left(p_x - \frac{v_3 \gamma_1}{2v_0^2} \right)^2 - p_y^2 = \frac{\Delta_x \gamma_1}{v_0^2} + \frac{v_3^2 \gamma_1^2}{4v_0^4}, \quad (3.29)$$

$$p_y \left(p_x + \frac{v_3 \gamma_1}{2v_0^2} \right) = \frac{\Delta_y \gamma_1}{2v_0^2}. \quad (3.30)$$

Eq.(3.29) describes a hyperbola with orthogonal asymptotes $p_x \pm p_y - v_3 \gamma_1 / (2v_0^2) = 0$ whereas Eq.(3.30) describes a hyperbola with orthogonal asymptotes with $p_y = 0$ and $p_x + v_3 \gamma_1 / (2v_0^2) = 0$. Since their asymptotes intersect, there must be at least two

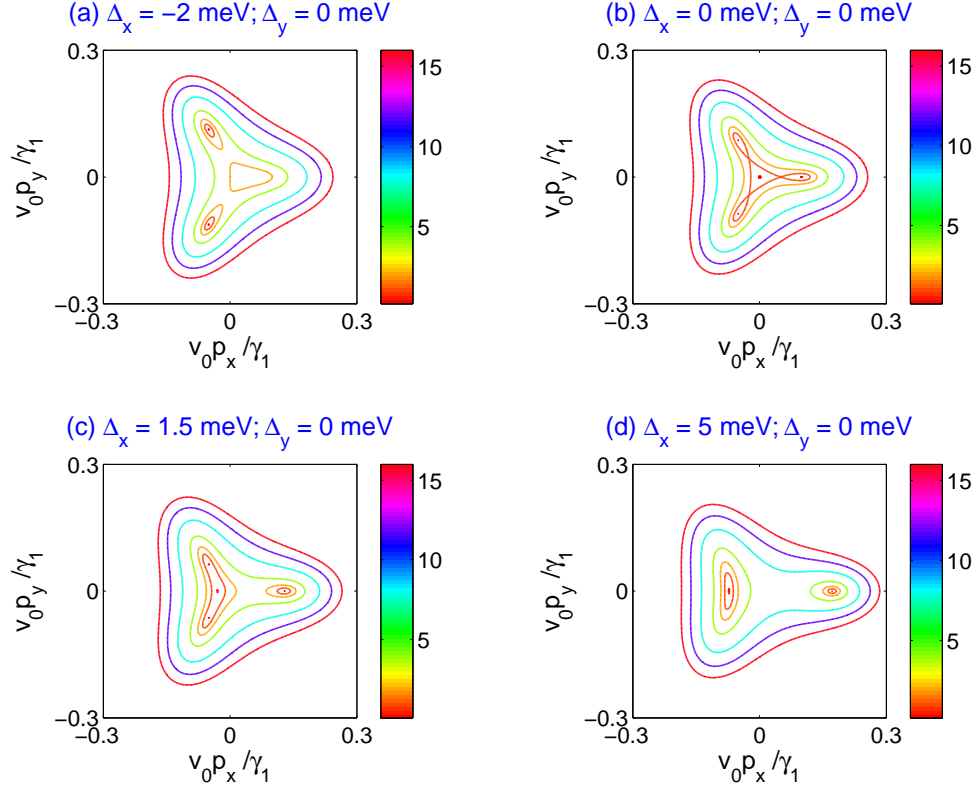


Figure 3.12: Constant energy contour plots of the conduction band near valley K of bilayer graphene for σ_x nematic order. Nonzero Δ_x breaks the \mathcal{C}_3 symmetry but the spectrum is still gapless. The contour energies are 16,12,8,4,2,1,0 meV from outside to inside. There are 2, 4, 4, and 2 Dirac points in (a), (b), (c) and (d) respectively. These plots were constructed using $\gamma_3 = 0.315$ eV and $\gamma_4 = 0$.

points of intersection between the two curves. It follows that the spectrum defined by Eq.(3.28) is gapless with at least two Dirac points.

The influence of nematic order on the bands can be understood simply in the illustrative special case $\Delta_y = 0$. It then follows from Eq.(3.30) that Dirac points can occur only along the lines $p_y = 0$ and $p_x = -v_3\gamma_1/(2v_0^2)$. Substituting $p_y = 0$ into Eq.(3.29), we find two Dirac points with $J = \pm 1$ chirality if $\Delta_x > -v_3^2\gamma_1/(4v_0^2)$

which annihilate when this inequality is not satisfied. (See Figure 3.12(a) and (b).) The other pair of Dirac points appear at $p_y = \pm \sqrt{3v_3^2\gamma_1^2/(4v_0^4) - \Delta_x\gamma_1/v_0^2}$ and $p_x = -v_3\gamma_1/(2v_0^2)$ which implies that $\Delta_x < 3v_3^2\gamma_1/(4v_0^2)$ is a necessary condition for the appearance of these two gapless Dirac points. Moreover, $p_x = -v_3\gamma_1/(2v_0^2)$ and $\Delta_x = 3v_3^2\gamma_1/(4v_0^2)$ indicate $p_y = 0$. Three Dirac points (one with $J = -1$ and a pair of points with $J = 1$) fuse into a single $J = 1$ Dirac point when $\Delta_x \geq 3v_3^2\gamma_1/(4v_0^2)$, as illustrated in Figure 3.12(b)-(d). The sum of the chirality of the Dirac points is $J_{tot} = 2$ for any value of the order parameter fields.

We conclude that the nematic order is not consistent with a gap.

3.5.5 Relative layer displacement does not yield a gapped state

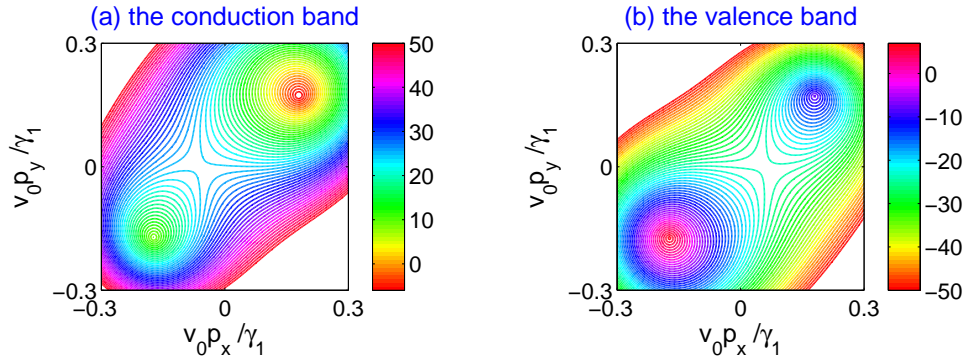


Figure 3.13: Constant energy contour plots of (a) the conduction band and (b) the valence band near valley K in a bilayer graphene samples in which one layer has been displaced relative to the other. This illustration is for a displacement with magnitude $d = 0.05a/\sqrt{3}$ and orientation $\phi_d = 0$. The relative displacement breaks the \mathcal{C}_3 and particle-hole symmetries. However, the spectrum is still gapless. The increment between constant energy contours in this plot is 1 meV. This illustration is for the parameters $\gamma_3 = 0.315$ eV and $\gamma_4 = -0.044$ eV.

In order to achieve high mobility, suspended bilayer graphene samples are

annealed by large currents. The consequent Joule heating may remove adsorbates but could potentially alter the bilayer structure, for example by displacing one layer relative to the other. Only very simple and systematic changes in structure have any chance of inducing a gap in the spectrum. Here we explore the effect of displacing one layer relative to the other and appeal to the $\mathbf{k}\cdot\mathbf{p}$ analysis of Ref.[70], which implies the interlayer hopping Hamiltonian (see Eq.(3.23)) is altered in the following way:

$$\begin{pmatrix} v_4\pi^\dagger & v_3\pi \\ \gamma_1 & v_4\pi^\dagger \end{pmatrix} \implies \begin{pmatrix} v_4\pi^\dagger & v_3\pi \\ \gamma_1 & v_4\pi^\dagger \end{pmatrix} + \begin{pmatrix} t_4 & t_3 \\ t_1 & t_4 \end{pmatrix}. \quad (3.31)$$

The t_i 's account for the change in the interlayer tunneling Hamiltonian evaluated at $\pi = 0$:

$$\begin{aligned} \begin{pmatrix} t_4 & t_3 \\ \gamma_1 + t_1 & t_4 \end{pmatrix} &= \frac{\gamma_1}{3} \begin{pmatrix} 1 & 1 \\ 1 & 1 \end{pmatrix} + \frac{\gamma_1}{3} e^{iGd\cos(\phi-5\pi/6)} \begin{pmatrix} e^{i2\pi/3} & e^{-i2\pi/3} \\ 1 & e^{i2\pi/3} \end{pmatrix} \\ &+ \frac{\gamma_1}{3} e^{iGd\cos(\phi+5\pi/6)} \begin{pmatrix} e^{-i2\pi/3} & e^{i2\pi/3} \\ 1 & e^{-i2\pi/3} \end{pmatrix}, \end{aligned} \quad (3.32)$$

where $G = 4\pi/(\sqrt{3}a)$ and \mathbf{d} is the sliding vector[70]. When this contribution to the interlayer tunneling Hamiltonian is treated perturbatively we obtain the following result for the *sliding* correction to the interlayer tunneling Hamiltonian:

$$\begin{aligned} \mathcal{H}' &= \frac{1}{\gamma_1^2} \begin{pmatrix} 0 & (v_0\pi^\dagger)^2 t_1^* \\ (v_0\pi)^2 t_1 & 0 \end{pmatrix} + \begin{pmatrix} 0 & t_3 - t_4^2/\gamma_1 \\ t_3^* - t_4^{*2}/\gamma_1 & 0 \end{pmatrix} \\ &- [t_4(v_0\pi) + t_4^*(v_0\pi^\dagger)]/\gamma_1 \begin{pmatrix} 1 & 0 \\ 0 & 1 \end{pmatrix}. \end{aligned} \quad (3.33)$$

Similar results have been obtained previously for bilayers in which the structure has been altered by sliding[71], or uniaxial strain[72]. The first term in this equation makes an unimportant change in the $J = 2$ chiral Hamiltonian. The second momentum-independent term is equivalent to nematic order with $\Delta_x - i\Delta_y = t_3 - t_4^2/\gamma_1$, which reduces rotational symmetry to \mathcal{C}_{2v} , while the third term breaks particle-hole symmetry but preserves the topology of the spectrum. The equations for the Dirac points are similar to Eqs.(3.29) and (3.30) although the hyperbolic asymptotes are different. Importantly, the two sets of asymptotes are never parallel the two curves therefore always have points of intersection. Therefore, the sliding case is similar to the nematic order, although the particle-hole symmetry is broken. As illustrated in Figure 3.13, sliding does not produce a gap.

3.5.6 Broken inversion symmetry yield gap and Berry curvature

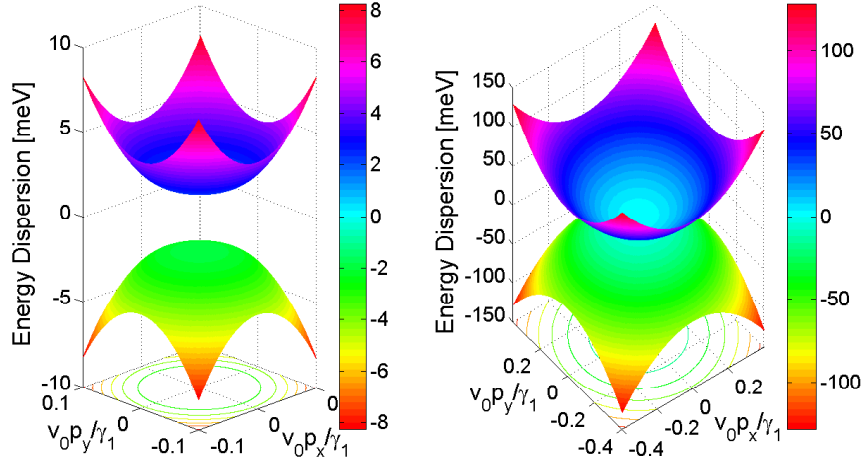


Figure 3.14: Low-energy dispersion near valley K for bilayer graphene with $\Delta_z = 2$ meV and $\gamma_3 = 0$. Nonzero Δ_z breaks inversion symmetry and introduces a gap $\sim 2\Delta_z$ at $\mathbf{p} = 0$.

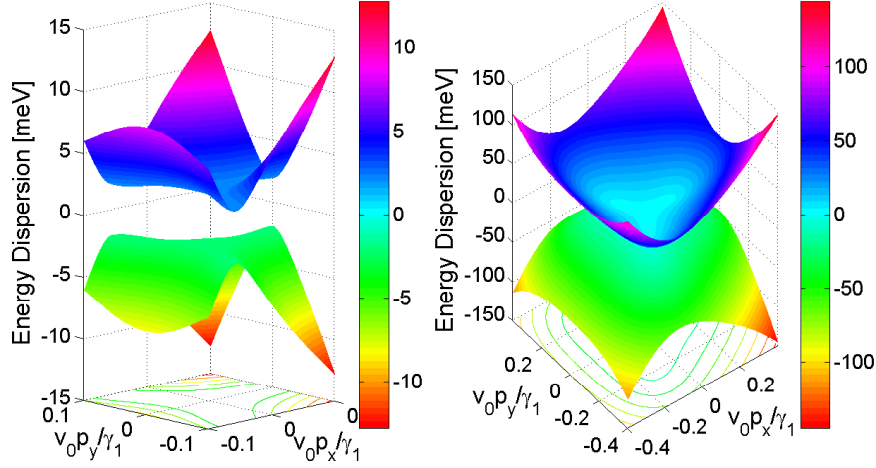


Figure 3.15: The low-energy dispersion near valley K of bilayer graphene with $\Delta_z = 2$ meV and $\gamma_3 = 0.315$ eV. Nonzero Δ_z breaks inversion symmetry and introduces a gap $\sim 2\Delta_z$ at $\mathbf{p} = 0$. The spectrum has \mathcal{C}_3 rotational symmetry when $\gamma_3 \neq 0$.

When layer inversion symmetry is broken within the four valley-spin flavors, either spontaneously[9, 10, 15, 46] or by external electric fields, a term of the form $\mathcal{H}_1 = \Delta_z \sigma_z$ appears in the quasiparticle Hamiltonian. Because there is no π -dependent band energy contribution that is proportional to σ_z there will always be a gap between conduction and valence bands when $\Delta_z \neq 0$. The energy dispersion for general Δ is

$$E^2 = \left[\frac{(v_0 p)^2}{\gamma_1} \cos(2\phi_p) - v_3 p \cos(\phi_p) - \Delta_x \right]^2 + \left[\frac{(v_0 p)^2}{\gamma_1} \sin(2\phi_p) + v_3 p \sin(\phi_p) - \Delta_y \right]^2 + \Delta_z^2, \quad (3.34)$$

which opens a band gap at Dirac points giving rise to $E = -|\Delta_z|$ on the top of the valence band and $E = |\Delta_z|$ at the bottom of the conduction band. A gap $\sim 2\Delta_z$ is clearly visible in Figure 3.14 and Figure 3.15 where trigonal warping is included

but has little influence. The valence band pseudospin points in the $\pm\hat{z}$ direction for $\mathbf{p} = 0$, and in the $\hat{x} - \hat{y}$ plane at large \mathbf{p} when the band terms in the Hamiltonian dominates. It follows that the pseudospin direction covers either the northern or southern hemisphere of the pseudospin Bloch sphere upon integrating over a small region of \mathbf{p} near the K and K' valleys, and hence that this region of momentum has large momentum space Berry curvatures[9] that vanish when $\Delta_z \rightarrow 0$.

Chapter 4

Spontaneous Quantum Hall States

Chirally stacked N -layer graphene with $N \geq 2$ is susceptible to a variety of distinct broken symmetry states in which each spin-valley flavor spontaneously transfers charge between layers. We explain in the first section how these states are distinguished by their charge, spin, and valley Hall conductivities, by their orbital magnetizations, and by their edge state properties. We also argue that valley Hall states have $[N/2]$ edge channels per spin-valley. In the second section, we focus on the edge states in the spinless case. We explicitly show that the quantum anomalous and valley Hall states are favored by a weak magnetic field and by an electric field between the graphene layers, respectively. More exotically, at interfaces between different phases one dimensional gapless modes exhibit novel Luttinger liquid behaviors. In section III, we analyze how the LAF and other competing states are influenced by Zeeman fields that couple to spin and by interlayer electric fields that couple to layer pseudospin, and comment on the possibility of using response and edge state signatures to identify the character of the bilayer ground state experimentally.

4.1 Spontaneous quantum Hall states

4.1.1 Introduction

In the early 1980s, following the discovery of the quantum Hall effect (QHE)[73], it was recognized[74] that electronic states can be characterized by topological indices, in particular by the integer valued Chern number indices that distinguish quantum Hall states. Quantum Hall states have non-zero Chern numbers and can occur only if time reversal symmetry (TRS) is broken; until recently they have been observed only when TRS is explicitly broken by an external magnetic field. In this article we discuss a class of broken symmetry states, first proposed theoretically[10, 15, 75] and recently discovered experimentally[17, 76], which appear in chirally stacked graphene systems and are characterized by spin and valley dependent spontaneous layer polarization. The aim of the present section is to explain how these states are distinguished by their charge[20, 77, 78], spin[79], and valley[80] quantized Hall conductances, by their orbital magnetizations, and by their edge state properties.

Success in isolating monolayer and few-layer sheets from bulk graphite, combined with progress in the epitaxial growth of few-layer samples, has opened up a rich new topic[3] in two-dimensional electron physics. Electron-electron interaction effects are most interesting in ABC-stacked $N \geq 2$ layer systems[4–6], partly because[10, 15, 21, 45–47] their conduction and valence bands are very flat near the neutral system Fermi level. For this special stacking order, low-energy electrons are concentrated on top and bottom layers and the low-energy physics of a N -layer system is described approximately by a two band model with $\pm p^N$ dispersion and large associated momentum-space Berry curvatures[8]. When these band states are described in a pseudospin language, the broken symmetry state is characterized[15] by

a momentum-space vortex with vorticity N and a vortex-core which is polarized in the top-or-bottom layers. For AB stacked bilayers, for example, interactions lead to a broken symmetry ground state[10, 15, 46] with a spontaneous gap in which charge is transferred between top and bottom layers. ABC-stacked trilayer graphene has even flatter bands and is expected to be even more unstable to interaction driven broken symmetries[6], but samples that are clean enough to reveal its interaction physics have not yet been studied.

4.1.2 Classification of broken symmetry states

We discuss the electronic properties of N -layer ABC-stacked systems using the ordered state quasiparticle Hamiltonians suggested by mean-field calculations[15, 46] and renormalization group analysis[10]

$$\mathcal{H}_N = \frac{(v_0 p)^N}{(-\gamma_1)^{N-1}} [\cos(N\phi_p)\sigma_x + \sin(N\phi_p)\sigma_y] + m\sigma_z. \quad (4.1)$$

We have used the notation $\cos\phi_p = \tau_z p_x/p$ and $\sin\phi_p = p_y/p$ where $\tau_z = \pm 1$ labels valleys K and K' , the two inequivalent Brillouin zone corners. The Pauli matrices σ act on a *which-layer* pseudospin degree-of-freedom and $s_z = \pm 1$ denotes the two spin flavors. In Eq. (4.1) the first term[4, 6] is the low-energy $\mathbf{k} \cdot \mathbf{p}$ band Hamiltonian for a single valley. Weak remote hopping processes have been dropped with the view that they do not play an essential role in the broken symmetry states[10]. The second term is an interaction-induced gap[10, 15, 21, 46] term which defines the direction of layer polarization in the momentum space vortex core. Since the pseudospin chirality frustrates off-diagonal symmetry-breaking[15], we consider only the pertinent types of diagonal symmetry-breaking. For each spin and valley, symmetry is broken by choosing a sign for m . We have dropped the momentum

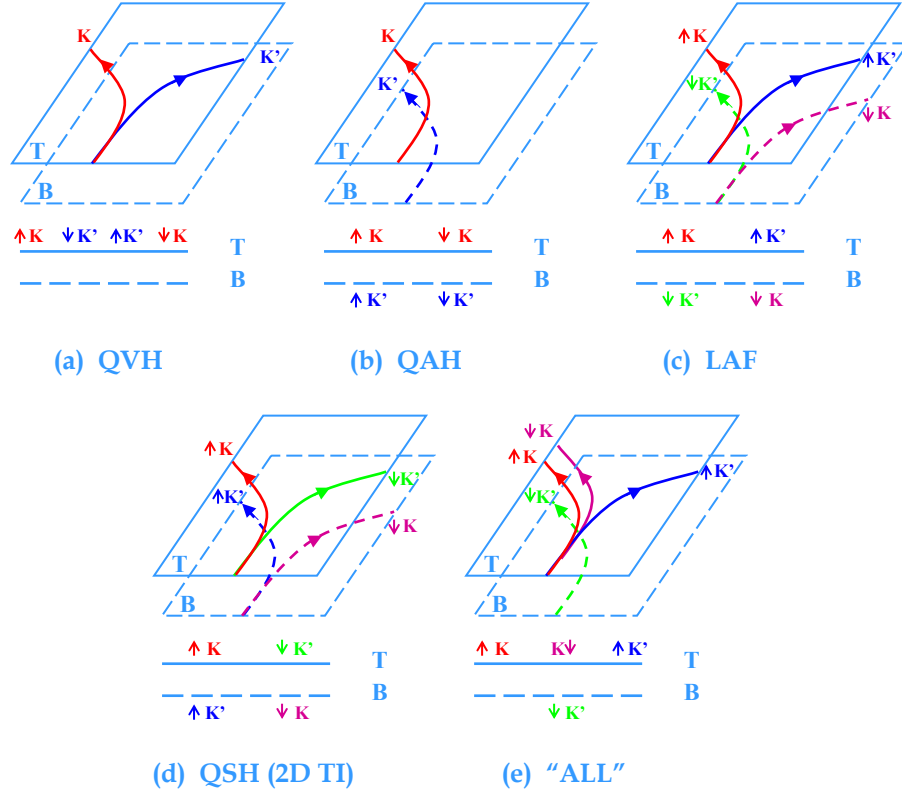


Figure 4.1: For cases (a-e) the lower panel describes the sense of layer polarization for each spin-valley combinations while the upper panel schematically indicates the corresponding Hall conductivity contributions[9]. (a) a valley Hall insulator with a net layer polarization and a mass $m\sigma_z$; (b) an anomalous Hall insulator with a valley-dependent mass $m\tau_z\sigma_z$; (c) a layer-antiferromagnetic insulator with a spin-dependent mass $m s_z\sigma_z$; (d) a quantum spin Hall (or 2D Topological) insulator with a valley and spin dependent mass $m\tau_z s_z\sigma_z$; (e) an exotic Hall state with a valley and spin dependent mass $m(\frac{1+\tau_z}{2} + \frac{1-\tau_z}{2}s_z)\sigma_z$.

dependence of m because, as we will see, it does not play an essential role below. $2|m|$ is the size of the spontaneous gap, v_0 is the Fermi velocity in graphene, and $\gamma_1 \sim 0.4$ eV is the interlayer hopping energy. The p^N dispersion is a consequence of the N -step process in which electrons hop between low-energy sites in top and bottom layers via high-energy states.

When spin and valley degrees-of-freedom are taken into account, the system has sixteen distinct broken symmetry states in which the sign of m is chosen separately for $(K \uparrow)$, $(K \downarrow)$, $(K' \uparrow)$ and $(K' \downarrow)$ flavors. We take the view that any of these states could be stable, depending on details that are beyond current knowledge and might be tunable experimentally. The sixteen states can be classified according to their total layer-polarization which is proportional to the sum over spin-valley of the sign of m . Six of the sixteen states have no net layer charge transfer between top and bottom layers and are likely to be lowest in energy in the absence of an external electric field. These six states can be separated into three doublets which differ only by layer inversion in every spin-valley. Thus three essentially distinct states compete for the broken symmetry ground state: the anomalous Hall state in which the sign of m is valley-dependent but not spin-dependent ($m\sigma_z \rightarrow m\tau_z\sigma_z$), the layer-antiferromagnetic state in which m is only spin-dependent ($m\sigma_z \rightarrow ms_z\sigma_z$) and the topological insulator (TI) state in which m is both spin and valley dependent ($m\sigma_z \rightarrow m\tau_zs_z\sigma_z$). These states are distinguished by their spin and valley dependent Hall conductivities and orbital magnetizations indicated schematically in Fig. 4.1 and summarized in Table 4.1.

4.1.3 Hall conductivities and orbital magnetizations

The three broken symmetry states on which we focus are distinguished by the signs of the Berry curvatures[8] contributions from near the K and K' valleys of \uparrow and \downarrow spin bands; we note that the Berry curvatures are non-zero only when inversion symmetry is spontaneously broken. Using the Berry curvatures, we evaluate the orbital magnetizations and Hall conductivities of all three states. For momentum-

independent mass m the Berry curvature of the N -layer chiral model is

$$\Omega_{\hat{z}}^{(\alpha)}(\mathbf{p}, \tau_z, s_z) = -\alpha \frac{\tau_z m}{2 h_t^3} \left(\frac{\partial h_{\parallel}}{\partial p} \right)^2, \quad (4.2)$$

where symbol $\alpha = +(-)$ denotes the conduction (valence) band, and the transverse and total pseudospin fields are $h_{\parallel} = (v_0 p)^N / \gamma_1^{N-1}$ and $h_t = \sqrt{m^2 + h_{\parallel}^2}$. The orbital magnetic moment carried by a Bloch electron[8] is $m_{\hat{z}}^{(\alpha)} = e\hbar \varepsilon^{(\alpha)} \Omega_{\hat{z}}^{(\alpha)}$ for a two-band model with particle-hole symmetry. For the chiral band model

$$m_{\hat{z}}^{(\alpha)}(\mathbf{p}, \tau_z, s_z) = \left[-\tau_z \frac{m}{h_t^2} \left(\frac{\partial h_{\parallel}}{\partial p} \right)^2 m_e \right] \mu_B, \quad (4.3)$$

where m_e is the electron mass and μ_B is the Bohr magneton $e\hbar/2m_e$. Like the Berry curvature the orbital magnetization changes sign when the valley label changes *and* when the sign of the mass term (the sense of layer polarization) changes, *i.e.* both are proportional to $\tau_z \text{sgn}(m)$. The orbital magnetization is however independent of the band index α . As illustrated in Fig. 4.3, in the case of $|m| = 10$ meV, the orbital magnetic moment close to each Dirac point has a symmetric sharp peak

Table 4.1: Summary[9] of spin-valley layer polarizations (T or B) and corresponding charge, spin, and valley Hall conductivities (e^2/h units) and insulator types for the three distinct states (b-d) with no overall layer polarization, for a state in which every spin-valley is polarized toward the top layer (a), and for a state with partial layer polarization (e).

Fig.	$K \uparrow$	$K \downarrow$	$K' \uparrow$	$K' \downarrow$	$\sigma^{(\text{SH})}$	$\sigma^{(\text{VH})}$	$\sigma^{(\text{CH})}$	$\sigma^{(\text{SVH})}$	Insulator
4.1(b)	T	T	B	B	0	0	$2N$	0	QAH
4.1(c)	T	B	T	B	0	0	0	$2N$	LAF
4.1(d)	T	B	B	T	$2N$	0	0	0	QSH
4.1(a)	T	T	T	T	0	$2N$	0	0	QVH
4.1(e)	T	T	T	B	N	N	N	N	All

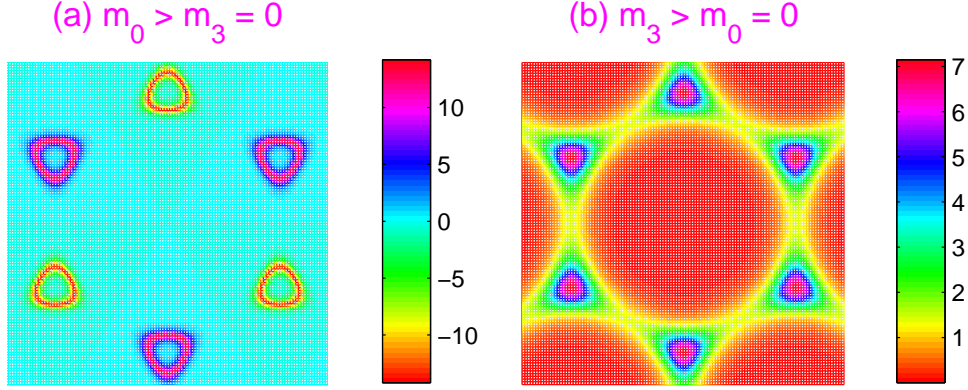


Figure 4.2: Berry curvature (an effective magnetic field in momentum space) as a function of momentum-space position in the bilayer graphene Brillouin zone[9]. (a) For a quantum valley Hall state; (b) for a quantum anomalous Hall state. Large energy gaps are chosen deliberately in order to visualize the shape of the peaks and the trigonal warping effect.

at which individual states carry moments twenty times larger than μ_B . The state in which $m \rightarrow m\tau_z$ therefore has overall orbital magnetization and broken time reversal symmetry, even though it does not have a finite spin-polarization. Integrating over the valence band, we obtain a total orbital magnetization per area $\sim (Nmm_e/2\pi\hbar^2)\ln(\gamma_1/|m|)\mu_B$, that is $\sim 0.002\mu_B$ per carbon atom for $|m| = 10$ meV.

In the presence of an in-plane electric field, an electron acquires an anomalous transverse velocity proportional to the Berry curvature, giving rise to an intrinsic Hall conductivity[8, 78]. Using Eq. (4.3), we find that the intrinsic Hall conductivity contribution from a given valley and spin is

$$\sigma_H^{(\alpha)}(\tau_z, s_z) = \frac{\tau_z Ne^2}{2h} \left(\frac{m}{h_t(p_F)} - \frac{m}{|m|} \delta_{\alpha,+} \right), \quad (4.4)$$

where $h_t(p_F)$ is the total pseudospin field at the Fermi wavevector. Provided that the Fermi level lies in the mass gap, each spin and valley contributes $Ne^2/2h$ to the

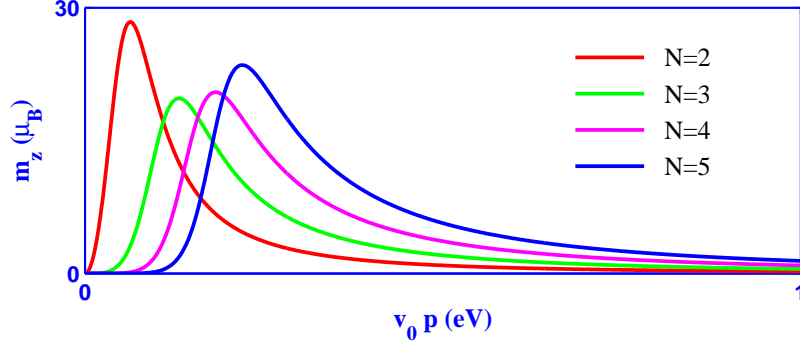


Figure 4.3: The magnitude of orbital magnetic moments carried by individual states versus in-plane momentum, for each spin and valley flavor in ABC graphene N -layers. Here the moments are in units of μ_B and $|m| = 10$ meV.

Hall conductivity, with the sign given by $\tau_z \text{sgn}(m)$.

In Fig. 4.1(a) we consider the case in which each spin-valley is polarized in the same sense. The total Hall conductivity is then zero for both spins, with the K and K' valleys making Hall conductivity and magnetization contributions of opposite sign, preserving time reversal symmetry. This phase can be viewed as having a valley Hall effect[80] and, even though it does not break time-reversal symmetry, we argue later that this designation has physical significance.

As shown in Fig. 4.1(b), the case $m\sigma_z \rightarrow m\tau_z\sigma_z$ implies Hall conductivity and orbital magnetization contributions of the same sign for each spin and valley. This state breaks time reversal symmetry but its spin density is surprisingly is everywhere zero. The total Hall conductivity has the quantized value $2Ne^2/h$. Similarly, the orbital magnetic moment has the same sign for all flavors. We refer to this state as the quantized anomalous Hall state. In addition to its anomalous Hall effect, this state has a substantial orbital magnetization. The anomalous Hall states is probably most simply identified experimentally by observing a $\nu = 2N$ QHE which persists to zero magnetic field.

For $m\sigma_z \rightarrow ms_z\sigma_z$, depicted in Fig. 4.1(c) the two spins have valley Hall effects of opposite sign, and the two layers have spin-polarizations of opposite sign. This layer-antiferromagnetic state has broken time reversal symmetry and opposite spin-polarizations on top and bottom layers.

Fig. 4.1(d) describes the third type of state with effective interaction $m\sigma_z \rightarrow m\tau_z s_z \sigma_z$. This state does not break time reversal invariance and instead has anomalous Hall effects of opposite signs in the two spin subspaces, i.e. a spin Hall effect. Neither the top nor the bottom layer has spin or valley polarization. Quite interestingly if we only consider one layer, there are both spin Hall and valley Hall effects, however, the orientations of the Hall currents in the top and the bottom layers are the same for the spin Hall effects but opposite for the valley Hall effects.

Table 4.1 includes as well the case in which one flavors polarizes in the opposite sense of the other three; charge, valley, and spin Hall effects coexist in this state which can be favored by a small potential difference between the layers.

4.1.4 Edge states

The physical significance of spontaneous charge, valley, and spin anomalous Hall effects is illustrated in Fig. 4.4. Graphene has very weak spin-orbit interactions, which in our case we ignore altogether. Fig. 4.4 compares the edge electronic structure of $N = 1, 2, 3$ spinless models with a quantized anomalous Hall effect (*i.e.* with opposite layer polarizations at two valleys) and with a quantized valley Hall effect. The states with anomalous Hall effects have N topologically protected robust chiral edge states associated with the QHE, as shown in Fig. 4.4(d)(e)(f). The edge state structure associated with the valley Hall states is more interesting. In the $N = 1$ valley Hall state the Hall conductivity contribution associated with each valley is

$1/2$ in e^2/h units; the full unit of Hall conductance requires the two valleys to act in concert. Because they act in opposition in the valley Hall state, there is no edge state, as shown in Fig. 4.4(a). For $N = 2$ on the other hand, each valley contributes a full quantum Hall effect, and as we see in Fig. 4.4(b) we find two chiral edge states with opposite chirality, one associated with each valley. For $N = 3$ depicted in Fig. 4.4(c), the additional half quantum Hall effect from each valley is insufficient to produce a new chiral edge state branch. In general we expect $[N/2]$ chiral edge state branches at each valley in an N -layer stack. Of course valley Hall edge states are topologically protected only when the edge-direction projections of K and K' valleys are not coincident and inter-valley scattering due to disorder is absent. Nevertheless, we expect robust edge states to be present in valley Hall states, as found[81] in numerical studies of valley Hall states induced by an external electric field without interactions.

4.1.5 Discussion

At the level of continuum-model mean-field theory[15], the three charge balanced states we have discussed are degenerate. In addition to breaking inversion symmetry, each breaks two of three additional symmetries; time reversal (\mathcal{T}), spin rotational invariance ($SU(2)$), and the valley Ising symmetry (\mathcal{Z}_2). The TI state preserves only \mathcal{T} , the AH phase preserves only spin-rotational invariance, and the AF state has \mathcal{Z}_2 symmetry. Both TI and AF phases break the continuous $SU(2)$ symmetry and therefore Goldstone modes emerge[20]. The actual ground state is dependent on subtle correlation and microscopic physics issues that are beyond the scope of this section. We note however that it might be possible to induce transitions between different possible states using external fields. For example, the energy of the quan-

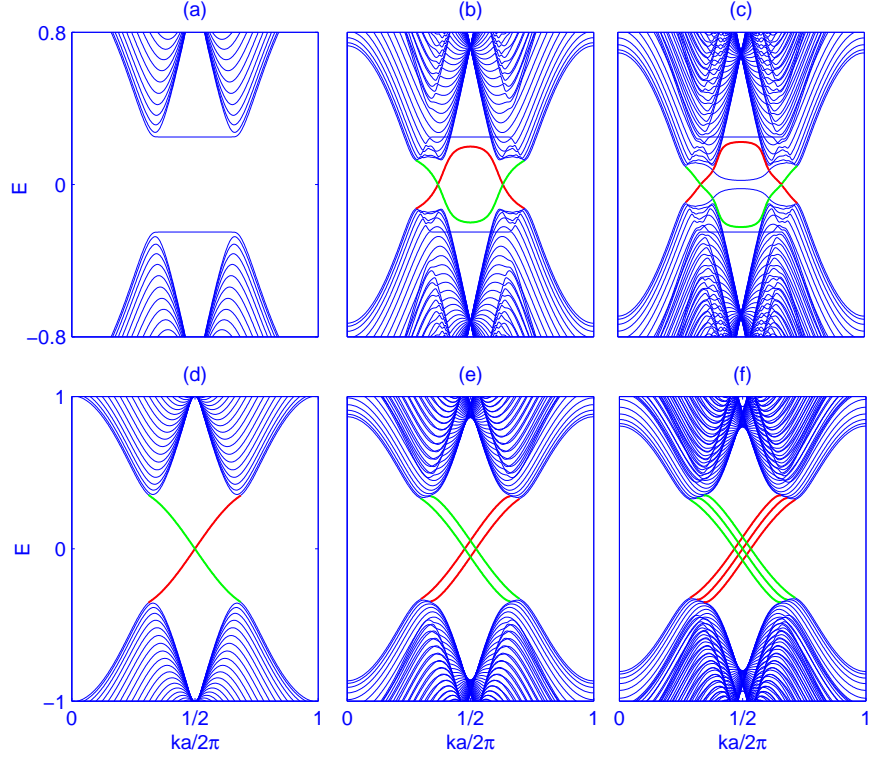


Figure 4.4: Intra-valley and inter-valley edge states in chirally-stacked graphene systems. (a)(d) for a single layer, (b)(e) for a bilayer and (c)(f) for a trilayer. To visualize the edge states, the intralayer and interlayer nearest neighbor hoppings are chosen as $\gamma_0 = 1$ and $\gamma_1 = 0.3$, respectively; $m = 0.25$ for Fig.(a,b,c) and $m = 0.3\sqrt{3}\tau_z$ for Fig.(d,e,f).

tized anomalous Hall state will be lowered by a perpendicular external magnetic field because it has a large orbital magnetization. The fully layer polarized state will be favored by an external electric field which produces a potential difference between the layers. Increasing the magnetic field further results in quantum Hall ferromagnetism[12, 64, 65]. Recent experiments[17, 76] in bilayers appear to provide definitive proof that the ground state at very weak external magnetic fields is the quantized anomalous Hall state.

The quantum spin Hall effect we discuss in this section is in several respects

different from that discussed in the well known papers[75, 79] which foreshadowed the identification of topological insulators.

- (i) The quantum spin Hall effect is driven by broken symmetries produced by electron-electron interactions, rather than by spin-orbit interactions[79] which we neglect. The effective spin-orbit coupling $m\tau_z s_z \sigma_z$ due to electron-electron interactions can be 10^4 times larger than the intrinsic one[82].
- (ii) Unlike the previous interaction induced TI phase[75] which appears only at finite interaction strengths, here the instability to the TI phase is present even for weak interactions.
- (iii) The broken symmetry occurs only for $N \geq 2$ systems which have weak repulsive interaction instabilities, rather than in the single-layer systems[75, 79] which require strong spin-orbit interactions or strong Coulomb interactions.
- (iv) Our states are also distinguished topologically, since they are characterized by Chern numbers which can have any integer value, rather than by a \mathcal{Z}_2 label. Of course, only N -odd layers are strong TI's, because the helical edge modes are likely to localize in a N -even system due to the backscattering process allowed by \mathcal{T} [83].

When Rashba spin-orbital interactions (RSOI) are strong, the spin Hall state is likely to be selected as the ground state and the Hall conductance will no longer be precisely quantized. The estimated strength of RSOI[82, 84] in most experimental systems studied to date is much smaller than the estimated spontaneous gap [21], so its influence will normally be marginal.

4.2 Deformation of edge states

4.2.1 Landau levels

In the spinless case, there are only two broken symmetry states, namely, the anomalous Hall state and the valley Hall state. In the case of a valley Hall state, valley K and K' have the same mass $m_0\sigma_z$, and each valley is layer polarized in the same sense[9]. Mass terms with the valley Hall form can be generated simply by a potential difference between the layers, so the valley Hall state is an easily generated non-interacting electron state. The total Hall conductivity of this state is zero, i.e. $\nu = 0$ for bilayer graphene, with the K and K' valleys making Hall conductivity and magnetization contributions of opposite sign, preserving time reversal symmetry. The valley Hall states can be favored experimentally by applying a perpendicular electric field[9], as shown in Fig. 4.5(a).

In the anomalous Hall state, on the other hand, one valley has a positive mass $m_3\sigma_z$ while the other has a negative mass $-m_3\sigma_z$. Correspondingly the two valleys spontaneously choose different layer polarizations[9]. Therefore the Hall conductivity and orbital magnetization contributions have the same sign for each valley[9]. This state breaks time reversal symmetry. The total Hall conductivity has the quantized value $\pm 2Ne^2/h$, i.e. $\nu = \pm 4$ in the case of bilayer graphene. In addition to its anomalous Hall effect, this state has a substantial orbital magnetization. The anomalous Hall state is probably most simply identified experimentally[17, 76] by observing a $\nu = 2N$ QHE which persists to zero magnetic field[9, 17, 20, 76], as depicted in Fig. 4.5(b).

The spectra of translationally invariant two-dimensional electron systems are quantized into Landau levels in the presence of a finite perpendicular magnetic field. In a gapless chirally stacked graphene N -layer, the zero energy Landau level

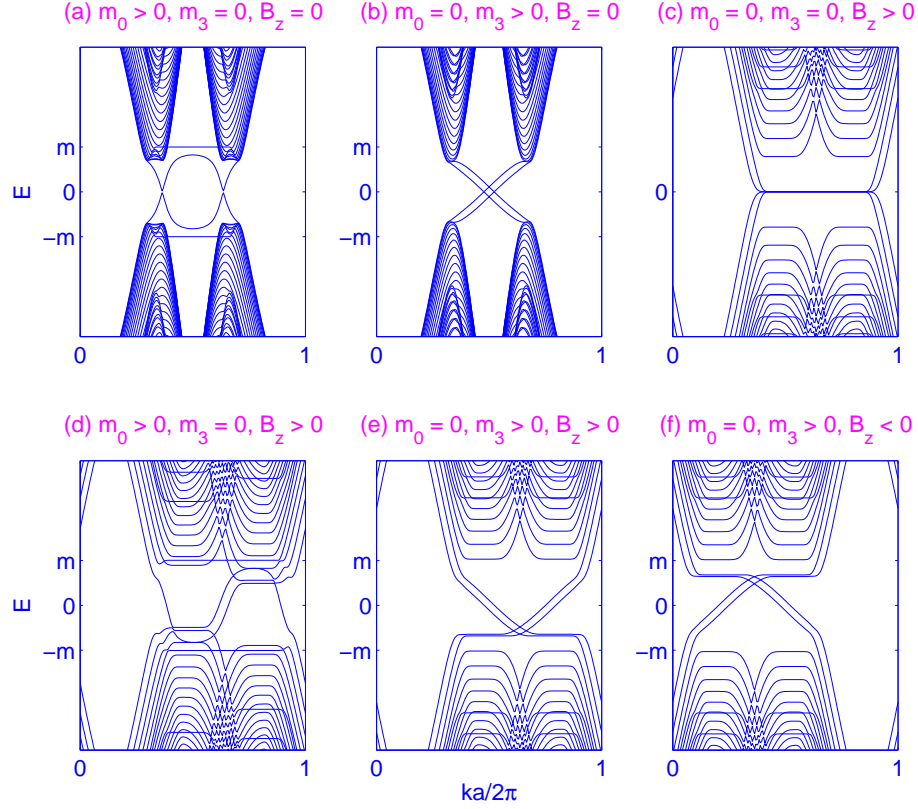


Figure 4.5: (a) Ribbon quantum valley Hall states and (b) ribbon quantum anomalous Hall states in the absence of magnetic fields; (c) Ribbon quantum Hall states for a gapless bilayer graphene; (d) $\nu = 0$ quantum Hall states for a gapped bilayer graphene in QVH phase; (e) and (f) $\nu = \pm 4$ quantum Hall states for a gapped bilayer graphene in QAH phase. To visualize the edge states, we use a zigzag ribbon, the intralayer and interlayer nearest neighbor hoppings are chosen as $\gamma_0 = 1$ and $\gamma_1 = 0.3$, respectively, and nonzero m is fixed as 0.15.

(Fig. 4.5(c)) is $4N$ fold degenerate. In the case of a valley Hall insulator, the states around K and K' valleys have very large orbital magnetic moments with opposite sign, which couple to the out-of-plane magnetic field and gives rise to the relative energy shift between valley K and K' . Consequently, the two-fold valley degeneracy is lifted and there is an asymmetry between those Landau levels around two

Dirac points, as described in Fig. 4.5(d). The energy spectrum of a quantum valley Hall insulator is adiabatically connected to that of the $\nu = 0$ quantum Hall state. In contrast, as shown in Fig. 4.5(e)(f), the valley degeneracy is unbroken in the presence of magnetic field, because the nature of the orbital magnetic moments near the two Dirac points are the same. The energy gap in a quantum anomalous Hall state is adiabatically connected to that of the $\nu = \pm 4$ quantum Hall state where the sign is a choice of whether the magnetic field is in \hat{z} or $-\hat{z}$ direction relative to m_3 .

When spin is taken into account, the quantized Landau levels of the three additional phases[9] are obtained by each spin choosing to be a quantum valley Hall state or a quantum anomalous Hall state. For the case of a quantum spin Hall state, one spin flavor is the $\nu = 2$ QAH state and the other flavor is the $\nu = -2$ QAH state. For the layer-antiferromagnetic state, each spin flavor is a $\nu = 0$ QVH state but with the opposite layer polarization to the other flavor. In contrast, one spin flavor is a QVH state while the other is a QAH state in the "All" state.

4.2.2 Electric field effects

By continuously lowering the magnetic field to zero, an anomalous Hall state is adiabatically identified[17, 76]. When a perpendicular electric field is switched on, the quantum valley Hall phase starts to compete with the quantum anomalous Hall phase. The sizes of the gap at the two valleys are $|m_0 + m_3|$ and $|m_0 - m_3|$, respectively. The state is still within the anomalous Hall phase but with two unequal gaps at K and K' for $|m_0| < |m_3|$ as seen in Fig. 4.6(a). Beyond the critical point where $|m_0| = |m_3|$ as depicted in Fig. 4.6(c), the state jumps to the valley Hall phase instead. In the quantum phase transition region as described by Fig. 4.6(b), the energy gap is enhanced at one valley while it closes at the other valley, where

quantum anomalous and valley Hall effects coexist.

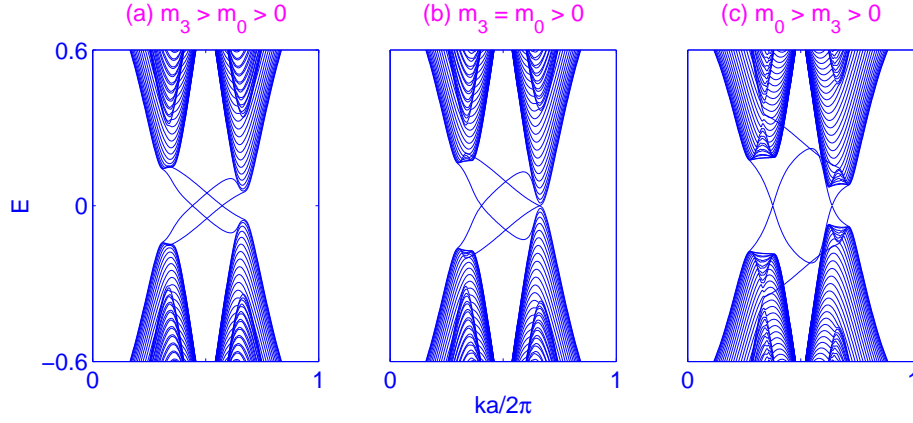


Figure 4.6: The competition between the quantum anomalous Hall state (intra-valley edge state) and the quantum valley Hall (inter-valley edge state) state in broken symmetry bilayer graphene. (a) a quantum anomalous Hall state with unequal gaps at K and K' ; (b) a critical point with an enhanced gap at K and a closed gap at K' , where quantum anomalous and valley Hall effects coexist; (c) a quantum valley Hall state with a reopened gap at K' . To visualize the edge states, we use a zigzag ribbon with the same γ_0 and γ_1 values as in Fig. 4.5.

In the quantum spin Hall state[9], the helical edge modes are likely to localize in a N -even system, due to the possible backscattering process in which N left movers and N right movers scatter into each other allowed by time reversal symmetry. Therefore, the QSH phase is topologically protected in chirally stacked odd number of graphene layers. Besides the effective spin-orbit coupling induced by interlayer interaction, Rashba interaction $\lambda_R(\tau_z\sigma_xs_y - \sigma_ys_x)$ is possibly induced by inversion symmetry breaking, and a small staggered potential $m_S\sigma_z$ is also present due to coupling to substrates. These interactions lift the degenerate zero energy to $m_{SH} \pm \lambda_S$, $-m_{SH} \pm \sqrt{4\lambda_R^2 + \lambda_S^2}$. The topological-nontrivial phase persists as long

as the effective spin-orbit gap is not closed, or in other words,

$$\left(\frac{\lambda_R}{m_{SH}}\right)^2 + \left|\frac{\lambda_S}{m_{SH}}\right| \leq 1, \quad (4.5)$$

which is independent of layer number N and determines the phase diagram. Trigonal warping and other remote hopping terms are time reversal invariant, not disfavoring the TI phase.

4.2.3 Edge states along domain walls

At zero temperature, in a clean chirally stacked few-layer graphene system, there are 16 possible broken symmetry states and they are classified as 5 distinct phases, as discussed in the section II. In the presence of disorder or thermal fluctuations, different phase are likely to appear locally in different parts of the system. There are 240 possible domain walls and they can be classified into 16 distinct types. In the spinless case, as only valley Hall phase and anomalous Hall phase are allowed, there are 2 types of intra-phase and 1 type of inter-phase domain walls. At each type of domain wall, we argue that a unique Luttinger liquid emerges; the spinless bilayer examples of which are illustrated in Fig. 4.7.

In a quantum valley Hall state, the Chern numbers[9, 74] of the two valleys are $\pm N/2$, respectively. For the case of a quantum anomalous Hall state, the Chern number[9, 74] is $N/2$ at both valleys with a uniform sign. These features are equivalently shown in Fig. 4.2. At the domain wall separating two quantum valley Hall regions with the opposite layer polarization, the Chern numbers change by $\pm N$ for a single valley and hence N parallel zero modes appear at each valley as depicted in Fig. 4.7(a). These one dimensional zero modes form N copies of full Luttinger liquids and the valley-pseudospin becomes exactly the left-or-right chi-

rality. This QVH-QVH domain walls and the generated Luttinger liquids are likely to be formed in the electron-hole puddles, and can be easily realized and tuned by an external electric field.

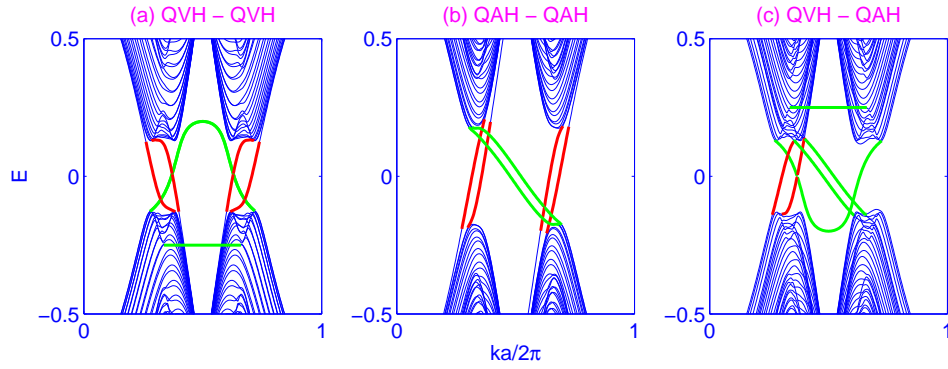


Figure 4.7: Three distinct Luttinger liquids at domain walls in spinless bilayer graphene with broken symmetry. The red lines denote the zero modes localized at domain walls between (a) two quantum valley Hall regions with opposite layer polarization; (b) two quantum anomalous Hall regions with opposite total Hall conductance; (c) a quantum valley Hall region and a quantum anomalous Hall region. The green lines represent the edge states on the outermost zigzag boundaries and note that they are doubly degenerate in (a) and (b) for the two zigzag boundaries. To visualize the edge states, we use a zigzag ribbon with the same γ_0 and γ_1 values as in Fig. 4.5 and $|m| = 0.25$.

At a domain wall separating two quantum anomalous Hall regions with opposite total Hall conductance, the change of Chern number is N (neglecting spin) for both valleys. Therefore, we expect that N parallel zero modes appear at each valley as seen in Fig. 4.7(b). Each valley has a copy of a purely chiral "spin"- $\frac{N-1}{2}$ like Luttinger liquid. At the domain wall between a quantum valley Hall and a quantum anomalous Hall region, the Chern number is changed by N for one valley while it is preserved for the other. Thus the edge states at the interface are purely chiral at one valley while they completely disappear at the other. We expect the Luttinger

liquid behaviors of the one dimensional zero modes at the spinfull domain walls are much more exotic.

4.2.4 Discussion

The trigonal warping effect is sometimes ignored in theoretical efforts to identify the broken symmetry physics based on mean field theory or renormalization group analysis. This is reasonably justified in the bilayer case for the following two reasons. (i) The trigonal warping effect dominates only below 1 meV[4], compared to relevant band broadening not much smaller than 1 meV. Trigonal warping effect are therefore likely to be smeared and become inessential, due to residue disorder and fluctuations at higher energies. (ii) The infrared cutoff of the RG flows can be reasonably set at where the quadratic band dispersion overwhelms the trigonal warping effect. For chirally stacked graphene with the layer number $N > 2$, the trigonal warping energy scale is increased by almost a factor of 10[6] while the even flatter gapless bands are much more unstable to interlayer interactions. Interaction effects are expected to dominate at low carrier densities[6] and to drive the spontaneous inversion symmetry breaking, but samples that are clean enough to reveal its interaction physics have not yet been studied. We comment that the broken symmetry is likely to occur only in low disorder and high quality samples, since large disorder can destroy the perfect nesting conditions and reduce the parameter space of the RG flows.

Recent experiments[17, 76] in bilayers appear to provide definitive proof that, at $\nu = \pm 4$, the ground state at very weak external magnetic fields is the quantized anomalous Hall state. (At $\nu = 0$, LAF state (or called SDW state) and QSH state are competing for the ground state at zero magnetic field.) Even though a

QAH state does not have a finite spin-polarization, the orbital magnetic moment close to each Dirac point has a symmetric sharp peak[9] at which individual states carry moments twenty times larger than μ_B , and a total orbital magnetization per area goes as $\sim (N\lambda m_e/2\pi\hbar^2) \ln(\gamma_1/|\lambda|)\mu_B$, that is $\sim 0.002\mu_B$ per carbon atom for $|m| = 10$ meV[9]. Thus the energy of the quantized anomalous Hall state will be lowered by a perpendicular external magnetic field. Lattice mean field theory shows the size of the gap can be as large as 30 meV[21] but the actual ground state is dependent on subtle correlation and microscopic physics issues. We estimate that a magnetic field of the order of 0.004 T is sufficient to favor the QAH state over the QVH state[21]. Increasing the magnetic field further results in quantum Hall ferromagnetism[12, 64, 65]. The fully layer polarized QVH state will be favored by an external electric field which produces a potential difference between the layers. The turning point of the band gap is approximately 7 mV/nm for a perpendicular electric field[21].

We close this discussion by pointing out that the edge states of a broken symmetry state have physical significance[9]. (i) The edge states for QAH phase are inter-valley one dimensional gapless modes while the zero modes are intra-valley like for QVH phase[9]. (ii) The states with anomalous Hall effects have N topologically protected robust chiral edge states associated with the QHE[9]. (iii) For the valley Hall effects, in general we expect $[N/2]$ chiral edge state branches at each valley in an N -layer stack[9]; the full e^2/h unit of Hall conductance requires the two valleys to act in concert; the additional half quantum Hall effect from each valley in the N -odd layers is insufficient to produce a new chiral edge state branch. This is a novel manifestation of the chiral anomaly in condensed matter systems. Of course valley Hall edge states are topologically protected only when the edge-direction projections of K and K' valleys are not coincident and inter-valley scattering due to

disorder is absent.

4.3 Distinguish spontaneous quantum Hall states in bilayer graphene

4.3.1 Introduction

Bilayer graphene[3, 4] and its thicker N -layer cousins, chirally (or ABC) stacked multilayers[5, 6, 9, 50], have attracted considerable theoretical[9, 10, 15, 20, 21, 46, 47, 69] and experimental[13, 17, 18, 68, 76] attention because of their susceptibility to broken symmetries that are accompanied by large momentum space Berry curvatures and different types of topological order. In a continuum model mean-field theory, the ground state is[15] an Ising layer-pseudospin ferromagnet in which each spin-valley flavor is[10, 15, 46] layer polarized. The quasiparticle Hamiltonian in these states develops mass gaps that change the character of the wavefunctions at small momentum and produce[9, 20] Berry curvature. The integral of Berry curvature over a suitably defined region of momentum space near a given valley is nearly exactly quantized at $\pm 2\pi$. This property can be interpreted as saying that each valley contributes $\pm e^2/h$ to the Hall conductivity with a sign that reverses with valley index and with the sense of layer polarization. States with total Hall conductivity Ie^2/h evolve smoothly into quantum Hall ferromagnets with $\nu = I$ in the presence of a perpendicular magnetic field.

When spin is ignored only two different types of states can be distinguished, ones in which the K and K' valleys are layer polarized in the opposite sense producing a quantum anomalous Hall (QAH) state[9, 20, 77] with broken time reversal (\mathcal{T}) symmetry and orbital magnetization[9], and ones in which the two valleys have

the same sense of layer polarization producing an inversion (\mathcal{I}) symmetry breaking quantum valley Hall (QVH) state[9, 20] with zero total Hall conductivity. When spin is included, there are three distinct states with no overall layer polarization as summarized in Table 4.2: i) a QAH state with Hall effect contributions of the same sign for opposite spins, ii) a quantum spin Hall (QSH) state[9, 20, 75, 79, 85, 86] with opposite QAH signs for opposite spins, and iii) a LAF state[9] that has QVH states with opposite layer polarization signs for opposite spins. Among these possibilities, lattice mean-field theory calculations[21] suggest that inter-valley exchange weakly favors QVH states in the spinless case and LAF states in the spinful case. In this section we analyze how all three states respond to Zeeman coupling to their spin and to electric-field coupling to their layer pseudospin degrees-of-freedom. We find that the Zeeman field response distinguishes QAH states from QSH and LAF states. In the LAF, the Zeeman field induces a non-collinear spin state in which the components of the spin-density perpendicular to the field are opposite in opposite layers, while those along the field direction grow smoothly with field strength and are identical. The three states respond similarly to an electric field between the layers, which can induce first order transitions at which the total layer polarization jumps.

Table 4.2: Summary[9] of spin-valley layer polarizations (t or b), broken symmetries, charge (C) and spin (S) Hall conductivities (e^2/h units) and insulator types for the three distinct states with no overall layer polarization.

$K \uparrow$	$K \downarrow$	$K' \uparrow$	$K' \downarrow$	$\sigma^{(S)}$	$\sigma^{(C)}$ (I)	Broken Symm.	Insulator
t	t	b	b	0	$2N$	T, Z_2	QAH
t	b	t	b	0	0	$T, SU(2)$	LAF
t	b	b	t	$2N$	0	$Z_2, SU(2)$	QSH

There is already some suggestive experimental evidence for spontaneous

quantum Hall states in graphene multilayers that is consistent with mass gaps $\Delta \sim 2 - 8$ meV in recent studies of suspended bilayers[13, 17, 18, 76] and trilayers[68]. Since the gaps are seen[13, 17, 68] only at temperatures well below Δ/k_B they appear to be of many-body origin. Moreover, measurements of bilayers in a perpendicular magnetic field B appear to show that both $\nu = \pm 4$ and $\nu = 0$ quantum Hall states can persist to zero-magnetic field[13, 18], implying that spontaneous quantum Hall states with total Hall conductivity quantum number $I = 0, 4$ can be stabilized by interactions at $B = 0$.

4.3.2 Continuum model mean-field theory

In single-layer graphene the band dispersion remains linear over a broad range of energy surrounding the charge neutrality point. When graphene's honeycomb layers are chirally stacked only two sublattice sites, one located in the top layer and one in the bottom layer, are not connected to near-neighbors in other layers and are therefore relevant at low energies. Hopping between these sites, *e.g.* from top (t) A to bottom (b) B , becomes an N -step process, leading to two remarkably flat bands with $\pm k^N$ dispersion and layer pseudospin chirality N [6, 9]. These unique band features are encoded in the low-energy $\mathbf{k} \cdot \mathbf{p}$ Hamiltonian given below. Because of the flat bands and the large pseudospin chirality, interactions become dominant at low energies in few-layer[6, 9] chiral graphene. In mean-field theory inversion symmetry is broken[10] within each spin and valley, leading in a contact interaction

model to the following Hamiltonian:

$$\mathcal{H}^{\text{HF}} = \sum_{\mathbf{k}\alpha\beta ss'} c_{\mathbf{k}\alpha s}^\dagger [h_0 + h_{\text{H}} + h_{\text{F}}] c_{\mathbf{k}\beta s'}, \quad (4.6a)$$

$$h_0 = \varepsilon_{\mathbf{k}} [\cos(N\phi_{\mathbf{k}}) \sigma_x^{\alpha\beta} + \sin(N\phi_{\mathbf{k}}) \sigma_y^{\alpha\beta}] \delta_{ss'}, \quad (4.6b)$$

$$h_{\text{H}} = [V_0 \Delta_0 \delta^{\alpha\beta} + V_z \Delta_z \sigma_z^{\alpha\beta}] \delta_{ss'}, \quad (4.6c)$$

$$h_{\text{F}} = -[V_0 + V_z \sigma_z^{\alpha\alpha} \sigma_z^{\beta\beta}] \Delta_{\alpha s}^{\beta s'}, \quad (4.6d)$$

where $\varepsilon_{\mathbf{k}} = (v_0 \hbar k)^N / (-\gamma_1)^{N-1}$ is the band dispersion, $V_{0,z} = (V_S \pm V_D)/2$ denotes the average (difference) of intralayer and interlayer interactions, and density matrix $\Delta_{\alpha s}^{\beta s'} = A^{-1} \sum_{\mathbf{k}} \langle c_{\mathbf{k}\beta s'}^\dagger c_{\mathbf{k}\alpha s} \rangle_{\text{f}}$ must be determined self-consistently. $\Delta_{0,z}$ is the density sum (difference) of the top and bottom layers. $\cot \phi_{\mathbf{k}} = \tau_z k_x / k_y$ and $\tau_z(\pm 1)$ labels valleys K and K' . The Pauli matrices σ act on the *which-layer* pseudospin and $s(\pm 1)$ denotes the real spin. Because of the in-plane rotational symmetry of the continuum model, it is easy to verify that this mean-field Hamiltonian does not generate Hartree (H) or Fock (F) potentials that are off-diagonal in layer index.

We seek self-consistent solutions for the $N = 2$ QAH, QSH, and LAF s -states. When Zeeman coupling is neglected the Hartree and Fock contributions to the Hamiltonian are mass terms proportional to σ_z , the four flavors decouple, and the mean-field equations are readily solved. For LAF, QSH, and QAH states the mass terms have the respective forms $-m s_z \otimes \sigma_z$, $-m \tau_z \otimes s_z \otimes \sigma_z$, and $-m \tau_z \otimes \sigma_z$ where s_z is a spin Pauli matrix, as summarized in Table 4.2. Using the constant density-of-states per flavor $\nu_0 = \gamma_1 / (4\pi \hbar^2 v_0^2)$ of the normal state, introducing an ultraviolet cutoff at the inter-layer hopping energy γ_1 , and assuming weak-coupling,

the gap equation can be solved to yield

$$m = 2\gamma_1 \exp(-2/v_0 V_S). \quad (4.7)$$

4.3.3 Influence of Zeeman field

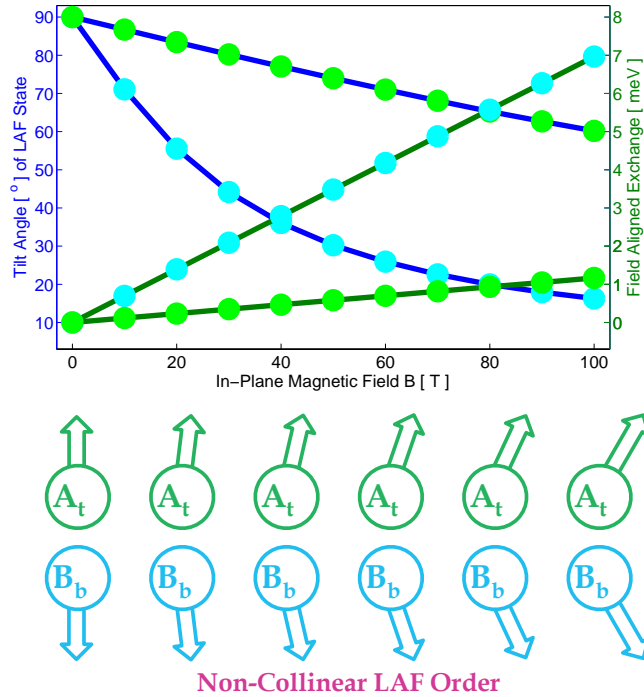


Figure 4.8: Upper panel: (Left axis) LAF tilt angle θ (green) and total effective-field tilt angle including both exchange and external field components (cyan) vs. in-plane magnetic field. (Right axis) Field aligned exchange $m \cos \theta$ (green) and total effective-field $M + m \cos \theta$ (cyan) vs. in-plane field. Lower panel: sketch of the LAF tilt angles obtained from the upper panel. We assume a 4 meV spontaneous gap at $B = 0$ throughout the section, corresponding to $v_0 V_S \sim 0.334$.

When Zeeman coupling is included, the QAH state quasiparticles simply spin-split, leaving the ground state unchanged but the charge gap reduced. For a 4 meV spontaneous gap at zero-field, corresponding to dimensionless interaction

$v_0 V_S \sim 0.334$ - close to the value expected to be appropriate for screened Coulomb interactions, a field of ~ 35 T drives the gap to zero. The QSH and LAF states, on the other hand, have more interesting non-collinear magnetic-field induced states. We apply a Zeeman field in the \hat{x} direction and allow spin-densities in the $\hat{x} - \hat{z}$ plane. In practice this amounts to keeping $\Delta_{\alpha s}^{\beta s'}$ real but allowing spin off-diagonal terms. In this case we find that for a 4 meV spontaneous gap, the LAF tilt angle θ relative to the \hat{x} direction decreases from $\pi/2$ at zero field to $\pi/3$ at 100 T. The mass terms are correspondingly spin-dependent with components in the \hat{x} and \hat{z} directions. For the LAF

$$h_Z^{\text{HF}} = h_0 - m \sin \theta s_z \otimes \sigma_z - [M + m \cos \theta] s_x \otimes \sigma_0, \quad (4.8)$$

where $2M = g\mu_B B$ denotes the Zeeman splitting and m and θ are determined by solving

$$m \sin \theta = \frac{V_S}{4A} \sum_{k,s=\pm} \frac{m \sin \theta}{E_s}, \quad (4.9)$$

$$m \cos \theta = \frac{V_S}{4A} \sum_{k,s=\pm} \frac{M + m \cos \theta + s \varepsilon_k}{E_s}, \quad (4.10)$$

with $E_{\pm} = \sqrt{(M + m \cos \theta \pm \varepsilon_k)^2 + m^2 \sin^2 \theta}$. The four quasiparticle energies are $\pm E_{\pm}$, so the gap is $2E_-$ evaluated at $\varepsilon_k = M + m \cos \theta$, *i.e.*, $2m \sin \theta$.

For weak fields the quasiparticle spins are nearly perpendicular to the Zeeman field. As the field strength is increased the quasiparticle state spin-polarizations, which are s and \mathbf{k} -dependent, all rotate toward the \hat{x} direction and the exchange field follows suit. Assuming that $\gamma_1 \gg m, M$ we find that the perpendicular LAF mass

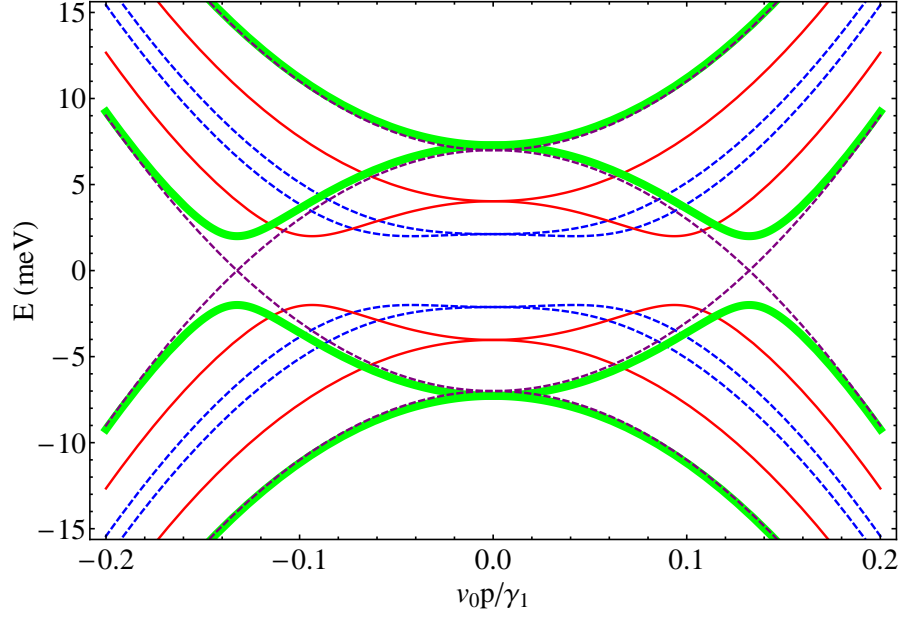


Figure 4.9: Canted LAF state quasiparticle bands for a series of in-plane magnetic field strengths: 10 T (blue), 50 T (red) and 100 T (green). The dashed purple curve for 100 T shows the quasiparticle bands when the unaligned exchange field $m \sin \theta$ is neglected.

component $m \sin \theta$ is still given by the right hand side of Eq. (4.7), and that

$$m \cos \theta = \frac{v_0 V_S}{2 - v_0 V_S} M, \quad (4.11)$$

implying that the LAF tilt angle is

$$\theta = \arctan \left[\frac{4\gamma_1 \cdot (2 - v_0 V_S)}{g\mu_B B \cdot v_0 V_S} \cdot e^{-2/(v_0 V_S)} \right]. \quad (4.12)$$

This solution was confirmed numerically and is summarized in Fig 4.8.

The gap is nearly independent of M , in clear contrast to the QAH case. As M increases the $k = 0$ quasiparticle band extrema of the LAF move to larger $k \propto \sqrt{M + m \cos \theta}$ as illustrated in Fig.4.9. For $M \gg m \sin \theta$ the non-collinear LAF state

can be viewed as an exciton condensate formed by pairing electrons in the bilayer majority spin band with holes in the minority spin band. In this limit the LAF state is therefore similar to the Zeeman-coupling induced exciton condensate considered previously in the single-layer graphene case by Aleiner *et al.*[87].

4.3.4 Influence of electric field

Because they all have σ_z layer pseudospin order, LAF, QAH, and QSH states respond similarly to an electric field perpendicular to the layers, which adds a $m_0\sigma_z$ term to the single-particle Hamiltonian. For the LAF, for example, the LAF masses $m_{\uparrow,\downarrow}$ for $m_0 = 0$ differ only by a sign. When a perpendicular electric field is applied, masses are enhanced for one spin and suppressed for the other. In our mean-field calculations first order phase transitions occur between states with distinct broken symmetries as illustrated in Fig 4.10, leading eventually to a state in which the sense of layer polarization is the same for all spin-valleys[88]. Experimental behavior in an external electric field will likely be sensitive to the pinning energies of domain walls that separate different spontaneous quantum Hall states.

When an in-plane magnetic field and a perpendicular electric field are both present, the field aligned LAF order parameter $m\cos\theta$ is little changed compared to the $E = 0$ case. The electric field dependence of $m_{\uparrow,\downarrow}$ is mainly determined by a competition between $m_0\sigma_z$ and $m\sin\theta s_z \otimes \sigma_z$. The noncollinear LAF phase is, however, strengthened by its field-aligned order-parameter component and is more robust against a perpendicular electric field when the Zeeman field is large, as illustrated in Fig 4.10. Fig 4.10 also shows that the LAF state stability can be dependent on the order in which the two fields are applied. We note that a small electric field between the layers can stabilize a state in which one flavor is

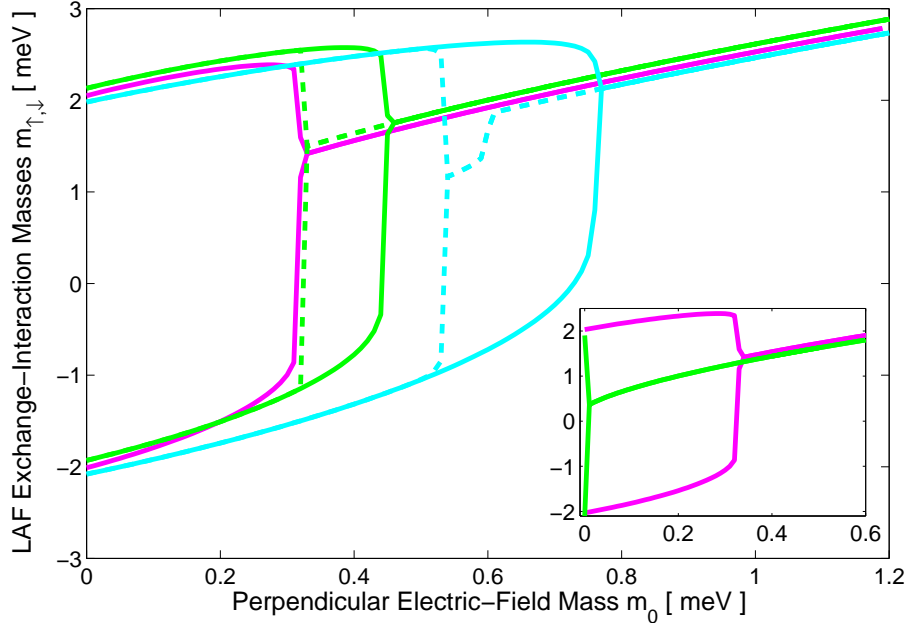


Figure 4.10: LAF exchange-interaction masses $m_{\uparrow,\downarrow}$ at parallel magnetic field $B = 0$ T (magenta), 20 T (green) and 40 T (cyan) vs. perpendicular electric-field mass m_0 . The solid and dashed curves were obtained by following the state evolution vs. electric field at fixed Zeeman field and vs. Zeeman field at fixed electric field. The inner panel indicates the LAF (magenta) and fully layer polarized (green) state stability ranges vs. electric-field mass at zero magnetic field.

polarized in a sense opposite to the other three and charge, valley, and spin Hall conductivities are all non-zero[9]. This state is not represented in Fig. 4.10 where we have assumed that the two valleys have the same layer polarization.

4.3.5 Discussion

Low-energy electrons in bilayer graphene have spin, valley, and layer two-component quantum degrees of freedom. Because it appears in the band Hamiltonian, the layer pseudospin plays a different role in bilayer graphene physics than spin or valley. Flat conduction and valence bands and Bloch states with $J = 2$ layer-pseudospin

chirality combine to make the band state unstable toward a family of insulating broken symmetry states that have independent spontaneous layer polarizations in each spin-valley component. Three distinct states have no overall layer polarization, a quantum anomalous Hall state, a quantum spin Hall state, and a layer antiferromagnet state[9]. In this Letter we have shown that the QAH state can be distinguished from the QSH and LAF states by examining the dependence of the charged quasiparticle gap on the strength of Zeeman coupling to an in-plane magnetic field. In the QAH case, the ground state is unchanged but the quasiparticle gap is reduced - vanishing when the Zeeman coupling strength is equal to the ground state gap via a mechanism reminiscent of the Clogston limit in superconductors. The QSH and LAF states respond to Zeeman fields in a more interesting way, by establishing non-collinear spin states within each valley and evolving toward an unusual kind of exciton condensate in the strong Zeeman coupling limit. The gap of QSH and LAF states is independent of Zeeman coupling strength drawing a sharp distinction with the QAH case. When combined with probes that are sensitive to edge state transport, which is topologically protected[85] in QAH and QSH cases but not in the LAF case, this property should enable any of the three states to be uniquely identified.

It appears clear that bilayer graphene is exhibiting new many-body physics. This Letter points out that experimental studies of the Zeeman energy dependence of the gap could help to distinguish between different possibilities in bilayers, and also in larger N chiral few-layer graphene. As mentioned previously some theoretical authors have concluded[47, 69] that the ground state of a neutral bilayer should be a *nematic XY*-plane layer-pseudospin ferromagnet which breaks in-plane rotational symmetry, rather than a \hat{z} -direction Ising pseudospin ferromagnet. (The z-component of the layer pseudospin density is the difference in density between

the top and bottom layers while an x- or y-component indicates interlayer coherence.) The nematic states are most strongly distinguished from the \mathcal{S} -symmetry breaking spontaneous quantum Hall states[9, 10, 15, 20, 21, 46] by the absence of a charged quasiparticle gap in the former case. In the nematic state interactions generate mean fields that are off-diagonal in layer index and reduce the symmetry of the bands, splitting the $2\pi K(K')$ Dirac points into two π -Dirac points that are displaced from $K(K')$ in an arbitrary direction. The mean-field-theory property that lower energy states are obtained with Ising compared to XY pseudospin order is related to the larger susceptibility associated with this pseudospin component. (The band eigenstates are perpendicular to the \hat{z} -direction for all \mathbf{k} , so all band states are easily rotated toward \hat{z} pseudospin polarization.) Other potential explanations for the anomalies observed to date can be sought in trigonal warping effects, which are relevant below ~ 1 meV in bilayers and have been ignored for simplicity in the present discussion, and in structural changes unintentionally induced by current annealing of suspended samples. There is however not yet a coherent explanation of how either of these might result in a gap at Dirac point. The observed gaps appears to be of many-body origin, in any event, since they appear only at temperatures that are much lower than observed gaps[13, 18, 68, 76].

Chapter 5

Broken $SU(12)$ Symmetry Quantum Hall Ferromagnets

Trilayer graphene provides a novel two-dimensional electron gas with markedly different low energy behaviors determined by its stacking order. The four spin-valley flavors and the 3π Berry's phase give rise to Hall plateaus with quantized steps of $4e^2/h$ and 12-fold degeneracy at the zeroth Landau Level. We predict that electron-electron interactions spontaneously break the $SU(12)$ symmetry and drive quantum Hall effects at all the integer fillings ν from -6 to 6 following the Hund's rules. At $\nu = 0$ of ABC trilayers, electric fields can drive phase transitions between spin- and layer(valley)-polarized states with a critical value linear in (perpendicular) magnetic field B . In ABA trilayers, we find that the Hund's rules and the $J = 1, 2$ LL crossings depend on the next-nearest layer tunnelings and the magnetic field.

5.1 Introduction

Recent experimental advances with remarkable control over single layers of bulk materials have ushered in new members of the two-dimensional electron gas (2DEG) family, such as graphene, bilayer graphene[3] and the nontrivial surfaces of topological insulators[85, 89], that have even more peculiar properties than the usual 2DEGs. Intriguingly, many of the exotic features in these new 2DEGs are related to the quantized Berry's phase gained by quasiparticles circling around the Dirac points. As in the case of semiconductor 2DEG in a perpendicular magnetic field, when disorder is weak, Coulomb interactions induce quantum Hall ferromagnetism, *i.e.*, spontaneous spin polarizations with gaps much larger than Zeeman energies[90, 91]. The additional degrees of freedom of the new members, such as layers (surfaces)[92–94], valleys[29, 30, 95] or zero energy degenerate Landau Level (LL) orbitals[4, 31], separately double the degeneracy near the Fermi energy of a neutral 2DEG and lead to novel phenomena such as exciton condensation[96, 97], canted antiferromagnetism, and valley or LL polarizations[12, 64, 65]. Trilayer graphene[6, 50], which has become experimentally feasible recently[68, 84, 98–103], offers a brand-new degree of freedom deriving from the stacking order of the layers that has far-reaching consequences at low energies.

At first glance, both ABA-stacked and ABC (or chiral)-stacked trilayers should have Hall plateaus at $\nu = \pm 4(n + 3/2)$ with 12-fold zero energy LLs in the simplest model, because of the 4 flavors in spin-valley space and because of the 3π Berry's phase[6, 50]. However, microscopic structures, low-energy physics and interacting pictures[9, 68] are strikingly distinct in graphene trilayers with different stacking orders. ABC trilayers are the next chiral generalization of monolayer and bilayer graphene. Only two sites located in the top and bottom layers remain at low

energy and in a single spin-valley the energy degeneracy at the Dirac point is thus protected by inversion symmetry[10]. Any perturbation breaking it creates an energy gap at the Dirac point and thus supports a layer-polarized state. The quantized LL energies are unique as $E_n^{(3)} \sim B^{3/2} \sqrt{n(n-1)(n-2)}$. On the other hand, the band structure of an ABA trilayer consists of a massless monolayer and a massive bilayer graphene subbands. A unbiased ABA trilayer has mirror symmetry with respect to the middle layer and an interlayer electric field only increases the band overlap instead of opening a gap. The LL spectrum can be viewed as a superposition of monolayer-like LLs $E_n^{(1)} \sim B^{1/2} \sqrt{n}$ and bilayer-like LLs $E_n^{(2)} \sim B \sqrt{n(n-1)}$ with different cyclotron frequencies, leading to the LL crossing[104, 105].

In this chapter, we first provide effective models that govern the low-energy behaviors of trilayer graphene, then predict the Hund's rules following which electron-electron interactions induce quantum Hall effects at all the duodectet integer fillings, and determine the critical electric field that drives the first order phase transition between spin- and layer(valley)-polarized states at $\nu = 0$ of ABC trilayers. We find that next-nearest layer tunnelings have pronounced influence on determining the details of Hund's rules and LL crossings in ABA trilayers while other weak hoppings are negligible.

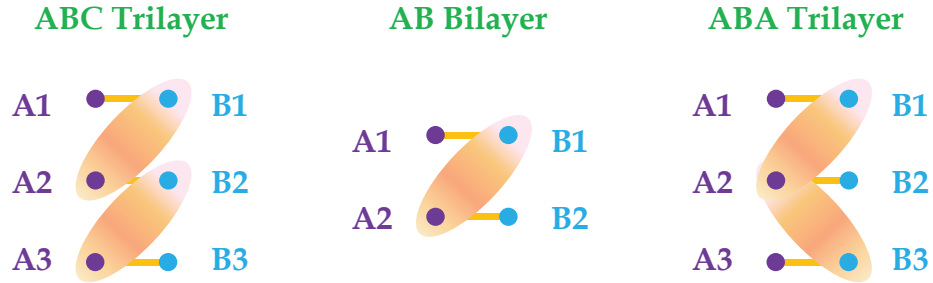


Figure 5.1: Schematic of the unit cells of few-layer graphene and the most important interlayer hoppings (γ_1).

5.2 Quantum Hall ferromagnetism in ABC trilayer graphene

When trigonal warping and Zeeman effect are neglected, in the absence of interactions the low energy properties of ABC trilayer graphene are determined by the band Hamiltonian[6, 50]

$$\begin{aligned} \mathcal{H}_{\text{ABC}} = & \frac{v_0^3}{\gamma_1^2} \begin{pmatrix} 0 & \pi^{\dagger 3} \\ \pi^3 & 0 \end{pmatrix} \\ & + u_d \left[\begin{pmatrix} 1 & 0 \\ 0 & -1 \end{pmatrix} - \frac{v_0^2}{\gamma_1^2} \begin{pmatrix} \pi^{\dagger} \pi & 0 \\ 0 & -\pi \pi^{\dagger} \end{pmatrix} \right]. \end{aligned} \quad (5.1)$$

In Eq.(5.1) the 2×2 matrices act on the low energy sites of the ABC trilayer (A_1 and B_3 in the leftmost panel of Fig. 5.1). $\pi = \hbar \mathbf{k} + e\mathbf{A}/c$ is the 2D kinetic momentum where $\pi = \tau^z \pi_x + i\pi_y$ and $\tau^z(\pm 1)$ represents valley $K(K')$. v_0 is the Fermi velocity in monolayers and $\gamma_1 \sim 0.5$ eV[6, 100] is the interlayer nearest neighbor hopping. $2u_d$ is the potential difference between the outermost layers, giving rise to an energy gap at Dirac points.

There are three zero energy eigenstates of unbiased \mathcal{H}_{ABC} in each valley, *i.e.*, $(0, \phi_{nK})$ with LL pseudospin $n = 0, 1, 2$ and $(\phi_{nK'}, 0)$ for the other valley. The dozen degenerate states follow from the direct product of LL orbital $SU(3)$ triplet, real spin $SU(2)$ doublet and *which-layer* $SU(2)$ doublet, where valley and layer pseudospins coincide. Zeeman coupling produces real spin-splitting $2E_{\text{ZM}} = g\mu_B B = 0.116 \times B[T]$ meV while u_d induces LL energy $E_{\text{LL}} = -\tau^z u_d (1 - n(\hbar\omega_3/\gamma_1)^{2/3})$ which splits LLs by distinguishing their layer and LL orbital pseudospins. $\hbar\omega_N = (\sqrt{2}v_0\hbar/\gamma_1 l_B)^N \gamma_1$ is the cyclotron frequency of quasiparticles in

chiral N -layer graphene.

The self-consistent Hartree-Fock Hamiltonian that describes the dozen zero energy states contains single-particle pseudospin splitting fields and Hartree and exchange interaction contributions:

$$\begin{aligned} \langle \alpha ns | \mathcal{H}_{ABC}^{\text{HF}} | \beta n' s' \rangle &= (E_{\text{LL}} \delta_{ss'} - E_{\text{ZM}} \sigma_{ss'}^z) \delta_{nn'} \delta_{\alpha\beta} \\ &+ E_{\text{H}} (\Delta_{\text{B}} - \Delta_{\text{T}}) \tau_{\alpha\beta}^z \delta_{ss'} \delta_{nn'} \\ &- E_{\text{F}} \sum_{n_1 n_2} X_{nn_2, n_1 n'}^{\alpha\beta} \Delta_{\alpha n_2 s}^{\beta n_1 s'} \delta_{ss'}, \end{aligned} \quad (5.2)$$

where we have used the notation $n = 0, 1, 2$ to denote LL orbitals, index s and Pauli matrix σ^z act on spin space, and $\alpha, \beta = B(K)$ or $T(K')$ are layer(valley) indices. $E_{\text{F}} = e^2 / \epsilon l_{\text{B}}$ is the strength of exchange interactions and the Hartree field $E_{\text{H}} = (2d / 2l_{\text{B}}) E_{\text{F}}$ captures the electrostatic capacitance between the top and bottom layers, where $l_{\text{B}} = 25.6 \text{ nm} (\sqrt{B[\text{T}]})^{-1}$ is the magnetic length. $d = 0.335 \text{ nm}$ is the separation between adjacent graphene layers. $\Delta_{\alpha} = \sum_{ns} \Delta_{\alpha ns}^{\alpha ns}$ where the density matrix $\Delta_{\alpha ns}^{\beta n' s'} = \langle c_{\beta n' s'}^{\dagger} c_{\alpha ns} \rangle$ must be determined self-consistently by occupying the lowest $\nu + 6$ eigenstates of $\mathcal{H}_{ABC}^{\text{HF}}$. The exchange integrals $X_{nn_2, n_1 n'}^{\alpha\beta}$ capture fermion quantum statistics and are defined as

$$X_{nn_2, n_1 n'}^{\alpha\beta} = \int \frac{d^2 \mathbf{k}}{(2\pi)^2} F_{nn_2}(-\mathbf{k}) F_{n_1 n'}(\mathbf{k}) \frac{2\pi e^2}{\epsilon k} \frac{\eta^{\alpha\beta}}{E_{\text{F}}}, \quad (5.3)$$

where $\eta^{\alpha\beta}$ becomes 1 for $\alpha = \beta$ and e^{-2kd} for $\alpha \neq \beta$. $F_{nn'}(\mathbf{k})$ are the LL Form factors in terms of associated Laguerre polynomials that capture the spatial profile of the LL wavefunctions.

The self-consistent solution of the Hartree-Fock theory for balanced ABC trilayers is summarized in Fig.5.2 using $B = 20 \text{ T}$. The gaps typically much larger

than E_{ZM} justify our weak-coupling theory. The duodectet fillings, proceeding in integer increments starting from filling factor $\nu = -6$ to 6, follows the Hund's rule behavior: first maximize the spin polarization; then maximize layer (valley) polarization to the greatest extent possible; and finally maximize the Landau Level polarization to the extent allowed by the first two rules. The states with spins along the field direction (say spin \uparrow) have lower energies than the spin down states via the Coulomb exchange enhanced spin splitting. For balanced ABC trilayers, the layer symmetric states (S) are filled before the layer antisymmetric states (AS). The three distinct Landau Level orbitals are filled in smaller n first order if the other two quantum numbers are exactly the same. Therefore, the first six filled LLs are $|S, 0 \uparrow\rangle$, $|S, 1 \uparrow\rangle$ and $|S, 2 \uparrow\rangle$ followed by the AS counterparts; the next six filled LLs are the spin \downarrow states in the same order.

The Hund's rules imply that the interaction driven integer quantum Hall s-states are spin and pseudospin polarized at $\nu = -5$ to 5, as depicted in Fig.5.2. All these 11 states are spin \uparrow polarized ferromagnets with a maximum at $\nu = 0$ driven by the exchange enhanced spin splitting. Provided by the LL dependence of the microscopic Hamiltonian, $n = 0$ LL pseudospin is polarized except at filling factors that are multiples of 3 while $n = 1$ is polarized only at $\nu = \pm 1$ and ± 4 . LL prefers to occupy both layers simultaneously in absence of interlayer bias, giving rise to XY type layer polarization with spontaneous interlayer coherence. XY phase breaks in-plane rotational symmetry and takes the advantage of no Hartree energy cost while Ising polarization breaks inversion symmetry and gains more exchange due to its intralayer character. Both the Hartree energy and the difference between intralayer and interlayer exchanges are the same order $\sim d/l_B \cdot e^2/l_B$, and it turns out that Hartree energy slightly dominates over exchange difference, leading to a XY layer-ferromagnet when $u_d = 0$.

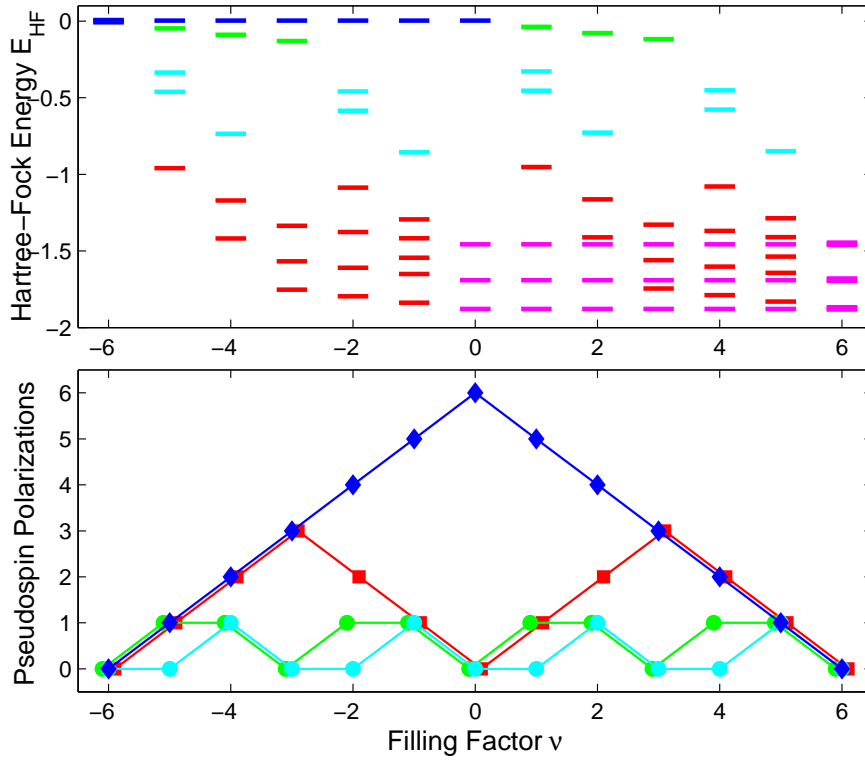


Figure 5.2: Upper panel: filling factor dependence of the Hartree-Fock energies of occupied and unoccupied LLs for a balanced ABC trilayer at 20 T. Energies are in units of $(\pi/2)^{1/2}e^2/\epsilon l_B$. Unoccupied LLs are sextets (blue), triplets (green), or singlets (cyan); occupied LLs are doublets (magenta) or singlets (red); LLs at $\nu = \pm 6$ have an extra double degeneracy due to Zeeman splitting. Lower panel: filling factor dependence of the polarizations of up spin (blue), symmetric layer (red), $n = 0$ and 1 LL orbitals (green and cyan). LL polarizations are relative to the $n = 2$ orbital.

Duodectet quantum Hall ferromagnets have fascinating dependence on the interlayer electric field. A very small potential difference between the top and bottom layers is sufficient to change the character of the layer(valley) polarization from the XY spontaneous-coherence form to an Ising polarization form in which one layer is occupied before the other. If the induced potential difference between the top and bottom layers becomes dominant over the exchange induced spin splitting be-

tween the highest occupied spin up and the lowest unoccupied spin down LLs at filling factor $\nu = 0$, there is a quantum phase transition from the spin polarized ferromagnet state into the layer(valley) polarized state. For instance, at $B = 20\text{T}$ ($\varepsilon = 1$) the layer polarized state has the lowest energy if the potential difference between the top and bottom layers exceeds 0.2eV . The gap between the highest occupied LL $|T, 2, \uparrow\rangle$ and the lowest unoccupied LL $|B, 0, \downarrow\rangle$ is 0.46eV for zero bias and is reduced to only 0.28eV near the critical point. We find that the critical electric field for this first order phase transition is $15\text{ mV}/(\text{nm}\cdot\text{T})$, comparable to the experimental value in bilayers[13, 17, 88, 106]. The linear dependence of the critical field on B follows from the fact that both bias supported energies E_H and E_{LL} are linear functions of B .

In high mobility and low disorder suspended samples, we anticipate that the states at $\nu = \pm 6, 0$ persist down to zero magnetic field exhibiting spontaneous quantum Hall effects[9], because the chiral trilayers are susceptible to broken symmetries that are accompanied by large momentum space Berry curvatures and different types of topological order. Remote weaker hoppings in ABC trilayers that have been ignored so far mainly result in trigonal warping effect at energy scale $\sim 7\text{ meV}$ [6]. This effect is likely to be washed out by exchange $E_F \sim 56\sqrt{B[\text{T}]}/\varepsilon\text{ meV}$, if not smeared by disorder.

5.3 Quantum Hall ferromagnetism in ABA trilayer graphene

Unlike ABC trilayer quasiparticles with pure chirality, the band structure of an ABA trilayer consists of a massless monolayer ($J = 1$) and a massive bilayer ($J = 2$)

subbands. Unbiased ABA trilayers have mirror symmetry respect to the middle layer and their low energy physics is governed by[104]

$$\begin{aligned} \mathcal{H}_{\text{ABA}} = & \left[v_0 \begin{pmatrix} 0 & \pi^\dagger \\ \pi & 0 \end{pmatrix} + \begin{pmatrix} -\frac{\gamma_2}{2} & 0 \\ 0 & \delta' - \frac{\gamma_5}{2} \end{pmatrix} \right]_{J=1} \\ \oplus & \left[\frac{-v_0^2}{\sqrt{2}\gamma_1} \begin{pmatrix} 0 & \pi^{\dagger 2} \\ \pi^2 & 0 \end{pmatrix} + \begin{pmatrix} \frac{\gamma_2}{2} & 0 \\ 0 & 0 \end{pmatrix} \right]_{J=2}, \end{aligned} \quad (5.4)$$

where the $J = 1$ subbands are layer antisymmetric states $|A_1\rangle - |A_3\rangle$ and $|B_1\rangle - |B_3\rangle$ while the $J = 2$ subbands are layer symmetric states $|A_1\rangle + |A_3\rangle$ and $|B_2\rangle$ with γ_1 enhanced by a factor of $\sqrt{2}$. Clearly, the mirror symmetry leads to layer coherence with XY form even in the single-particle level. The next-nearest layer tunnelings[104], *i.e.*, $\gamma_2 = -20$ meV, $\gamma_5 = 40$ meV and $\delta' = 50$ meV, lead to a band gap for each chiral branch separately but no direct gap overall. In the presence of a magnetic field, valley and linearly combined sublattices coincide, and the self-consistent Hartree-Fock Hamiltonian that describes the broken symmetry zero-energy duodecet states is

$$\begin{aligned} \langle in_i s | \mathcal{H}_{\text{ABA}}^{\text{HF}} | j n_j s' \rangle = & (E'_{\text{LL}} \delta_{ss'} - E_{\text{ZM}} \sigma_{ss'}^z) \delta_{n_i n_j} \delta_{ij} \\ & + \frac{E_{\text{H}}}{2} \Delta_{\text{B}_2} (2\delta_{\text{B}_2, i} - 1) \delta_{ss'} \delta_{n_i n_j} \delta_{ij} \\ & - E_{\text{F}} \sum_{n_1 n_2} X_{n_1 n_2}^{ij} \Delta_{i n_2 s}^{j n_1 s'} \delta_{ss'}, \end{aligned} \quad (5.5)$$

where LL index n_i depends on its atomic orbital i , *i.e.*, $n = 0$ only for $J = 1$ branch while $n = 0, 1$ for $J = 2$ branch. Exchange integrals X^{ij} is still defined by Eq.(5.3) but with a more general definition $\eta^{ij} = \sum_m c_m V_m / V_0$, where $V_{0,1,2}$ respectively denote intralayer, nearest interlayer, and next-nearest interlayer interactions in mo-

momentum space, and c_m is obtained from the interaction matrix element decomposition $\langle ij|V|ij\rangle = \sum_m c_m V_m$. Otherwise the notation in Eq.(5.5) is the same as in the ABC case. Since we focus on the balanced case with $u_d = 0$, E_{LL} is absent and replaced by E'_{LL} which is the diagonal elements in Eq.(5.4) from next-nearest layer couplings.

We find that the duodectet fillings follow the same Hund's rule behavior

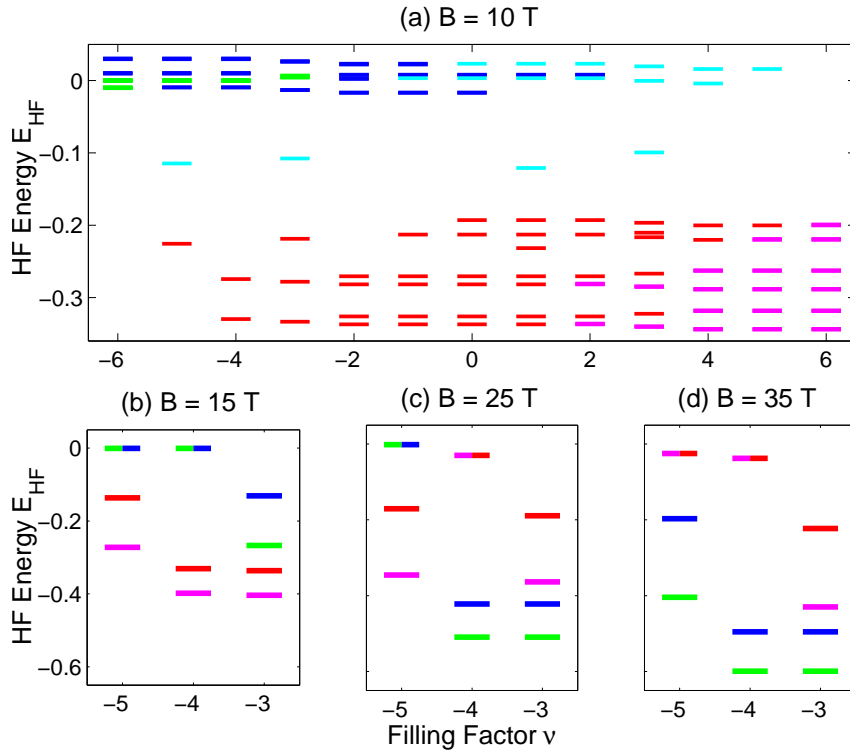


Figure 5.3: (a) Filling factor dependence of the Hartree-Fock (HF) energies (eV) of occupied and unoccupied LLs for a balanced ABA trilayer at 10 T. Unoccupied LLs are quartets (green), doublets (blue), or singlets (cyan); occupied LLs are doublets (magenta) or singlets (red). (b)-(d) Field dependence of the HF energies (eV) of the lowest four LLs at $\nu = -5, -4$ and -3 . We use 15 T in (b), 25 T in (c) and 35 T in (d). Magenta and red respectively denote the $n = 0$ and 1 orbitals of LL $|A_1 + A_3 \uparrow\rangle$; green and blue respectively denote the $n = 0$ and 1 orbitals of LL $|B_2 \uparrow\rangle$. Zeeman splitting is small enough to ignore and we assume $\epsilon = 1$.

as the ABC case while influenced significantly by next-nearest layer tunnelings. This Hund's rule prefers symmetric layer polarization so the $J = 2$ LLs are filled first. When the magnetic field is smaller than $B_{c1} = 17$ T ($\epsilon = 1$ hereafter), the first six filled LLs are $|A_1 + A_3 \uparrow\rangle$ with $n = 0$ and 1, then $|B_2 \uparrow\rangle$ with $n = 0$ and 1, and lastly $|A_1 - A_3 \uparrow\rangle$ and $|B_1 - B_3 \uparrow\rangle$ with $n = 0$. The next six filled LLs are the spin \downarrow states following the same order. The above pictures are summarized in Fig.5.3(a). At $\nu = -5$ and -4 $|A_1 + A_3 \uparrow\rangle$ LLs would be occupied first, taking advantage of gaining exchange, avoiding Hartree energy cost and being favored by E'_{LL} . At $\nu = -3$ $|B_2 0, \uparrow\rangle$ LL is then occupied, which lowers the total energy by gaining intralayer exchange and negative Hartree energy cost, and also being favored by E'_{LL} . There is a $SU(2)$ symmetry in the highest occupied LL between the $J = 1$ spin \uparrow LLs at $\nu = -1$. It is the single-particle term E'_{LL} , originated from the next-nearest layer tunnelings, that makes $|A_1 - A_3 \uparrow\rangle$ more favorable. We note that similar symmetries emerge at $\nu = \pm 1$ and ± 5 and are lifted by E'_{LL} which is independent of spin, LL orbital n and magnetic field.

While the Hund's rule behaviors at $\nu > -3$ are universal, the filling of LLs at $\nu = -5, -4$ and -3 becomes rather field dependent, as indicated in Fig.5.3. As the field strength becomes larger than B_{c1} , at $\nu = -4$, the pair of LLs $|B_2 \uparrow\rangle$ are filled before the other pair $|A_1 + A_3 \uparrow\rangle$. This results from that Coulomb physics overwhelms the next-nearest layer tunneling effects, and that intralayer exchange dominates interlayer exchange and Hartree energy cost. Furthermore, when the field is turned up to $B_{c2} = 33$ T, at $\nu = -5$ LL $|B_2 0 \uparrow\rangle$ instead of $|A_1 + A_3 0 \uparrow\rangle$ would be filled first. The two critical fields are roughly determined by $E_H/2 \sim \Delta E'_{LL}$, since the difference between intralayer and interlayer exchanges ($\sim E_H$) competes with the combination of Hartree energy $E_H/2$ and single-particle LL energy difference $\Delta E'_{LL}$. The solution is in agreement with the self-consistent numerical results (B_{c1}

and B_{c2}).

Unlike in ABC trilayers where only $J = 3$ bands are present at low energies, both $J = 1$ and 2 subbands appear at all energies in ABA trilayers, leading to LL crossing[99, 104, 105] between the two chiral branches when $\omega_1/\omega_2 = \sqrt{n_2(n_2 - 1)/2n_1}$ is satisfied. We anticipate Coulomb physics would open gaps at LL crossing points, whose characteristics would depend on the orbital indices of the crossing LLs. The measurement of Shubnikov-de Hass oscillations is able to probe the chirality of different subbands and the LL crossing effect, in which the coexistence of two 4-fold LLs doubles the degeneracy and increases the density-of-state peaks. Because of the LL crossing, the sequence of the plateaus in ABA trilayers highly depend on the magnetic field strength.

We stress here that for ABA trilayers, it is important to include next-nearest layer couplings since these tunnelings play an essential role in determining the ABA Hund's rule and the LL crossings. In contrast, the effective trigonal warping in the $J = 2$ subbands is relevant below ~ 1 meV and can be fairly ignored in the presence of disorders and interactions.

Chapter 6

Conclusion

6.1 Experimental observations

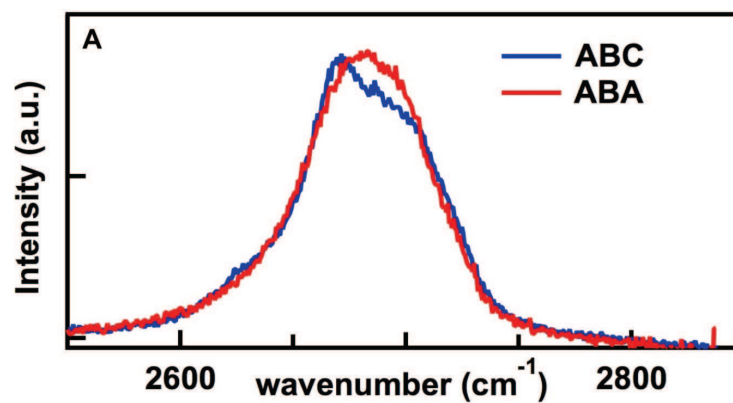


Figure 6.1: Raman spectroscopy of two trilayer graphene devices with ABA and ABC stacking orders respectively[68].

After electrical measurements, graphene devices are identified using Raman spectroscopy to be bilayer, ABA-stacked or ABC-stacked trilayer graphene[68]. As shown in Fig.6.1, the 2D peak of an ABC trilayer is more asymmetric with a

pronounced shoulder, compared to that of the ABA counterpart. This experimental advance opens the door to discover a large family of different graphene 2DES's, by identifying their layer numbers and their stacking orders as well. The electric field induced gap opening[6, 50] in trilayers have started to be observed in optical experiments[103] recently.

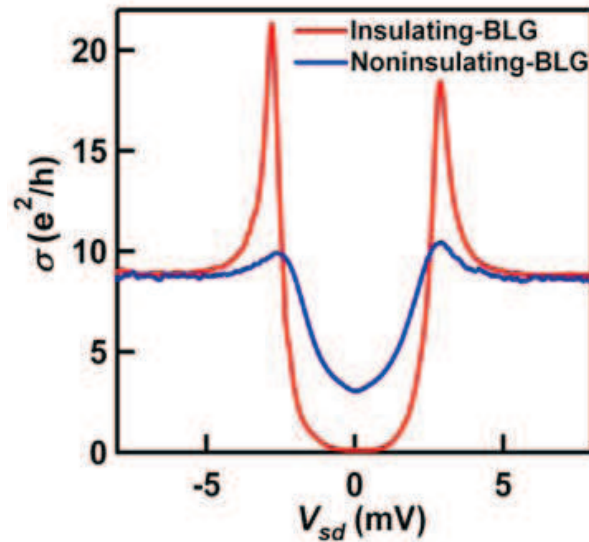


Figure 6.2: The observed spontaneous gap in suspended bilayer graphene[13].

Recent experiments[13, 17, 18, 76] have provided convincing evidence of strong electronic correlations near the charge neutrality point in bilayer graphene, although the presence of gaps is difficult to establish. The first direct spectroscopic measurements[13] in ultra-clean double-gated bilayer graphene, has resolved a gap of $\sim 2 - 3$ meV at charge neutral point using source-drain bias as the spectroscopic tool. This anomalous insulating broken symmetry state is clearly shown in Fig.6.2 with double peaks. This unique feature bears a striking resemblance to the BCS superconducting density of states and strongly suggests the formation of an ordered phase with an energy gap. Importantly, this gap can be closed by appli-

cation of $E_{\perp} \sim 13$ mV/nm of either polarity, as shown in Fig.6.3(a). Conductance G increases with small E_{\perp} ; upon application of moderate $E_{\perp} \simeq 13$ mV/nm, the BCS-like structure completely vanishes and the conductance reaches a finite minimum of $\sim 100 \mu\text{S}$ at zero carrier density. Eventually, for sufficiently large E_{\perp} , G starts to decrease with increasing fields, reverting to the well known single-particle behavior. The absence of edge states is the most unambiguous experimental signature, since the two-terminal conductivity is as low as $0.02e^2/\hbar$. It is judged that

(a) Finite E reduces spontaneous gap (b) Spontaneous gap increases with B

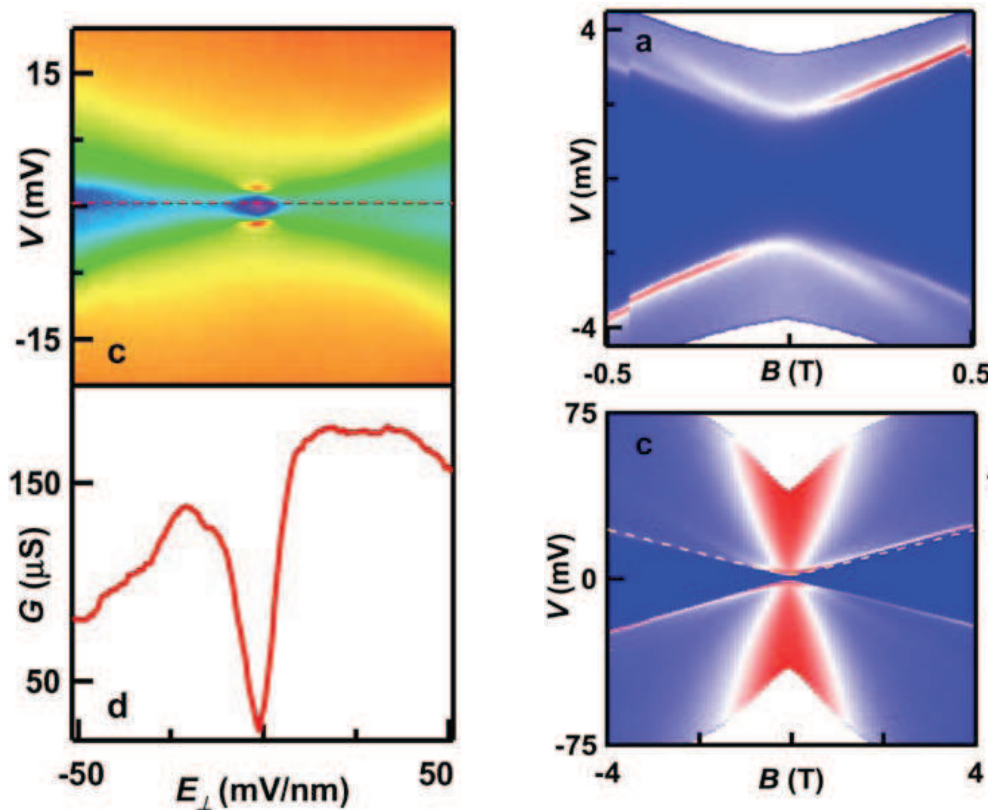


Figure 6.3: The influence of electric fields and magnetic fields on the spontaneous gap of suspended bilayer graphene[13].

among the proposed states[9], the observations are most consistent with a layer-antiferromagnet state (LAF). LAF state that breaks inversion symmetry and time reversal symmetry. Fig.6.3(b) shows that this LAF state continuously evolves to the $\nu = 0$ quantum Hall state with a gap that increases monotonically with a magnetic field. Further experiments might demonstrate the existence of non-collinear LAF order at finite magnetic field, *i.e.* LAF state at zero field is smoothly connected to the $\nu = 0$ quantum Hall ferromagnet state at infinite field. Although it is difficult to explain the particle-hole asymmetry in the experiment data, this experiment provides the first mapping of the ground states in ultra-clean bilayer graphene.

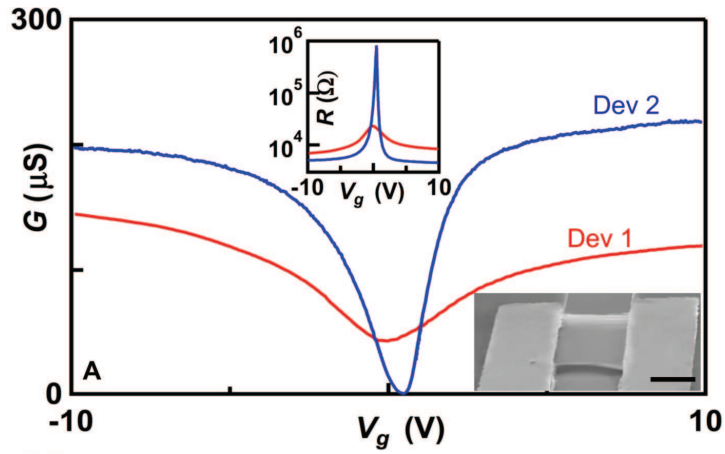


Figure 6.4: The observed spontaneous gap in suspended ABC trilayer graphene[68].

As the spontaneous inversion symmetry breaking and the resultant energy gap have been predicted in all the chiral graphene 2DES's with layer number $N \geq 2$ [9, 10], the experiments have also investigated the thicker cousin of bilayer graphene—ABC (chiral) trilayer graphene. Fig.6.4 displays the two-terminal conductance of two different suspended trilayers devices, the red one (device 1) with ABA stacking and the blue (device 2) with ABC stacking, as a function of back gate

voltage V_g at $T = 1.5$ K. Both curves are V-shaped, characteristic of high mobility samples. Interestingly, the two devices display drastically different minimum conductance G_{\min} at the charge neutrality point. G_{\min} is $\sim 50 \mu\text{S}$ for the ABA trilayer but is close to zero for ABC trilayer. This striking contrast in minimum conductivity, which differs by several orders of magnitude, not only labels the stacking orders of high mobility trilayer graphene samples, but also first time discovered[68] the predicted[9, 10] insulating broken symmetry state in ABC (or chiral) stacked trilayer graphene.

6.2 Future directions

The prediction[9] of spontaneous quantum Hall states and the observation[13, 19] of insulating broken symmetry states are just the starting of fascinating physics in few-layer graphene 2DES's, we close this thesis by pointing out some potential future directions that interest both theorists and experimentalists in condensed matter physics.

- (i) Apparently, electric or magnetic fields, carrier densities, temperatures and disorders are all able to drive phase transitions[19] between different spontaneous quantum Hall states. Some of these transitions have been observed to date, but more are waiting to be explored! Particularly, the phase diagram for $\nu = 0$ state in bilayer graphene is expected to be very rich. A perpendicular electric field drives the antiferromagnet state at zero magnetic field or the ferromagnet state at high magnetic field to a layer polarized state. At small magnetic field, antiferromagnet state is driven to quantum anomalous Hall state when the system deviates from charge neutrality. At charge neutrality, as the perpendicular magnetic increases, the non-collinear layer-antiferromagnet

ground state smoothly evolves[25] into the quantum Hall ferromagnet state with spins rotating to align with the field. On the other hand, in the presence of parallel magnetic field[16], the non-collinear layer-antiferromagnet state can be viewed as an Zeeman-coupling induced exciton condensate formed by pairing electrons in the bilayer majority spin band with holes in the minority spin band.

- (ii) Topological order usually has protected edge or surface states against weak disorders or interactions. For the five predicted spontaneous quantum Hall states, only quantum anomalous Hall and quantum spin Hall states are in company with topologically protected edge states along the boundaries while the others' edge states are only robust for zigzag terminations. However, along a domain wall or an interface[22] that separates different spontaneous quantum Hall states, novel one-dimensional solitonic zero modes do appear and the number of the modes are related to the change of bulk topological properties. It's also intriguing to study the pinning energy of the domain walls, and how a domain wall moves under external perturbations, since the energy differences between different spontaneous quantum Hall states are only $\sim 1\%$ of their condensate energies[21].
- (iii) Spontaneous quantum Hall states are predicted to occur in chiral graphene with more than one layers[9]. So it would be useful to investigate whether the layer number has an influence on the character of the ground states, how the critical temperature changes with the film thickness, and in what conditions chiral trilayer graphene is a two-dimensional topological insulator. Quantum spin Hall effect has been proposed in monolayer graphene as a topologically nontrivial consequence of the intrinsic spin-orbital interaction, preserving and

protected by the time-reversal symmetry. Unfortunately, this quite fascinating phase is not likely to emerge in graphene since the spin-orbital interactions have been proved to be smaller than 10^{-3} meV, namely, the critical temperature is below 10^{-2} K even in the clean graphene. However, this effect might be realized in chiral odd-few-layer graphene[9] via spontaneously symmetry breaking physics, as quantum spin Hall state is one of the candidate ground states.

- (iv) One of the essential reason we use current annealing when preparing the suspended bilayer graphene devices is that the broken symmetry physics in charge neutral bilayers is very fragile if disorder is present. From theoretical calculations and also experimental observations, the minimum conductivity in bilayers has a quite universal value $\sim 3e^2/\hbar$ in both suspended and substrate-supported bilayer graphene, as an influence of charge impurities. It turns out that this minimum conductivity can be strongly reduced to $\sim 0.02e^2/\hbar$ after current annealing[13]. It is highly desired to know the influence of magnetic disorder and the interplay between broken symmetry physics and charge disorder[19].
- (v) Each graphene few-layer is a unique 2DES depending on its stacking order and layer number. This fact opens the door for studying 2DES's with different chiral quasiparticles. It's very interesting to study the tunneling behaviors between different chiral 2DES's or to study the subtle correlations between different chiral quasiparticles in different sub-bands of a few-layer with a pure stacking order. One example of the latter is the ABA-stacked trilayer where monolayer-like and bilayer-like sub-bands coexist at low energies. It is also likely to have a stacking disorder[24], a new type of topological disorder, in

mechanically exfoliated multilayer graphene samples, *i.e.* grain boundaries or lattice mismatching lines separate regions with different stacking orders. Topologically protected edge (interface) states are expected to emerge, supported by external fields or even by electron-electron interactions.

Few-layer graphene systems are unique 2DES's and have more surprises in store for us to discover.

Bibliography

- [1] K. Novoselov, A. Geim, S. Morozov, D. Jiang, Y. Zhang, S. Dubonos, I. Grigorieva, and A. Firsov, *Science* **306**, 666 (2004).
- [2] A. Geim and A. MacDonald, *Physics Today* **60**, 35 (2007).
- [3] A. Neto, F. Guinea, N. Peres, K. Novoselov, and A. Geim, *Reviews of Modern Physics* **81**, 109 (2009).
- [4] E. McCann and V. Falko, *Physical Review Letters* **96**, 86805 (2006).
- [5] H. Min and A. MacDonald, *Physical Review B* **77**, 155416 (2008).
- [6] F. Zhang, B. Sahu, H. Min, and A. MacDonald, *Physical Review B* **82**, 035409 (2010).
- [7] F. Guinea, A. Neto, and N. Peres, *Physical Review B* **73**, 245426 (2006).
- [8] D. Xiao, M. Chang, and Q. Niu, *Reviews of Modern Physics* **82**, 1959 (2010).
- [9] F. Zhang, J. Jung, G. Fiete, Q. Niu, and A. MacDonald, *Physical Review Letters* **106**, 156801 (2011).

- [10] F. Zhang, H. Min, M. Polini, and A. MacDonald, *Physical Review B* **81**, 041402 (2010).
- [11] F. Zhang, D. Tilahun, and A. MacDonald, Unpublished (2011).
- [12] B. Feldman, J. Martin, and A. Yacoby, *Nature Physics* **5**, 889 (2009).
- [13] J. Velasco Jr, L. Jing, W. Bao, Y. Lee, P. Kratz, V. Aji, M. Bockrath, C. Lau, C. Varma, R. Stillwell, D. Smirnov, F. Zhang, J. Jung, and A. MacDonald, Arxiv preprint arXiv:1108.1609 (2011).
- [14] A. MacDonald, J. Jung, and F. Zhang, Invited Paper for Proceedings of the Nobel Symposium on Graphene (2011).
- [15] H. Min, G. Borghi, M. Polini, and A. MacDonald, *Physical Review B* **77**, 041407 (2008).
- [16] F. Zhang and A. MacDonald, Arxiv preprint arXiv:1107.4727 (2011).
- [17] R. Weitz, M. Allen, B. Feldman, J. Martin, and A. Yacoby, *Science* **330**, 812 (2010).
- [18] F. Freitag, J. Trbovic, M. Weiss, and C. Schönenberger, Arxiv preprint arXiv:1104.3816 (2011).
- [19] W. Bao, J. Velasco Jr, F. Zhang, L. Jing, B. Standley, D. Smirnov, A. MacDonald, M. Bockrath, and C. Lau, Unpublished (2011).
- [20] R. Nandkishore and L. Levitov, *Physical Review B* **82**, 115124 (2010).
- [21] J. Jung, F. Zhang, and A. MacDonald, *Physical Review B* **83**, 115408 (2011).
- [22] F. Zhang, J. Jung, and A. MacDonald, *Journal of Physics* (invited) (2011).

- [23] J. Jung, F. Zhang, Z. Qiao, and A. MacDonald, Arxiv preprint arXiv:1105.3666 (to appear in Physical Review B) (2011).
- [24] F. Zhang and A. MacDonald, Unpublished (2011).
- [25] F. Zhang, D. Tilahun, and A. MacDonald, Unpublished (2011).
- [26] T. Ando, Journal of the Physical Society of Japan **74**, 777 (2005).
- [27] A. Geim and K. Novoselov, Nature materials **6**, 183 (2007).
- [28] Y. Barlas, T. Pereg-Barnea, M. Polini, R. Asgari, and A. MacDonald, Physical Review Letters **98**, 236601 (2007).
- [29] K. Novoselov, A. Geim, S. Morozov, D. Jiang, M. Katsnelson, I. Grigorieva, S. Dubonos, and A. Firsov, Nature **438**, 197 (2005).
- [30] Y. Zhang, Y. Tan, H. Stormer, and P. Kim, Nature **438**, 201 (2005).
- [31] K. Novoselov, E. McCann, S. Morozov, V. Fal'ko, M. Katsnelson, U. Zeitler, D. Jiang, F. Schedin, and A. Geim, Nature Physics **2**, 177 (2006).
- [32] E. McCann, Physical Review B **74**, 161403 (2006).
- [33] H. Min, B. Sahu, S. Banerjee, and A. MacDonald, Physical Review B **75**, 155115 (2007).
- [34] C. Lu, C. Chang, Y. Huang, R. Chen, and M. Lin, Physical Review B **73**, 144427 (2006).
- [35] M. Aoki and H. Amawashi, Solid State Communications **142**, 123 (2007).

- [36] P. Gava, M. Lazzeri, A. Saitta, and F. Mauri, *Physical Review B* **79**, 165431 (2009).
- [37] T. Ohta, A. Bostwick, T. Seyller, K. Horn, and E. Rotenberg, *Science* **313**, 951 (2006).
- [38] Z. Li, E. Henriksen, Z. Jiang, Z. Hao, M. Martin, P. Kim, H. Stormer, and D. Basov, *Physical Review Letters* **102**, 37403 (2009).
- [39] L. Zhang, Z. Li, D. Basov, M. Fogler, Z. Hao, and M. Martin, *Physical Review B* **78**, 235408 (2008).
- [40] A. Kuzmenko, E. van Heumen, D. van der Marel, P. Lerch, P. Blake, K. Novoselov, and A. Geim, *Physical Review B* **79**, 115441 (2009).
- [41] Y. Zhang, T. Tang, C. Girit, Z. Hao, M. Martin, A. Zettl, M. Crommie, Y. Shen, and F. Wang, *Nature* **459**, 820 (2009).
- [42] K. Mak, C. Lui, J. Shan, and T. Heinz, *Physical Review Letters* **102**, 256405 (2009).
- [43] E. Castro, K. Novoselov, S. Morozov, N. Peres, J. Dos Santos, J. Nilsson, F. Guinea, A. Geim, and A. Neto, *Physical Review Letters* **99**, 216802 (2007).
- [44] J. Oostinga, H. Heersche, X. Liu, A. Morpurgo, and L. Vandersypen, *Nature materials* **7**, 151 (2007).
- [45] F. Guinea, *Physics* **3**, 1 (2010).
- [46] R. Nandkishore and L. Levitov, *Physical Review Letters* **104**, 156803 (2010).

- [47] O. Vafek and K. Yang, *Physical Review B* **81**, 041401 (2010).
- [48] K. Sun, H. Yao, E. Fradkin, and S. Kivelson, *Physical Review Letters* **103**, 46811 (2009).
- [49] S. Latil and L. Henrard, *Physical Review Letters* **97**, 36803 (2006).
- [50] M. Koshino and E. McCann, *Physical Review B* **80**, 165409 (2009).
- [51] M. Koshino, *Physical Review B* **81**, 125304 (2010).
- [52] M. Dresselhaus and G. Dresselhaus, *Advances in Physics* **30**, 139 (1981).
- [53] P. Giannozzi, S. Baroni, N. Bonini, M. Calandra, R. Car, C. Cavazzoni, D. Ceresoli, G. Chiarotti, M. Cococcioni, I. Dabo, *et al.*, *Journal of Physics: Condensed Matter* **21**, 395502 (2009).
- [54] D. Vanderbilt, *Physical Review B* **41**, 7892 (1990).
- [55] T. Thonhauser, V. Cooper, S. Li, A. Puzder, P. Hyldgaard, and D. Langreth, *Physical Review B* **76**, 125112 (2007).
- [56] N. Marom, J. Bernstein, J. Garel, A. Tkatchenko, E. Joselevich, L. Kronik, and O. Hod, *Physical Review Letters* **105**, 46801 (2010).
- [57] S. Hikami, A. Larkin, and Y. Nagaosa, *Progress of Theoretical Physics* **63**, 707 (1980).
- [58] H. Suzuura and T. Ando, *Physical Review Letters* **89**, 266603 (2002).
- [59] A. Morpurgo and F. Guinea, *Physical Review Letters* **97**, 196804 (2006).

- [60] E. McCann, K. Kechedzhi, V. Falko, H. Suzuura, T. Ando, and B. Altshuler, *Physical Review Letters* **97**, 146805 (2006).
- [61] K. Kechedzhi, V. Falko, E. McCann, and B. Altshuler, *Physical Review Letters* **98**, 176806 (2007).
- [62] F. Tikhonenko, A. Kozikov, A. Savchenko, and R. Gorbachev, *Physical Review Letters* **103**, 226801 (2009).
- [63] E. McCann, *Physics* **2**, 98 (2009).
- [64] Y. Barlas, R. Côté, K. Nomura, and A. MacDonald, *Physical Review Letters* **101**, 97601 (2008).
- [65] Y. Zhao, P. Cadden-Zimansky, Z. Jiang, and P. Kim, *Physical Review Letters* **104**, 66801 (2010).
- [66] T. Giamarchi, *Quantum physics in one dimension*, Vol. 121 (Oxford University Press, USA, 2004).
- [67] R. Shankar, *Reviews of Modern Physics* **66**, 129 (1994).
- [68] W. Bao, L. Jing, Y. Lee, J. Velasco Jr, P. Kratz, D. Tran, B. Standley, M. Aykol, S. Cronin, D. Smirnov, *et al.*, Arxiv preprint arXiv:1103.6088 (2011).
- [69] Y. Lemonik, I. Aleiner, C. Toke, and V. Falko, *Physical Review B* **82**, 201408 (2010).
- [70] R. Bistritzer and A. MacDonald, *Proceedings of the National Academy of Sciences* **108**, 12233 (2011).

- [71] Y. Son, S. Choi, Y. Hong, S. Woo, and S. Jhi, Arxiv preprint arXiv:1012.0643 (2010).
- [72] M. Mucha-Kruczyński, I. Aleiner, and V. Falko, *Physical Review B* **84**, 041404 (2011).
- [73] K. Klitzing, G. Dorda, and M. Pepper, *Physical Review Letters* **45**, 494 (1980).
- [74] D. Thouless, M. Kohmoto, M. Nightingale, and M. Den Nijs, *Physical Review Letters* **49**, 405 (1982).
- [75] S. Raghu, X. Qi, C. Honerkamp, and S. Zhang, *Physical Review Letters* **100**, 156401 (2008).
- [76] J. Martin, B. Feldman, R. Weitz, M. Allen, and A. Yacoby, *Physical Review Letters* **105**, 256806 (2010).
- [77] F. Haldane, *Physical Review Letters* **61**, 2015 (1988).
- [78] N. Nagaosa, J. Sinova, S. Onoda, A. MacDonald, and N. Ong, *Reviews of Modern Physics* **82**, 1539 (2010).
- [79] C. Kane and E. Mele, *Physical Review Letters* **95**, 226801 (2005).
- [80] D. Xiao, W. Yao, and Q. Niu, *Physical Review Letters* **99**, 236809 (2007).
- [81] J. Li, I. Martin, M. Büttiker, and A. Morpurgo, *Nature Physics* **7**, 38 (2010).
- [82] H. Min, J. Hill, N. Sinitsyn, B. Sahu, L. Kleinman, and A. MacDonald, *Physical Review B* **74**, 165310 (2006).
- [83] C. Xu and J. Moore, *Physical Review B* **73**, 045322 (2006).

- [84] W. Norimatsu and M. Kusunoki, *Physical Review B* **81**, 161410 (2010).
- [85] M. Hasan and C. Kane, *Reviews of Modern Physics* **82**, 3045 (2010).
- [86] M. König, S. Wiedmann, C. Brüne, A. Roth, H. Buhmann, L. Molenkamp, X. Qi, and S. Zhang, *Science* **318**, 766 (2007).
- [87] I. Aleiner, D. Kharzeev, and A. Tsvelik, *Physical Review B* **76**, 195415 (2007).
- [88] S. Kim, K. Lee, and E. Tutuc, Arxiv preprint arXiv:1102.0265 (2011).
- [89] X. Qi and S. Zhang, *Physics Today* **63**, 33 (2010).
- [90] C. Kallin and B. Halperin, *Physical Review B* **30**, 5655 (1984).
- [91] I. Aleiner and L. Glazman, *Physical Review B* **52**, 11296 (1995).
- [92] H. Fertig, *Physical Review B* **40**, 1087 (1989).
- [93] K. Moon, H. Mori, K. Yang, S. Girvin, A. MacDonald, L. Zheng, D. Yoshioka, and S. Zhang, *Physical Review B* **51**, 5138 (1995).
- [94] T. Jungwirth and A. MacDonald, *Physical Review B* **63**, 035305 (2000).
- [95] K. Nomura and A. MacDonald, *Physical Review Letters* **96**, 256602 (2006).
- [96] J. Eisenstein and A. MacDonald, *Nature* **432**, 691 (2004).
- [97] D. Tilahun, B. Lee, E. Hankiewicz, and A. MacDonald, Arxiv preprint arXiv:1107.2969 (2011).
- [98] W. Bao, Z. Zhao, H. Zhang, G. Liu, P. Kratz, L. Jing, J. Velasco Jr, D. Smirnov, and C. Lau, *Physical Review Letters* **105**, 246601 (2010).

- [99] T. Taychatanapat, K. Watanabe, T. Taniguchi, and P. Jarillo-Herrero, Arxiv preprint arXiv:1104.0438 (to appear in Nature Physics) (2011).
- [100] L. Zhang, Y. Zhang, J. Camacho, M. Khodas, and I. Zaliznyak, Arxiv preprint arXiv:1103.6023 (2011).
- [101] A. Kumar, W. Escoffier, J. Poumirol, C. Faugeras, D. Arovas, M. Fogler, F. Guinea, S. Roche, M. Goiran, and B. Raquet, Arxiv preprint arXiv:1104.1020 (2011).
- [102] S. Jhang, M. Craciun, S. Schmidmeier, S. Tokumitsu, S. Russo, M. Yamamoto, Y. Skourski, J. Wosnitza, S. Tarucha, J. Eroms, *et al.*, Arxiv preprint arXiv:1106.4995 (2011).
- [103] C. Lui, Z. Li, K. Mak, E. Cappelluti, and T. Heinz, Arxiv preprint arXiv:1105.4658 (2011).
- [104] M. Koshino and E. McCann, Physical Review B **83**, 165443 (2011).
- [105] S. Yuan, R. Roldán, and M. Katsnelson, Arxiv preprint arXiv:1107.0057 (2011).
- [106] C. Töke and V. Falko, Physical Review B **83**, 115455 (2011).

Vita

Fan Zhang was born in Hubei, China on 8 December 1983, the son of Wen-liang Zhang and Zhong-mei Li. He received the Bachelor of Science degree in Physics from the University of Science and Technology of China in July 2006. In August 2006 he joined the Graduate School of the University of Texas at Austin to pursue a PhD in Physics.

Permanent Address: 2501 Lake Austin Blvd
Apt L103
Austin, TX 78703

This dissertation was typeset by the author.